Politecnico di Torino

The Exploration Company

POLITECNICO DI TORINO

Master Course in Aerospace Engineering
Academic Year 2023-2024

ADVANCED MODELING OF METALLIC ROCKET ENGINE NOZZLE EXTENSIONS AND THE PERFORMANCE IMPACT OF FILM COOLING

Supervisors:
Prof. Domenic D'Ambrosio
Prof. Roberto Marsilio

Company tutor:
Julian Matt

Candidate:
Marco Romano Delogu
294859

April 2024

Abstract

A great effort has been made by the European space industry to ensure an innovative and independent progress in space technology. In this context The Exploration Company, which supported the present work, is rapidly developing new technologies for future space transportation systems, including a new LOX/CH4 liquid rocket engine named Huracán that will equip their future space module and lunar lander Nyx Moon. This thesis focuses on the nozzle extension of the Huracán engine, which is a vital component for a rocket engine with in-space applications. Its purpose is to increase the velocity of the mass being ejected and hence the overall thrust produced by the engine. Although it is a thermally critical component, its design differs from that of the main combustion chamber due to the lower temperature of the expanding gases and the weight limitation that a large component such as the nozzle extension entails. In this work the flowfield behavior of the expanding gases in the nozzle extension has been investigated. An analytic model has been implemented on Python to provide useful data for the future design of the component. The model has been compared to numerical solutions obtained with Simcenter Star-ccm+ which include the most relevant phenomenon that characterize high temperature environments. Multiple cooling strategies have been investigated, with a focus on film cooling which is historically one of the most studied and used cooling technologies for this kind of application. Multiple combustion models and boundary conditions have been investigated to better understand how film cooling performs. Finally, the performance impact of film cooling has been evaluated in terms of Isp loss. The results of this thesis demonstrate that a rocket metallic nozzle extension can survive high temperature environments thanks to film cooling with a reduced Isp loss and provide useful data for the development of the nozzle extension and for future studies related to this component.

Contents

List of Figures

List of Tables

Acronyms

CEA	Chemical Equilibrium Application
CFD	Computational Fluid Dynamic
ESA	European Space Agency
FAC	Finite Area Combustor
FVM	Finite Volume Method
GCH4	Gaseous Methane
GCI	Grid Convergence Index
IAC	Infinite Area Combustor
LCH4	Liquid Methane
LNG	Liquefied Natural Gas
LOX	Liquid Oxygen
MCC	Main Combustion Chamber
NE	Nozzle Extension
NS	Navier Stokes
RANS	Reynolds Averaged Navier Stokes
S.I.	International measurement System
TIC	Truncated Ideal Contour
TOP	Thrust Optimized Parabolic (geometry)

Chapter 1

Introduction

This thesis was developed in collaboration with The Exploration Company in the context of the development of their engine named Huracán. In this chapter, the company vision and the historical context of the work are presented.

1.1 The Exploration Company

The Exploration Company is a spacecraft manufacturer startup founded in July 2021. A new reusable capsule named Nyx is under development. It is conceived as a cargo transport system to Earth and lunar orbit, but it is planned that in the future it could also transport astronauts. In one year of development the company has been able to design, manufacture and test its first iteration of their Huracán rocket engine that will equip the future lunar lander named Nyx Moon. The European Space Agency awarded The Exploration Company a contract on May 29, 2023, to carry out a research and development project for future European single-use and reusable spacecraft as part of ESA's Vision 2030+. In Series A, which was concluded in early 2023, the company raised 40 million euros for its Nyx capsule and in September 2023 announced an agreement with Axiom Space for the cargo resupply of their new space station. The first small-scale prototype, nicknamed Bikini, will be launched on the inaugural flight of Ariane 6 or on a PSLV Indian rocket providing useful data on ballistic reentry and TPS performance. Mission Possible is the second demonstrator, a recoverable reentry vehicle closer to the Nyx design that will be launched by a Falcon 9 in early 2025 and will feature the first cargo mission for the company with paying customers. The full scale Nyx capsule is planned to be launched in 2026 with Mission Odissey. The Nyx Moon project is expected to be ready for 2028 and will provide a Earth-Moon-Earth cargo transportation system as well as a Lunar Gateway resupply module. The future lunar lander will deliver cargo on the lunar surface as well as providing a lunar point to point cargo delivery system.

1.2 The Huracán engine

The cryogenic engine that will power the Nyx module and lunar lander is named Huracán. It is a bi propellant electric pump fed engine operating using liquid oxygen and bio-methane (LNG or LCH4) as propellants. It features an Inconel 718 3D-printed regeneratively cooled main combustion chamber (MCC) and injector head and it is designed to match high specific impulse and efficiency specifications. The engine is optimized for in-space vacuum operations and multiple re-lighting. The MCC is currently being developed and a prototype has been tested in Lampoldshausen in July 2023. Its nozzle extension (NE), which is the focus of this thesis, will be developed and manufactured in the next months. A short skirt version for passenger testing at sea level will be tested.

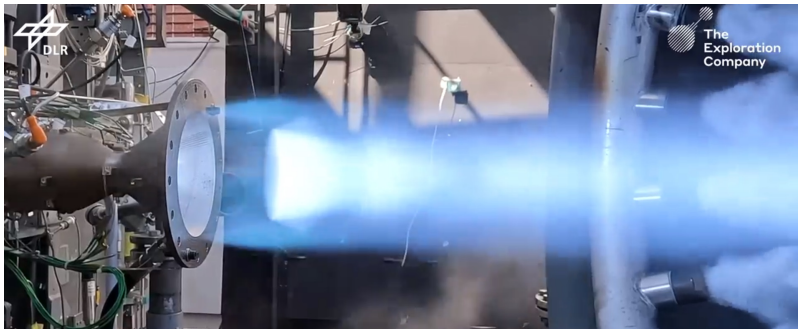

Figure 1.1: Huracán engine MCC test

1.3 Context

The development of liquid rocket engines is, historically, a hard task. It requires an in depth understanding of heat transfer, high temperature environments, fast moving gases and manufacturing techniques. Modern technologies and extensive studies helped gathering information on how rocket engines perform. Today, more and more private companies can afford the development of space related hardware, providing alternatives to national agencies services. In this context, additive manufacturing revolutionised the way rocket engine components are manufactured, from the combustion chamber to the injection head and feeding system components. Additive manufacturing reduces the time needed to adapt designed geometries to the limits of traditional manufacturing processes. This helps not only to reduce the time for design, but also lowers the overall manufacturing costs and speeds up the component development process. Thanks to 3D printing the main engine components can also be reduced and today an entire (small) main combustion chamber can be manufactured by additive manufacturing. The greatest limitation in additive manufacturing

is the dimension of the components that have to be built. Because of this, the Huracán engine NE can't be manufactured in a single piece together with the MCC.

1.4 Nozzle extension development

The combustion of the propellant in the MCC produces a gas with a high temperature and no material can sustain these, therefore, instead of trying to search a material that can withstand high temperatures, a material that can easily conduct heat is used. Rocket engine MCC are usually made with metallic alloys, usually steel or copper alloys (e.g. Inconel for nichel-chromium steel alloys or CuCrZr for copper alloys). To allow the metal to survive high temperatures, a cold liquid passed through the chamber walls and this technique is called regenerative cooling, allowing rocket engine to be built and used. When the gas expands through the convergent-divergent nozzle, it lowers its temperature and pressure, exchanging them with kinetic energy. Because of the third Newton's law, the gas ejected in a direction at high speed, provides a force in the opposite direction, called thrust. Multiple engines use regenerative cooling to refrigerate the entire engine and this is especially true for launchers engines that are limited in the expansion the can achieve. In fact, launchers must be able to provide thrust at different ambient conditions, including the sea level. At sea level, the ambient pressure is relatively high, around 101325 Pa and if the rocket nozzle expands the gas to pressures lower than the ambient pressure, it risks to encounter separation, which is the phenomenon that causes the detachment of the gas flow from the nozzle walls that can lead to the nozzle destruction. The condition in which the engine expands the gas more than outer pressure is called overexpansion (while the opposite, underexpansion). For launchers, the engine operates from the sea level conditions up to low pressure conditions in the high levels of the atmosphere. Therefore these engines light at sea level in slightly overexpanded conditions, they reach matched exit pressure conditions at altitude, and then continue in underexpansion until stage separation.

While overexpansion is dangerous for the structure of the nozzle, underexpansion means that the engine is not working in optimal conditions. Is underexpanded, part of the energy of the flow is not being converted in thrust and continues its expansion out of the nozzle. While this being a necessary compromise for launchers, it is not for rocket engines that have to operate in the near-vacuum environment of space, as the Huracán engine. For an engine designed to operate in space, there isn't an external ambient pressure that guides over/underexpansion, therefore these engines always operate in underexpanded conditions. This also means that the more the engine expands the gas, the more thrust is produced. However, increasing the expansion of the nozzle means increasing the dimensions of the engine, up to the point when the increase of mass exceeds the performance gained by generating more thrust. The expansion of the gas lower its temperature and pressure but a cooling technique

is still required. In the case of the Huracán engine, a metallic nozzle extension is investigated, using film cooling to lower wall temperatures within the acceptable range.

1.5 Purpose

The research about film cooling has been historically carried out experimentally, however in this work a simplified model for gaseous film cooling based on literature has been implemented and then compared with CFD results. The findings of the previous mentioned works have been compared to the outputs of this thesis. Its purpose is to use all the research findings on a real engine case, in order to provide vital information for the design of the component. The CFD computations have been carried out using Star-ccm+ while all other calculations have been performed on Python and MatLab.

Chapter 2

Theory background

This chapter summarises the theoretical background of an ideal rocket engine and of the CFD software used for the analysis, after describing the problem of the NE design and film cooling.

2.1 Nozzle extension

Since the gas in a space designed rocket engine is expanded more than a launcher engine, both the exit pressures and temperatures are lower. This means that the last part of the nozzle doesn't have to be refrigerated in the same way as the MCC. Therefore, the lower temperatures combined with the increase in dimensions for higher expansion ratios, lead to the fact that these engines do not feature a regenerative cooling system for the entirety of the engine. At this point, a separated nozzle extension becomes an feasible alternative. The main advantage of a NE without regenerative cooling is therefore the reduction of weight allowing to build a larger NE and improve the spacecraft performances. However, despite the temperatures being lower than the MCC, they are not low enough to simply manufacture and add a thin metallic layer as a NE. Depending on the case, a composite NE may be able to survive the hot gas high temperatures, however it brings other complications (mainly the composite-metallic interface with the MCC). For metallic NE multiple strategies can be used to lower the wall temperatures or increase the material survivability:

- Ablative cooling: consists in adding a layer of an ablative material on the wall surface that is consumed after every use, removing heat from the wall surface. This strategy is used when the engine doesn't have to be relighted multiple times or it has to fire for a limited amount of time, since the wall cannot survive without the ablative layer;
- Dump cooling: the coolant is poured through cooling channels inside the material and is then dumped overboard or injected into the nozzle and used as a film for the downstream;

- Radiative cooling: this is not properly a cooling technique since it is more a consequent effect of the nozzle walls becoming hotter. When a body heats up, it radiates part of that heat, technically cooling the wall;
- Film cooling: a small quantity of a cold fluid is injected from the injector plate (or close) on the MCC walls or at a specific location in the nozzle, to reduce wall temperatures by shifting the local mixture ratio or by creating a thin layer of colder gas.

Each of these strategies have their pros and cons. For a reusable engine, for example, ablative cooling is not suitable, while film cooling may significantly reduce the engine performances if a high coolant mass flow rate is required.

2.2 Film cooling

Injecting a small quantity on coolant near the wall to lower temperatures inevitably leads to a performance loss, due to the fact that part of the propellant is injected in a region where it can not react in the same conditions as the MCC, reducing thrust and specific impulse. However, it all depends on if or how the coolant is available and the engine mission. Multiple engines that flown in space missions implemented film cooling. On the Saturn V the F-1 engines injected the gas coming from the turbine exhaust of the gas-generator cycle into the NE walls via a tapered distribution manifold. Also the Saturn V J-2 upper stage engine used the turbine exhaust gas for the NE wall film cooling. Also the SSME, RD-180, Vinci and Vulcain 2 engines used some form of film cooling [22].

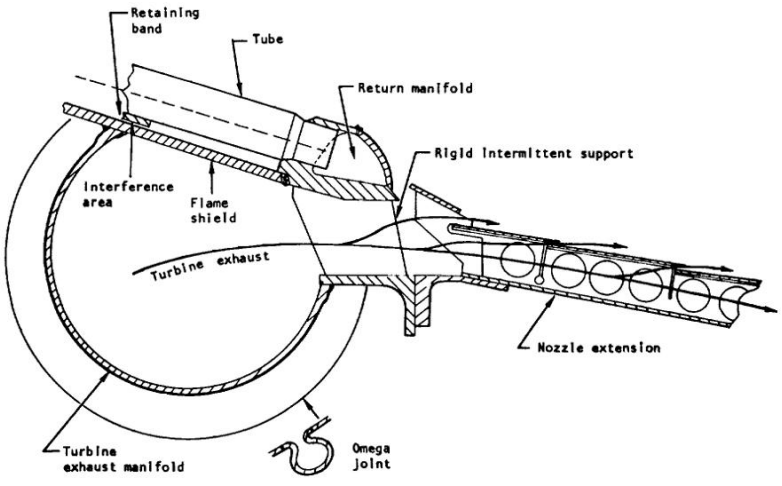

Figure 2.1: F-1 engine film cooling injection geometry [1]

Film cooling can be used for main combustion chambers if the regenerative system is not enough to lower wall temperatures or for specific parts of the nozzle, such as the throat or the NE. The coolant can also be both gaseous or liquid. When liquid, the cooling effect is increased since it requires a larger amount of heat to vaporize. Gaseous film cooling, however, is usually easier to get since most of the engine operate with gas cycles and are able to provide the necessary small amount of coolant from the cycle. Moreover, a gas can be injected supersonic, reducing the velocity ratio and the shear induced turbulence.

For the Huracán engine, the coolant is injected at the MCC-NE interface in the divergent part of the nozzle, where the flow is already supersonic. Despite liquid film cooling being a possibility, gaseous film cooling has been investigated in this thesis, since, as mentioned, it is usually easier to get a gaseous mass flow rate from the engine's cycle. The coolant is injected around the main flow with a supersonic injection. Supersonic film cooling has proven to be more effective in creating an uniform lower temperature gas layer close to the wall compared to subsonic film cooling. The gaseous coolant mass flow rate is therefore accelerated to supersonic speed before being injected into the main stream.

Supersonic mixing of two streams has been widely investigated, as well as the backward facing step interaction (for film cooling injection) with a compressible high speed flow. Peng and Jiang [21] investigate the influence of shock waves on supersonic film cooling, showing how an oblique shock wave can reduce the adiabatic wall cooling effectiveness and increase mixing. Takeshi K. et al. [18] also investigated the the film cooling-shock waves interactions concluding that the decreasing in film effectiveness is due to the decrease in local mach number and the increase in heat transfer coefficient. Juhany K. A. et al. [17] studies the effect of different coolant mach number and temperature determining their influence on film cooling effectiveness with an experimental campaign. Aupoix B. et al. [2] studies supersonic film cooling via an experimental setup, providing Schlieren visualizations of the flowfield structures. They showed the advantages of supersonic film cooling compared to subsonic film cooling and provided an experimental database for film cooling models validation. Song and Shen [28][29] studied the influence of both coolant feeding pressure and coolant channel lip thickness on the coolant flow, providing useful Schlieren visualizations as well.

2.3 Ideal rocket theory

In a rocket engine a convergent-divergent nozzle is used to accelerate a hot gas exchanging pressure and chemical energy for kinetic energy. When mass is accelerated or expelled in one direction from a system, a force (the thrust) is generated in the opposite direction and it is described by Newton's third law. A great acceleration of

a small amount of gas provides a small acceleration to the large mass of the vehicle the engine powers. To simplify the evaluation of rocket nozzle performances some assumptions are made, and the **ideal rocket** is defined[15]:

- the working fluid is a homogeneous gas, free of condensed species and obeys the perfect gas law;
- the chemical reaction is a constant pressure heating process;
- the expansion is steady, isentropic and one-dimensional.

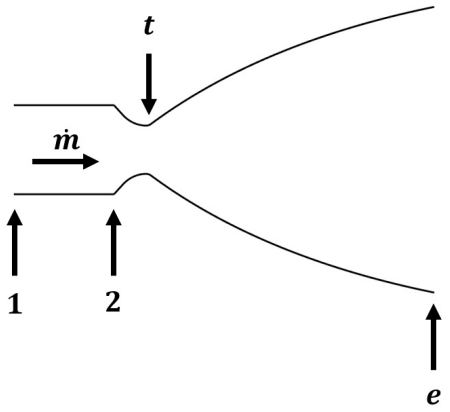

Figure 2.2: Nozzle scheme

The ideal rocket is therefore composed by a combustor and a convergent-divergent nozzle. Identifying with 1 and 2 respectively the inlet and the outlet of a combustor and with t and e the throat and exit section of the nozzle, from the energy equation:

$$\dot{Q} = \dot{m}(h_2^\circ - h_1^\circ) = \dot{m}c_p(T_2^\circ - T_1^\circ) \implies T_2^\circ = T_1^\circ + \frac{\dot{Q}}{\dot{m}c_p}$$

Where $\dot{Q}$ is the equivalent heating rate and $\dot{m}$ is the propellant mass flow rate. Assuming an adiabatic flow in the nozzle expansion, the conservation of total enthalpy is required and assuming that the velocity at the stage 2 is negligible:

$$h_2^\circ = h_e^\circ \implies \frac{u_e^2}{2} = h_2^\circ - h_e = c_p(T_2^\circ - T_e)$$

Since the expansion is isentropic:

$$u_e = \sqrt{2c_pT_2^\circ\left[1 - \left(\frac{p_e}{p_2^\circ}\right)^{\frac{\gamma-1}{\gamma}}\right]} = \sqrt{\frac{2\gamma\overline{R}}{(\gamma-1)\overline{M}}T_2^\circ\left[1 - \left(\frac{p_e}{p_2^\circ}\right)^{\frac{\gamma-1}{\gamma}}\right]}$$

Because of the conservation of total temperature and pressure in the nozzle expansion, the mass flow rate may be calculated using the throat area and stagnation properties:

$$\dot{m} = \frac{A_t p_2^\circ}{\sqrt{\frac{\overline{R}}{\overline{M}} T_2^\circ}} \sqrt{\gamma \left(\frac{2}{\gamma+1}\right)^{\frac{\gamma+1}{\gamma-1}}} = \frac{A_t p^\circ}{\sqrt{RT^\circ}} \sqrt{\gamma \left(\frac{2}{\gamma+1}\right)^{\frac{\gamma+1}{\gamma-1}}}$$

The thrust equation applied to a rocket engine is:

$$T = \dot{m} u_e + (p_e - p_a) A_e$$

Where p_a is the ambient pressure. Substituting the previous equations in the thrust equation and dividing for the throat area and total pressure, the thrust coefficient C_T is obtained:

$$C_T = \frac{T}{A_t p^\circ} = \sqrt{\frac{2\gamma^2}{\gamma-1} \left(\frac{2}{\gamma+1}\right)^{\frac{\gamma+1}{\gamma-1}} \left[1 - \left(\frac{p_e}{p^\circ}\right)^{\frac{\gamma-1}{\gamma}}\right]} + \left(\frac{p_e}{p^\circ} - \frac{p_a}{p^\circ}\right) \frac{A_e}{A_t}$$

Defining ε as the geometric expansion ratio:

$$\varepsilon = \frac{A_e}{A_t} = \frac{\sqrt{\gamma \left(\frac{2}{\gamma+1}\right)^{\frac{\gamma+1}{\gamma-1}}}}{\sqrt{\frac{2\gamma}{\gamma-1} \left(\frac{p_e}{p^\circ}\right)^{\frac{2}{\gamma}} \left[1 - \left(\frac{p_e}{p^\circ}\right)^{\frac{\gamma-1}{\gamma}}\right]}} \implies C_T = f(\gamma, \varepsilon, p_a)$$

It can be seen that C_T is a function of the geometry of the nozzle, the ambient pressure and the gas γ only. Figure 2.3 shows the relation between these parameters.

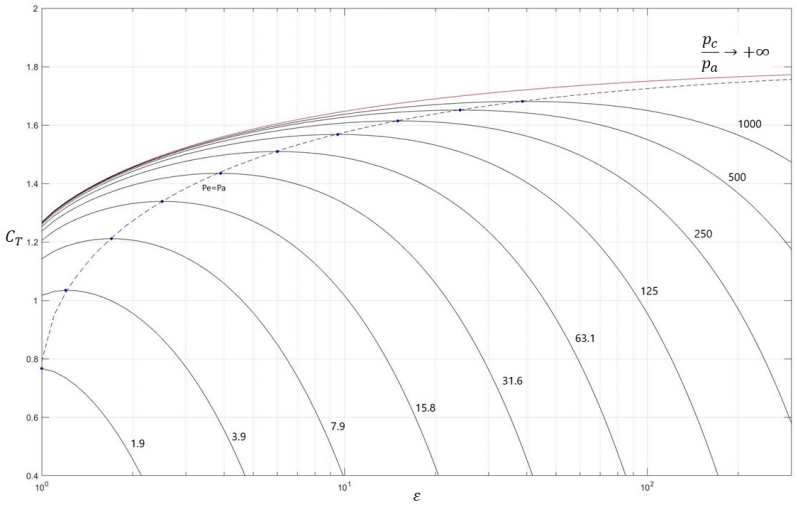

Figure 2.3: Thrust coefficient envelope

If the engine operates in atmosphere, increasing the geometric expansion ratio ε leads to flow separation when the exit pressure of the nozzle is lower than the atmospheric static pressure. Increasing ε always increases the engine thrust in vacuum conditions since the the nozzle is always underexpanded. Despite the monotonous trend of thrust, the advantage gained at high expansion ratio becomes less significant and the negative impact of mass increases due to the nozzle increased exit area, reducing the advantages of a higher thrust. The thrust coefficient puts a measure to how efficiently the gas energy is converted in kinetic energy during the expansion in the nozzle. To account for the combustion chamber performances too, another coefficient, the characteristic velocity, is defined:

$$c^* = \frac{p^\circ A_t}{\dot{m}} = \sqrt{\frac{\overline{R}T^\circ}{\overline{M}} \frac{1}{\gamma} \Big(\frac{\gamma+1}{2}\Big)^{\frac{\gamma+1}{\gamma-1}}}$$

Combining the previous equations the thrust can be rewritten as:

$$T = \dot{m} c^* C_T$$

Lastly, to put a measure to how much propellant is needed to produce a certain thrust for a certain period of time, the specific impulse is defined:

$$Isp = \frac{c^* C_T}{g} = \frac{u_{eq}}{g}$$

2.4 CFD theory

When it comes to fluids simulation, it is necessary to describe the equations governing their behaviour. A quick overview of the theoretical background of a CFD simulation is presented, focusing on the case of this thesis.

2.4.1 Equilibrium equations

The equilibrium (or conservation) equations describe the evolution of a fluid in time and space. These equations can be written from two points of view, generally referred to as the Eulerian and Lagrangian approaches. The Eulerian approach assumes a fixed control volume in space and time to determine the properties of the fluid flowing through it. The Lagrangian approach, on the other hand, assumes a fixed mass and follows its evolution as it moves through the fluid of which it is a part. The Eulerian approach is used to write the equilibrium equations in their integral form. Assumes a control volume V, delimited by a surface S as in figure2.4.
The first equation is the conservation of the mass and states that the temporal variation of the mass is equal to the flux of mass trough the surface of the control volume:

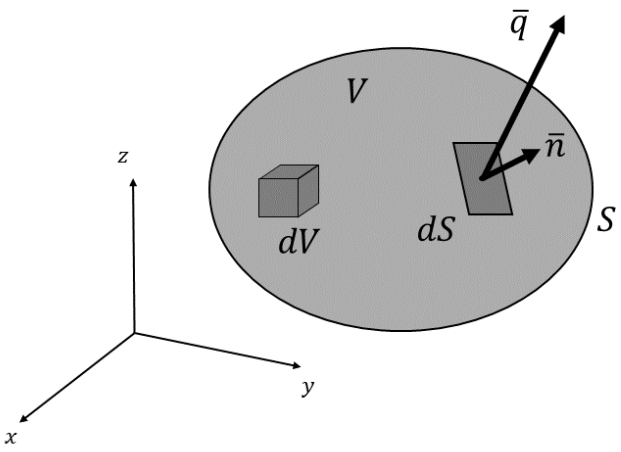

Figure 2.4: Control volume scheme

$$\frac{\partial}{\partial t}\int_V [\rho] dV = -\int_S [\rho \overline{q} \circ \overline{n}] dS \; [+source\; terms]$$

ρ is the fluid density (scalar), $\overline{q}$ is the velocity (vector) and $\overline{n}$ is the normal direction to the surface (vector). The symbol "$\circ$" indicates the scalar product. The minus sign indicates that when the mass leaves the control volume, mass is lost (the normal direction points out of the control volume). The mass is always globally conserved however in the case of a reacting flow the equation has to be solved for each species that can be created or destructed depending on the chemical reactions, with additional source terms in the equation.

The second equation is the momentum conservation equation. While the mass equation is scalar, the momentum equation is a vector as the velocity $\overline{q}$. The shape is equal to the mass equation, but the conservative variable in the momentum $\rho\overline{q}$:

$$\frac{\partial}{\partial t}\int_V [\rho \overline{q}] dV = -\int_S [\rho \overline{q}\overline{q} \circ \overline{n}] dS \; [+source\; terms]$$

Source terms for the momentum equation are usually divided in surface and volume sources:

$$\int_V [\rho \overline{f_c}] dV \qquad \int_S [\overline{\overline{\sigma}} \circ \overline{n}] dS$$

$\overline{f_c}$ are the volume forces per unit of mass (e.g. centrifugal, gravity) and they are vectors. $\overline{\overline{\sigma}}$ is a symmetric stress tensor that includes the pressure and viscous components (it's a 3X3 matrix). The momentum equation is therefore a vector equation.

The third and last equation is the energy conservation equation. The conservative variable is ρE, where E is the sum of internal (e) and kinetic energy ($q^2/2$):

$$E = e + \frac{q^2}{2}$$

The shape of the equation is the same as the other conservation, so the variation of the conservative variable integrated on the volume is equal to the flux of the conservative variable trough the control volume surface:

$$\frac{\partial}{\partial t}\int_V [\rho E]dV = -\int_S [\rho E \overline{q} \circ \overline{n}]dS \; [+source\,terms]$$

For the energy equation source terms consist in the exchange of work of surface and volume forces and eventual thermal heat flux trough the surface:

$$\dot{L_S} = \int_S [(\overline{\overline{\sigma}} \circ \overline{n}) \circ \overline{q}]dS \qquad \dot{L_V} = \int_V [\rho \overline{f_c} \circ \overline{q}]dV \qquad \dot{Q} = -\int_S [\overline{q}_\tau \circ \overline{n}]dS$$

The heat flux $\overline{q}_\tau$ is assumed to be positive when the heat leaves the system, therefore a minus sign is required. The equilibrium equations can be summarised as follows:

$$\frac{\partial}{\partial t}\int_V [U]dV = -\int_S [U(\overline{q} \circ \overline{n})]dS \; [+source\,terms] \qquad where \qquad U = \begin{cases} \rho \\ \rho\overline{q} \\ \rho E \end{cases}$$

$$\begin{cases} \frac{\partial}{\partial t}\int_V [\rho]dV = -\int_S [\rho \overline{q} \circ \overline{n}]dS \\ \frac{\partial}{\partial t}\int_V [\rho \overline{q}]dV = -\int_S [\rho \overline{q q} \circ \overline{n}]dS + \int_S [\overline{\overline{\sigma}} \circ \overline{n}]dS + \int_V [\rho \overline{f_c}]dV \\ \frac{\partial}{\partial t}\int_V [\rho E]dV = -\int_S [\rho E \overline{q} \circ \overline{n}]dS + \int_S [(\overline{\overline{\sigma}} \circ \overline{n}) \circ \overline{q}]dS + \int_V [\rho \overline{f_c} \circ \overline{q}]dS - \int_S [\overline{q}_\tau \circ \overline{n}]dS \end{cases}$$

The **Gauss theorem** states that if V is a subset of $\mathbb{R}^n$ (n=3 for a three dimensional space), it is compact, has a piecewise smooth boundary S and F is a continuously differentiable vector field defined on a neighborhood of V, then:

$$\int_S [\overline{F} \circ \overline{n}]dS = \int_V [\nabla \circ \overline{F}]dV$$

This theorem can be used to change all surface integrals to volume integrals and to rewrite the conservation equations in their differential formulation:

$$\begin{cases} \dfrac{\partial \rho}{\partial t} + \nabla \circ (\rho \overline{q}) = 0 \\ \dfrac{\partial (\rho \overline{q})}{\partial t} + \nabla \circ (\rho \overline{q} \overline{q}) = \nabla \circ \overline{\overline{\sigma}} + \rho \overline{f_c} \\ \dfrac{\partial (\rho E)}{\partial t} + \nabla \circ (\rho \overline{q} E) = \nabla \circ (\overline{\overline{\sigma}} \circ \overline{q}) + \rho \overline{f_c} \circ \overline{q} - \nabla \circ \overline{q}_\tau \end{cases}$$

In this formulation the problem is not closed. For a three dimensional case this system consists of 5 equation but the number of unknown variables is higher:

Variable	#unknowns
ρ	x1
$\overline{q}$	x3
$\overline{\overline{\sigma}}$	x6
e	x1
$\overline{q}_\tau$	x3
	14

Table 2.1: Equilibrium equations unknowns summary

To close the problem more equations are introduced. The stress tensor $\overline{\overline{\sigma}}$ can be divided for pressure (scalar field) and viscosity contributions:

$$\overline{\overline{\sigma}} = -p\overline{\overline{I}} + \overline{\overline{\tau}} \qquad where \qquad \overline{\overline{I}} = \begin{bmatrix} 1 & 0 & 0 \\ 0 & 1 & 0 \\ 0 & 0 & 1 \end{bmatrix}$$

For a Newtonian fluid, the viscous stress tensor can be written as the sum of an anisotropic and an isotropic term, for each tensor component, depending on the fluid dynamic viscosity μ:

$$\tau_{ij} = \mu\Big(\frac{\partial q_i}{\partial x_j} + \frac{\partial q_j}{\partial x_i}\Big) - \frac{2}{3}\mu(\nabla \circ \overline{q})\delta_{ij} \qquad where \qquad \delta_{ij} = \begin{cases} 1 & if \quad i = j \\ 0 & if \quad i \neq j \end{cases}$$

The heat exchange can be rewritten in terms of **Fourier's law**:

$$\overline{q}_\tau = -k \cdot \nabla T$$

With this approach the number of unknown variables has increased because of the addition of p and T (pressure and temperature) bringing the total number to 16. However it is possible to close the problem with the assumption of a perfect gas:

$$p = \rho RT \qquad e = c_v T \qquad c_v = \frac{R}{\gamma - 1} \qquad \gamma = \frac{c_p}{c_v}$$

Implementing these into the equilibrium equations the **Navier-Stokes** (NS) equations for **compressible flows** are obtained:

$$\begin{cases} \dfrac{\partial \rho}{\partial t} + \nabla \circ (\rho \overline{q}) = 0 \\ \dfrac{\partial (\rho \overline{q})}{\partial t} + \nabla \circ (\rho \overline{q} \overline{q}) = -\nabla p + \nabla \circ \overline{\overline{\tau}} + \rho \overline{f_c} \\ \dfrac{\partial (\rho E)}{\partial t} + \nabla \circ (\rho \overline{q} E) = -\nabla \circ (p \overline{q}) + \nabla \circ (\overline{\overline{\tau}} \circ \overline{q}) + \rho \overline{f_c} \circ \overline{q} - \nabla \circ (k \nabla T) \end{cases}$$

2.4.2 Navier Stokes (NS) equations for compressible, viscous and reacting flow

For a compressible, viscous and reacting flow (as the gas flow that is the focus of this thesis) the NS equations can be rewritten as follows:

$$\begin{cases} \dfrac{\partial \rho y_i}{\partial t} + \nabla \circ (\rho \overline{q} y_i) = -\nabla \circ \overline{J}_i + \dot{\omega}_i & 1 \leqslant i \leqslant N_S \\ \dfrac{\partial (\rho \overline{q})}{\partial t} + \nabla \circ (\rho \overline{q} \overline{q}) = -\nabla p + \nabla \circ \overline{\overline{\tau}} + \rho \overline{f_c} \\ \dfrac{\partial (\rho E)}{\partial t} + \nabla \circ (\rho \overline{q} E) = -\nabla \circ (p \overline{q}) + \nabla \circ (\overline{\overline{\tau}} \circ \overline{q}) + \rho \overline{f_c} \circ \overline{q} - \nabla \circ (k \nabla T) - \nabla \circ \overline{q}_m \end{cases}$$

The subscript i denotes the i-th chemical species, N_S is the number of chemical species and y_i is the corresponding species mass fraction. In the energy equation the sum of internal and kinetic energy depends on the mass fractions of the gas mixture:

$$E = \sum_{i=1}^{N_S} y_i e_i + \frac{1}{2} q^2$$

The internal energy is not a direct function of temperature anymore therefore its evaluation is more complicated than the perfect gas case:

$$\begin{cases} h_i = e_i + \frac{p}{\rho} \\ h_i = h_{f,i}^{\circ} + \int_{T_0}^{T} c_{p,i}(T) dT \end{cases} \implies e_i = h_i - \frac{p}{\rho} = \left(h_{f,i}^{\circ} + \int_{T_0}^{T} c_{p,i}(T) dT - \frac{p}{\rho} \right)$$

$\overline{q}_m$ in the energy equation is the energy flux transported by the diffusive mass flux:

$$\overline{q}_m = \sum_{i=1}^{N_S} \Big(h^{\circ}_{f,i} + \int_{T_0}^{T} c_{p,i}(T) dT \Big) \overline{J}_i$$

$-\nabla \circ \overline{J}_i$ is the mass diffusion term where $\overline{J}_i$ is expressed in terms of Fick's law:

$$\overline{J}_i = -\rho \alpha \nabla y_i = -\frac{\mu}{Sc} \nabla y_i$$

Fick's law describes the mass diffusivity which is the movement of mass from higher to lower concentrations. μ is the species viscosity, α is the mass diffusivity and Sc is the Schmidt number. The Schmidt number is a dimensionless number defined as the ratio of momentum diffusivity (kinematic viscosity) and mass diffusivity, used to characterize fluid flows with simultaneous momentum and mass diffusion processes:

$$Sc = \frac{\mu}{\rho \alpha}$$

The perfect gas law keep the same structure but the gas constant is adjusted:

$$p = \rho R T \qquad R = \sum_{i=1}^{N_S} y_i R_i \qquad R_i = \frac{\overline{R}}{M_i}$$

Where $\overline{R}$ is the perfect gas constant and M_i is the i-th species molecular mass. The $\dot{\omega}_i$ term in the mass equation is an source/destruction term. It contains all the contributions of each chemical reaction in which the i-th species is involved. If N_R is the number of chemical reactions and $1 \leqslant j \leqslant N_R$:

$$\sum_{i=1}^{N_S} \nu^R_{i,j} B_i \longleftrightarrow \sum_{i=1}^{N_S} \nu^P_{i,j} B_i$$

is the general chemical reaction equation. R and P stand for reactants and products, B_i are the chemical species and $\nu^{R,P}_{i,j}$ are the reaction stoichiometric coefficients. The $\dot{\omega}_i$ term is:

$$\dot{\omega}_i = M_i \sum_{j=1}^{N_R} (\nu^P_{i,j} - \nu^R_{i,j}) \Big[k_{f,j} \prod_{i=1}^{N_S} \Big(\frac{\rho_i}{M_i} \Big)^{\nu^R_{i,j}} - k_{b,j} \prod_{i=1}^{N_S} \Big(\frac{\rho_i}{M_i} \Big)^{\nu^P_{i,j}} \Big] \beta_j$$

β_j is a third body empiric correction coefficient and $k_{f/b,j}$ are the forward and backward equilibrium constant of each reaction. These constant are calculated by the **Arrhenius law**:

$$k_{f/b,j} = A T^{\beta} e^{-\frac{E_a}{RT}}$$

A is the pre-exponential factor, β is the temperature exponent and E_a is the reaction activation energy. The value of these parameters are given by combustion models for each reaction involved.

2.4.3 RANS equations

Most of the flows are not inviscid and laminar in real case applications. Therefore a strategy to model turbulence is needed. Turbulence is a chaotic, non stationary, multi-scale and three-dimensional phenomenon. Due to its multi-scale nature, it is not always possible to solve NS equations on cells that need to be as small as the turbulence dissipation phenomenon can be. The computational grid would necessitate to range from cells with a dimension comparable to the body dimension to cells orders of magnitude smaller. The RANS approach does not solve the NS on each scale but introduces an approximation that greatly decreases computational cost, since for most industrial application this is enough for a component design process. Assumes a generic time dependant variable $u(t)$. The Reynolds approach is based on a decomposition of the $u(t)$ variable. This can be written as the sum of an average value and a time dependant fluctuation:

$$u(t) = \widetilde{u}_i + u_i'(t)$$

$\widetilde{u}_i$ is the average value of $u(t)$ and $u_i'(t)$ is the time dependant fluctuation.

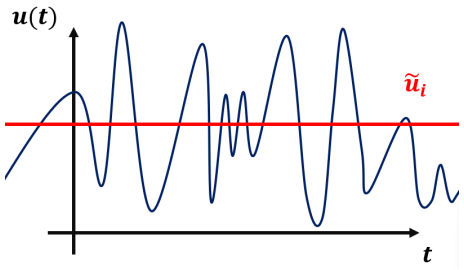

Figure 2.5: Reynolds decomposition

The average can be computed in different ways:

- Time average: for stationary problems the average field is not time dependant:

$$\widetilde{u}_i(\overline{x}) = \lim_{T\to\infty} \frac{1}{T} \int_t^{t+T} u_i(\overline{x}, t)dt$$

- Spatial average: for homogeneous in space problems:

$$\widetilde{u}_i(t) = \lim_{\Omega\to\infty} \frac{1}{\Omega} \int_\Omega u_i(\overline{x}, t)d\Omega$$

- Favre average: for compressible flows, density used as a weight:

$$\widetilde{u}_i(x) = \lim_{T\to\infty} \frac{1}{\overline{\rho}T} \int_t^{t+T} \rho u_i(x, t)dt$$

Regardless of the type, because of the averaging operator:

- The average of the average is equal to the average: $\widetilde{(\widetilde{u}_i)} = \widetilde{u}_i$;
- The average of the fluctuation is always equal to zero: $\widetilde{u}'_i = 0$;

Considering the mass and momentum equations of NS for an incompressible flow:

$$\begin{cases} \dfrac{\partial q_i}{\partial x_i} = 0 \\ \rho \dfrac{\partial q_i}{\partial t} + \rho q_j \dfrac{\partial q_i}{\partial x_j} = -\dfrac{\partial p}{\partial x_i} + \dfrac{\partial \tau_{ij}}{\partial x_j} \end{cases} \qquad \begin{cases} q_i = \widetilde{q}_i + q'_i \\ p = \widetilde{p} + p' \end{cases}$$

The Reynolds decomposition is applied to q and p and the formulation of the RANS equations is obtained:

$$\begin{cases} \dfrac{\partial \widetilde{q}_i}{\partial x_i} \\ \rho \dfrac{\partial \widetilde{q}_i}{\partial t} + \rho \widetilde{q}_j \dfrac{\partial \widetilde{q}_i}{\partial x_j} = -\dfrac{\partial \widetilde{p}}{\partial x_i} + \dfrac{\partial}{\partial x_j}(\widetilde{\tau_{ij}} + \tau^R_{ij}) \end{cases}$$

The term τ^R_{ij} is the Reynolds stress tensor:

$$\tau^R_{ij} = -\rho \widetilde{q'_i q'_j}$$

Because of this term, a turbulence model is required. One possible strategy is to describe the Reynolds tensor as a viscosity trough the Boussinesq linear eddy viscosity model:

$$\tau^R_{ij} = 2\mu_t \widetilde{S}_{ij} - \frac{2}{3}\mu_t \frac{\partial q_k}{\partial x_k}\delta_{ij} - \frac{2}{3}\rho K \delta_{ij}$$

This formulation divides the tensor in an isotropic and an anisotropic part. K is the turbulent kinetic energy:

$$K = \frac{1}{2}\widetilde{q'_i q'_i} = -\frac{1}{2\rho}\tau^R_{ii}$$

where τ^R_{ii} is the tensor trace, and $\widetilde{S}_{ij}$ is:

$$\widetilde{S}_{ij} = \frac{1}{2}\Big(\frac{\partial \widetilde{q}_i}{\partial x_j} + \frac{\partial \widetilde{q}_j}{\partial x_i}\Big)$$

The determination of the turbulent viscosity μ_t depends on the turbulence model.

2.4.4 SST (Menter) $K-\omega$ turbulence model

The SST (shear stress transport) $K-\omega$ turbulence model is a hybrid between the $K-\varepsilon$ and the standard $K-\omega$ models. The $K-\varepsilon$ model introduces two transport equations for K (turbulent kinetic energy) and ε (kinetic energy dissipation):

- $\dfrac{\partial(\rho K)}{\partial t}+\dfrac{\partial(\rho q_i K)}{\partial x_i}=\dfrac{\partial}{\partial x_i}\Big[\Big(\mu+\dfrac{\mu_t}{\sigma_K}\Big)\dfrac{\partial K}{\partial x_i}\Big]+\rho G_K-\rho\varepsilon+Y_M$
- $\dfrac{\partial(\rho\varepsilon)}{\partial t}+\dfrac{\partial(\rho q_i \varepsilon)}{\partial x_i}=\dfrac{\partial}{\partial x_i}\Big[\Big(\mu+\dfrac{\mu_t}{\sigma_\varepsilon}\Big)\dfrac{\partial \varepsilon}{\partial x_i}\Big]+C_{1\varepsilon}\dfrac{\varepsilon}{K}\rho G_K-C_{2\varepsilon}\dfrac{\rho\varepsilon^2}{K}$

The equations have the same shape as the equilibrium equations. The terms after the convective term are source/destruction terms of K and ε and Y_M takes into account the effect of compressibility. The turbulent viscosity is given by:

$$\mu_t=\rho C_\mu\frac{K^2}{\varepsilon}$$

The boundary conditions applied to turbulent kinetic energy and dissipation require $K=\varepsilon=0$ at the wall. Because of this, the $K-\varepsilon$ model does not describe well the behavior of the fluid near the wall if not enhanced wall function are implemented. The $K-\omega$ model solves this problem using the specific dissipation ω:

$$\omega\simeq\frac{\varepsilon}{K}$$

The additional transport equation are:

- $\dfrac{\partial(\rho K)}{\partial t}+\dfrac{\partial(\rho q_i K)}{\partial x_i}=\dfrac{\partial}{\partial x_i}\Big[\Big(\mu+\dfrac{\mu_t}{\sigma_K}\Big)\dfrac{\partial K}{\partial x_i}\Big]+\rho G_K-\rho\omega K\beta_*$
- $\dfrac{\partial(\rho\omega)}{\partial t}+\dfrac{\partial(\rho q_i \omega)}{\partial x_i}=\dfrac{\partial}{\partial x_i}\Big[\Big(\mu+\dfrac{\mu_t}{\sigma_\omega}\Big)\dfrac{\partial \omega}{\partial x_i}\Big]+\dfrac{\rho\alpha\omega}{K}G_K-\rho\omega^2\beta+\rho\dfrac{\sigma_1}{\omega}\Big(\dfrac{\partial K}{\partial x_i}\dfrac{\partial\omega}{\partial x_i}\Big)$

The $K-\omega$ describes very well the behaviour of the fluid near the wall but is heavily dependant on the initial value of ω. The SST (Menter) model uses the $K-\varepsilon$ model far from the wall and the $K-\omega$ model near the wall making a continuous blending between them.

2.4.5 Finite Volume Method

One of the techniques employed in computational fluid dynamics is the Finite Volume Method (FVM). This method involves the partitioning of the domain into a grid comprised of finite control volumes, and subsequently discretizing the governing differential equations to enable their application to the grid. The procedure of grid

generation for the computational domain includes geometry creation, followed by the meshing of the domain into the finite volume grid. By identifying commonalities in the three governing equations, a transport equation for a general property Φ can be developed as:

$$\frac{\partial(\rho\Phi)}{\partial t} + \frac{\partial}{\partial x_j}(\rho\Phi_i q_j) = \frac{\partial}{\partial x_j}\Big(\Gamma\frac{\partial\Phi_j}{\partial x_i}\Big)\ [+source\ terms]$$

This equation describes the change rate of property Φ within a fluid element plus the net rate of flow of Φ out of the fluid element, equal to the rate of increase of Φ due to sources. Γ is the diffusion coefficient. Upon integrating the equation across a three-dimensional control volume and employing Gauss's divergence theorem, the resulting equation is as follows:

$$\frac{\partial}{\partial t}\Big(\int_V[\rho\Phi]dV\Big) + \int_S[\overline{n}\circ(\rho\Phi\overline{q})]dS = \int_S\Big[\overline{n}\circ\Big(\Gamma\frac{\partial\Phi}{\partial x_j}\Big)\Big]dS + \int_V[S_\Phi]dV$$

$\overline{n}$ represents the surface normal vector to the area dS, and the product of n with a vector gives the component of that vector in the surface normal direction. Consequently, the second term on the left-hand side and the first term on the right-hand side represent the Φ flux through the surface, corresponding to convection and diffusion, respectively. By approximating each integral as the flux over the edges of a small control volume, this equation can be extended to a finite volume representation of a 3D geometry. The value of Φ is stored for the central node of each control volume (element) in the grid. The fluxes exchange between the control volumes take place at the faces. To approximate these fluxes at the faces, the center node values of the adjacent cells are employed. The set of rules governing how this approximation is executed are part of the discretization scheme. These fluxes are then utilized to calculate new values at the central nodes. The discretization scheme establishes a relationship between a new value of variable Φ at the central node of a control volume, the previous value at the same node, and the central node values from one or more adjacent control volumes. An example in a one dimensionale case with a centered scheme is presented.

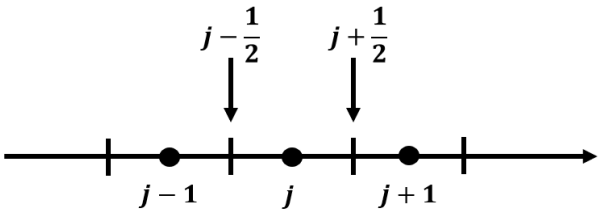

Figure 2.6: One dimensional finite volume discretization

Assumes a structured one dimensional grid. The center of the adjacent cells are $j-1$, j, $j+1$. The interfaces are $j-\frac{1}{2}$ and $j+\frac{1}{2}$. The simplified one dimensional equation to discretise is:

$$\frac{\partial}{\partial t}\int [u]dx = -(f^n_{j+1/2} - f^n_{j-1/2})$$

In this case n identifies the time step and f the interface flux. The average value of u on the cell is:

$$u_j = \frac{\int u dx}{\Delta x} \implies \Delta x \frac{\partial}{\partial t}(u_j) = -(f_{j+1/2} - f_{j-1/2})$$

As an example, a centered scheme is used:

$$\begin{cases} f_{j+1/2} = \frac{f_j + f_{j+1}}{2} \\ f_{j-1/2} = \frac{f_j + f_{j-1}}{2} \end{cases} \implies \Delta x = \frac{\partial u_j}{\partial t} = -\frac{f_{j+1} - f_{j-1}}{2}$$

$$\implies \Delta x \frac{\partial u_j}{\partial t} = \Delta x \frac{u^{n+1}_j - u^n_j}{2} + \frac{f_{j+1} - f_{j-1}}{2} = 0$$

At this point the discretization formulation for the update of the searched variable is obtained:

$$\frac{u^{n+1}_j - u^n_j}{\Delta t} + \frac{f_{j+1} - f_{j-1}}{2\Delta x} = 0$$

Chapter 3

Engine model

In order to provide a fast and reliable computation for the engine performances, Python has been used. The RocketCEA library has been implemented to obtain gas flow conditions to be used in the engine thermal model.

3.1 RocketCEA

The Chemical Equilibrium Application (CEA) is a chemical solver developed by NASA in the last 50 years. It contains a thermodynamic database with more than 1900 species both gaseous and condensed and represents still today a standard for the analysis of problems where combustion, rocketry, shocks and detonations are involved.

3.2 Routine input and chemical equilibrium

The CEA application obtains chemical equilibrium compositions for an assigned thermodynamic state [11][12]. Two thermodynamic state functions must be assigned:

Mode	Function
TP	Assigned temperature an pressure
HP	Assigned enthalpy and pressure
SP	Assigned entropy and pressure
TV	Assigned temperature and density
UV	Combustion at assigned density
SV	Assigned entropy and density
RKT	Rocket problem
SHOCK	Shock tube problem
DTN	Chapman-Jouguet Detonation

In the case of a **rocket problem** analysis, an HP thermodynamic state is assumed and specific rocket correlation are used to estimate the flow evolution. The procedure to determine the chemical equilibrium is based on the minimization of Gibbs free energy. A mixture of NS species is considered and the Gibbs energy per kilogram of mixture is:

$$g = \sum_{j=1}^{NS} \mu_j n_j \qquad\qquad \mu_j = \Big(\frac{\partial g}{\partial n_j}\Big)_{T,P,n_{i\neq j}}$$

μ_j is the chemical potential per kilogram-mole of the j species. The constraints for the minimization of free energy are:

$$\sum_{j=1}^{NS} a_{ij} n_j - b_i^\circ = 0 \qquad (i = 1, ..., l)$$

$$b_i - b_i^\circ = 0 \qquad (i = 1, ..., l)$$

$$b_i = \sum_{j=1}^{NS} a_{ij} n_j \qquad (i = 1, ..., l)$$

- a_{ij} are the number of kilogram-atoms of i element per kilogram-mole of species j;
- l is the number of chemical elements;
- b_i° is the assigned number of kilogram-atoms of element i per kilogram of total reactants;
- b_i is the number of kilogram-atoms of element i per kilogram of mixture.

The condition for equilibrium is:

$$\delta G = \sum_{j=1}^{NS} \Big(\mu_j + \sum_{i=1}^{l} \lambda_i a_{ij}\Big) \delta n_j + \sum_{i=1}^{l} (b_i - b_i^\circ) \delta \lambda_i = 0$$

where λ_i are Lagrangian multipliers and G is defined as:

$$G = g + \sum_{i=1}^{l} \lambda_i (b_i - b_i^\circ)$$

Considering δn_j and $\delta \lambda_j$ as independent:

$$\mu_j + \sum_{i=1}^{l} \lambda_i a_{ij} = 0 \qquad (j = 1, ..., NS)$$

The previous mentioned chemical potential can be written as:

$$\mu_j = \begin{cases} \mu_j^\circ + RT \ln \frac{n_j}{n} + RT \ln P & (j = 1, ..., NG) \\ \mu_j^\circ & (j = NG+1, ..., NS) \end{cases}$$

Where NG is the number of gaseous species and μ_j° is the chemical potential in the standard state. In the case of HP or rocket problems the thermodynamic state corresponding to a constant pressure combustion is specified by:

$$h = h_0$$

$$P = P_0$$

h is the specific enthalpy of the mixture and h_0 is a constant equal to the specific enthalpy of the reactants:

$$h = \sum_{j=1}^{NS} n_j H_j^\circ$$

H_j° is the standard-state molar enthalpy for species j at temperature T. The problem is not linear. A Newton-Raphson method is used to solve the iterative problem with corrections to the initial estimates of n_j, λ_j, n and T. The used correction variables are:

- $\Delta \ln n_j \qquad (j = 1, ..., NG)$;
- $\Delta n_j \qquad (j = NG+1, ..., NS)$;
- $\Delta \ln n$;
- $\pi_i = -\lambda_i / RT$;
- $\Delta \ln T$.

The obtained Newton-Rhapson equations are:

- $\Delta \ln n_j - \sum_{i=1}^{l} a_{ij} \pi_i - \Delta \ln n - \frac{H_j^\circ}{RT} \Delta \ln T = -\frac{\mu_j}{RT} \qquad (j = 1, ..., NG)$
- $-\sum_{i=1}^{l} a_{ij} \pi_i - \frac{H_j^\circ}{RT} \Delta \ln T = -\frac{\mu_j}{RT} \qquad (j = NG+1, ..., NS)$
- $\sum_{j=1}^{NG} a_{kj} n_j + \sum_{j=NG+1}^{NS} a_{kj} \Delta n_j = b_k^\circ - b_k \qquad (k = 1, ..., l)$
- $\sum_{j=1}^{NG} n_j \Delta \ln n_j - n \Delta \ln n = n - \sum_{j=1}^{NG} n_j$
- $\sum_{j=1}^{NG} \frac{n_j H_j^\circ}{RT} \Delta \ln n_j + \sum_{j=NG+1}^{NS} \frac{H_j^\circ}{RT} \Delta n_j + \left(\sum_{j=1}^{NS} \frac{n_j C_{p,j}^\circ}{R} \right) \Delta \ln T = \frac{h_0 - h}{RT}$

For TP, HP and SP problems combinations of the previous equations can be used to obtain corrections to estimates. For a large number of chemical species this results in a large number of equations. Obtaining the expression of $\Delta \ln n_j$ from the first equation it can be substituted to obtain reduced equation:

- $\sum_{i=1}^{l} \sum_{j=1}^{NG} a_{kj} a_{ij} n_j \pi_i + \sum_{j=NG+1}^{NS} a_{kj} \Delta n_j + \Big(\sum_{j=1}^{NG} a_{kj} n_j \Big) \Delta \ln n +$

$$+ \Big(\sum_{j=1}^{NG} \frac{a_{kj} n_j H_j^\circ}{RT} \Big) \Delta \ln T = b_k^\circ - b_k + \sum_{j=1}^{NG} \frac{a_{kj} n_j \mu_j}{RT} \qquad (k = 1, ..., l)$$

- $\sum_{i=1}^{l} a_{ij} \pi_i + \frac{H_j^\circ}{RT} \Delta \ln T = \frac{\mu_j}{RT} \qquad (j = NG+1, ..., NS)$

- $\sum_{i=1}^{l} \sum_{j=1}^{NG} a_{ij} n_j \pi_j + \Big(\sum_{j=1}^{NG} n_j - n \Big) \Delta \ln n +$

$$+ \Big(\sum_{j=1}^{NG} \frac{n_j H_j^\circ}{RT} \Big) \Delta \ln T = n - \sum_{j=1}^{NG} n_j + \sum_{j=1}^{NG} \frac{n_j \mu_j}{RT}$$

- $\sum_{i=1}^{l} \Big(\sum_{j+1}^{NG} \frac{a_{ij} n_j H_j^\circ}{RT} \Big) \pi_i + \sum_{j=NG+1}^{NS} \frac{H_j^\circ}{RT} \Delta n_j + \Big(\sum_{j=1}^{NG} \frac{n_j H_j^\circ}{RT} \Big) \Delta \ln n +$

$$+ \Big[\sum_{j=1}^{NG} \frac{n_j C_{p,j}^\circ}{R} + \sum_{j=1}^{NG} \frac{n_j (H_j^\circ)^2}{R^2 T^2} \Big] \Delta \ln T = \frac{h_0 - h}{RT} + \sum_{j=1}^{NG} \frac{n_j H_j^\circ \mu_j}{R^2 T^2}$$

After the calculation of the other correction variables, the corrections $\Delta \ln n_j$ are obtained from the original equation. The convergence tests for these equations are explained in a dedicated chapter on the guide [10].

3.3 CEA theoretical rocket performance

The CEA routine works as a chemical equilibrium application. To determine rocket engine performances a rocket model has to be defined [10].

3.3.1 IAC/FAC

In the CEA program combustion and throat parameters are calculated with two different approaches 3.1:

- IAC (infinite area combustor): only one combustor point is calculated, assumed with an infinite area;
- FAC (finite area combustor): three combustor points are calculated, one at an infinite area (to help iterative calculations) and the other two at the beginning and end of the combustor.

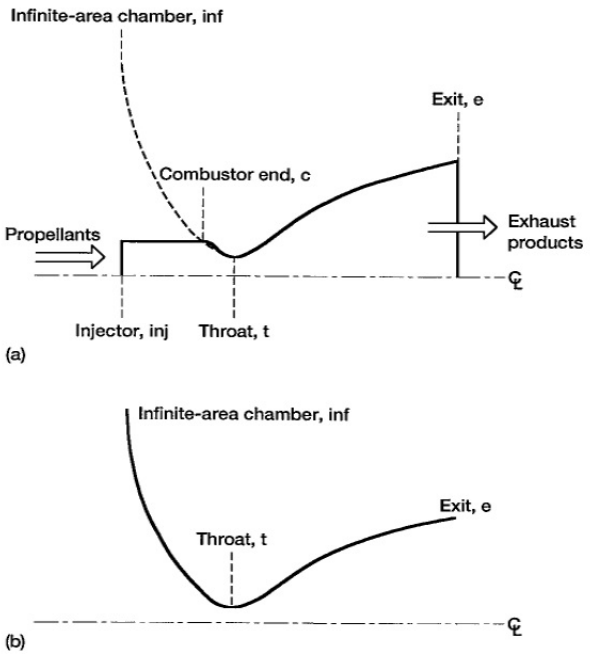

Figure 3.1: IAC/FAC approaches

3.3.2 Assumptions

Several assumption are made for both IAC and FAC model:

- 1D form of continuity, momentum and energy equations:

$$\rho_2 A_2 u_2 = \rho_1 A_1 u_1$$

$$P_2 + \rho_2 u_2^2 = P_1 + \rho_1 u_1^2$$

$$h_2 + \frac{u_2^2}{2} = h_1 + \frac{u_1^2}{2}$$

- Zero velocity at the combustion chamber inlet;
- Complete combustion;
- Adiabatic combustion;
- Isentropic expansion in the nozzle;
- Homogeneous mixing;
- Ideal-gas law;
- Zero velocity lags and zero temperature lags between condensed and gaseous species

For the **FAC** model a constant area combustor is assumed, the combustion is a non isentropic, irreversible process. During the burning process part of the energy released is used to raise the entropy, and the pressure drops.

Chemical equilibrium of the combustion products are assumed to obtain combustion conditions:

- IAC model: it is possible to calculate performances assuming either chemical equilibrium (instantaneous chemical equilibrium during expansion) or frozen equilibrium (frozen composition at the combustion composition during expansion);
- FAC model: only chemical equilibrium computations are possible.

Combustion inlet conditions are obtained assuming the same velocity (or zero velocity) at the combustion chamber inlet for both IAC and FAC models. Assuming the velocity at the combustion chamber inlet to be negligible, the exit velocity is:

$$u_e = \begin{cases} \sqrt{2(h_\infty - h_e)} & IAC\ \ model \\ \sqrt{2(h_{inj} - h_e)} & FAC\ \ model \end{cases}$$

From the momentum equation:

$$F = \frac{\dot{m} u_e}{g_c} + (P_e - P_a) A_e$$

Where $g_c = 1$ for S.I. units. Specific impulse is computed in the form of a velocity [m/s]. In this case when the ambient pressure is equal to the exit pressure, the specific impulse is equal to the exit gas velocity:

$$I = \frac{F}{\dot{m}} = \frac{u_e}{g_c} + \frac{(P_e - P_a) A_e}{\dot{m}} \implies I_{sp} = \frac{u_e}{g_c}$$

When the ambient is assumed as vacuum, the specific impulse is:

$$I_{vac} = I_{sp} + \frac{P_e A_e}{\dot{m}}$$

The remaining rocket parameters are computed as follows:

$$M = \frac{u}{a} \qquad c* = \frac{P_\infty A_t g_c}{\dot{m}} \qquad \frac{A}{\dot{m}} = \frac{1}{\rho u_e}$$

$$C_F = \frac{u}{c*} \qquad \frac{A_e}{A_t} = \frac{(A/\dot{m})_e}{(A/\dot{m})_t}$$

3.3.3 Rocket performances with IAC

For the IAC model the rocket performances determination procedure begins with the determination of the combustion properties and then the throat exhaust properties are calculated. If assigned, it calculates exhaust properties for other stations (as area ratios or pressure ratios). Combustion temperature and equilibrium compositions are obtained for an assigned chamber pressure and reactant enthalpy at the inf station and the entropy is then calculated. This entropy is assumed as constant during the expansion in the nozzle.

Throat conditions

Throat conditions are determined locating the area ratio where the velocity of the gas is equal to the sound speed. The process is iterative because the adiabatic expansion coefficient is unknown:

$$\frac{P_\infty}{P_t} = \left(\frac{\gamma_s + 1}{2}\right)^{\frac{\gamma_s}{\gamma_s - 1}}$$

This equation is exact only when γ_s is constant. From s_∞ and P_t it is possible to calculate u_e^2 and a_e^2 and the following convergence test is made:

$$\left|\frac{u_e^2 - a_e^2}{u_e^2}\right| \leqslant 0.4 \cdot 10^{-4}$$

This test ensures that the Mach number is within $1 \pm 0.2 \cdot 10^{-4}$. If the convergence requirement is not met, an improved estimation is made:

$$P_{t,k+1} = \left(P\frac{1 + \gamma_s M^2}{1 + \gamma_s}\right)_{t,k}$$

where k is the k-th iteration (maximum of 4 iterations). In case of a discontinuity of the velocity of sound at the throat (due to any transition point, such as a melting point) the solution requires the following equation that estimates the throat pressure at the melting point:

$$\ln(P_t) = \ln P + \left(\frac{\partial \ln P}{\partial \ln T}\right)_S (\ln T_m - \ln T)$$

$\mathbf{P_\infty/P_e}$ estimation

An iterative process is used to obtain pressure ratios for each assigned area ratio. The first estimation of the pressure ratios used an empirical correlation, however if the supersonic are ratios are greater than 2, the first estimation is made through an analytic expression. For subsonic area ratios:

$$\ln \frac{P_\infty}{P_e} = \frac{\ln \frac{P_\infty}{P_t}}{\frac{A_e}{A_t} + 10.587\left(\ln \frac{A_e}{A_t}\right)^3 + 9.454 \ln \frac{A_e}{A_t}} \qquad \left(\frac{A_e}{A_t} \geqslant 1.09\right)$$

$$\ln\frac{P_\infty}{P_e}=\frac{0.9\ln\frac{P_\infty}{P_t}}{\frac{A_e}{A_t}+10.587\Big(\ln\frac{A_e}{A_t}\Big)^3+9.454\ln\frac{A_e}{A_t}}\qquad\Big(1.0001<\frac{A_e}{A_t}<1.09\Big)$$

For supersonic area ratios:

$$\ln\frac{P_\infty}{P_e}=\ln\frac{P_\infty}{P_t}+\sqrt{3.294\Big(\ln\frac{A_e}{A_t}\Big)^2+1.535\ln\frac{A_e}{A_t}}\qquad\Big(1.0001<\frac{A_e}{A_t}<2\Big)$$

$$\ln\frac{P_\infty}{P_e}=\gamma_s+1.4\ln\frac{A_e}{A_t}\qquad\Big(\frac{A_e}{A_t}\geqslant 2\Big)$$

The first estimations of P_∞/P_e are improved with the following iterative process:

$$\Big(\ln\frac{P_\infty}{P_e}\Big)_{k+1}=\Big(\ln\frac{P_\infty}{P_e}\Big)_k+\Big[\Big(\frac{\partial\ln\frac{P_\infty}{P_e}}{\partial\ln\frac{A_e}{A_t}}\Big)_s\Big]_k\cdot\Big[\ln\frac{A_e}{A_t}-\Big(\ln\frac{A_e}{A_t}\Big)_k\Big]$$

Where the derivative is:

$$\Big(\frac{\partial\ln\frac{P_\infty}{P_e}}{\partial\ln\frac{A_e}{A_t}}\Big)_s=\frac{1}{\Big(\frac{1}{\gamma_s}-\frac{nRT}{u^2}\Big)_e}=\Big(\frac{\gamma_s u^2}{u^2-a^2}\Big)_e$$

k is the kth estimate. The procedure is continued until the following condition is met, with a maximum of 10 iterations:

$$\Big|\Big(\ln\frac{P_\infty}{P_e}\Big)-\Big(\ln\frac{P_\infty}{P_e}\Big)_k\Big|\leqslant 0.00004$$

3.3.4 Rocket performances with FAC

For the FAC model the combustion properties at the combustor inlet are first determined (inj station). At iterative loop that involves the inf conditions is used to determine the combustor end properties (subscript c) and the throat exhaust properties. As in the IAC model, other nozzle points properties are determined if specified. Combustion temperature and equilibrium compositions are obtained for an assigned chamber pressure and reactant enthalpy but in the FAC model the combustion is a nonisentropic process. The entropy increases from s_{inj} to s_c and the pressure drops from P_{inj} to P_c. The entropy at the end of the combustor s_c is assumed constant for the isentropic expansion in the nozzle. The finite area combustor is assumed to have a constant cross section. The momentum equation is:

$$(P+\rho u^2)_{inj}=(P+\rho u^2)_c$$

Using the continuity equation:

$$\left(P + \frac{\dot{m}u}{A}\right)_{inj} = \left(P + \frac{\dot{m}u}{A}\right)_c$$

The injection velocity is negligible, therefore:

$$P_{inj} = (P + \rho u^2)_c = \left(P + \frac{\dot{m}u}{A}\right)_c$$

An iterative procedure is required to solve this equation. The procedure depends on the input data of the FAC model. If the contraction ratio A_c/A_t is assigned P_∞ is estimated by:

$$P_\infty = P_{inj}\left(\frac{1.0257 - 1.2318\frac{A_c}{A_t}}{1 - 1.26505\frac{A_c}{A_t}}\right)$$

However, if the mass flow rate per unit combustor area $\dot{m}/A_c$ is assigned, a first estimation of A_c/A_t is required:

$$\frac{A_c}{A_t} = \frac{P_\infty}{2350\frac{\dot{m}}{A_c}}$$

This equation comes from the definition of characteristic velocity. After the computation of P_∞, the iterative process continues until:

$$\frac{|P_{inj} - (P + \rho u^2)_c|}{P_{inj}} \leqslant 2 \cdot 10^{-5}$$

The improved estimate for P_∞ is obtained by assuming that the ratio of this desired $P_{inf,new}$ value to the current value of P_{inj} is equal to the ratio of the assigned value of P_{inj} ($P_{inj,a}$) to the current value of P_{inj}:

$$P_{inf,new} = P_\infty \frac{P_{inj,a}}{P_{inj}}$$

In the case where the contraction ratio is not assigned:

$$\frac{A_c}{A_t} = \frac{\frac{\dot{m}}{A_t}}{\frac{\dot{m}}{A_c}}$$

3.4 Frozen rocket performances

The frozen composition model assumes infinitely slow reaction rates. After obtaining combustion conditions in the same way as before, the exit conditions are computed as follows. An improved estimation of the exit temperature are obtained:

$$(\ln T_e)_{k+1} = (\ln T_e)_k + (\Delta \ln T_e)_k$$

Where:

$$(\Delta \ln T_e)_k = \frac{s_\infty - s_{e,k}}{c_{p,e,k}}$$

The iterative procedure continues until:

$$|\Delta \ln T_e| < 0.5 \cdot 10^{-4}$$

The derivatives based on frozen composition are as follows:

$$\left(\frac{\partial \ln V}{\partial \ln T}\right)_P = 1 \qquad \left(\frac{\partial \ln V}{\partial \ln P}\right)_T = -1$$
$$c_v = c_{p,f} - nR \qquad \gamma_s = \gamma$$

3.5 Nozzle extension model

The CEA routine provides the hot gas properties for each specified expansion ratio ε for both equilibrium and frozen computations. These properties include:

- Gas state properties: static pressure, static temperature and density, mach number;
- Thermodynamic properties: specific heat, adiabatic expansion coefficient, sonic velocity;
- Transport properties: viscosity, conductivity, Prandtl number;
- Rocket performance parameters: characteristic velocity, specific impulse, thrust coefficient;
- Hot gas composition in terms of species mass fraction above an arbitrarily chosen threshold.

The averaged molecular mass M_g of the gas is computed from the species mass fractions and their own molecular mass as follows:

$$M_g = \sum_i y_i M_i \quad [kg/kmol]$$

Static gas temperature is corrected assuming a target combustion efficiency η_{ef}:

$$T_g = T_{g,ideal} \cdot \eta_{ef}^2$$

Total temperature and pressure are calculated knowing the gas mach number M and adiabatic expansion coefficient γ:

$$T_g^\circ = T_g\left(1 + \frac{\gamma - 1}{2}M^2\right) \qquad p_g^\circ = p_g\left(1 + \frac{\gamma - 1}{2}M^2\right)^{\frac{\gamma}{\gamma-1}}$$

A simple Prandtl based approach to estimate the recovery factor in a compressible turbulent boundary layer is used[19]:

$$r = \frac{T_{aw} - T_g}{T_g^\circ - T_g} = Pr^{\frac{1}{3}}$$

T_{aw} is the adiabatic wall temperature (or recovery temperature) and it can be calculated using the recovery factor:

$$T_{aw} = T_g + r\frac{u_g^2}{2c_p} = T_g\left(1 + r\frac{\gamma - 1}{2}M^2\right)$$

To solve the interface temperature problem and obtain the maximum wall temperature, a simple heat transfer model is implemented. Through forced convection, the wall is heated by the hot gas stream. The metallic wall conducts the heat to the external surface where it radiates the heat towards ambient vacuum or nearby bodies as shown in Figure 3.2:

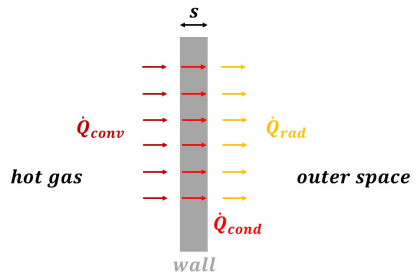

Figure 3.2: Heat transfer model

3.5.1 Hot gas heat transfer

When a hot gas flows over a non adiabatic wall it exchanges heat with it through convection. The generic convective heat transfer equation is:

$$\dot{Q}_{conv} = h_{conv}(T_{aw} - T_{wall,in}) \qquad \left[\frac{W}{m^2}\right]$$

The convective heat transfer coefficient has to be evaluated. Multiple heat transfer coefficient correlations have been proposed. Bartz, modified Bartz and Pavli heat transfer coefficient estimations are widely used in rocket applications. When it comes to predict MCC heat fluxes, all the models are able to replicate the experimental trend, but Bartz and Pavli tend to underestimate heat flux while modified Bartz

usually overestimates it. Despite the fact that these are their typical behaviour, they are not always true when compared with experimental data, therefore in some cases they over or under predict the heat flux depending on the case. However for compressible supersonic flows (as in the NE), Pavli's heat transfer coefficient estimation proved to better estimate experimental data [6]. For this reason, in this case Pavli's heat transfer estimation is used. This correlation is given in terms of the Stanton number [6]:

$$St = \frac{h_{conv}}{\rho u c_p} = \frac{Nu}{PrRe}$$

The Stanton number measures the ratio of heat transferred into a fluid to the thermal capacity of the fluid. It can be expressed as a combination of Nusselt, Reynolds and Prandtl numbers. The Pavli equation [7] is:

$$St_{Pavli} = 0.023 Re^{-0.2} Pr^{-0.6} \left(\frac{T_{aw}}{T_{ref}}\right)^{0.6} \left(\frac{x}{x_{throat}}\right)^{-0.2}$$

The convective heat transfer coefficient is, therefore:

$$h_{conv} = St_{Pavli} \cdot \rho_g \cdot u_g \cdot c_p$$

3.5.2 Wall heat transfer

The model solves a one-dimensional thermal problem for each expansion ratio ε. Inside the solid wall, simple conduction heat transfer is considered. From the one-dimensional Fourier's law:

$$q_\tau = -k\nabla T \implies q_\tau = -k\frac{\partial T}{\partial x}$$

Assuming a one-dimensional and homogeneous material the integrated equation gives:

$$\frac{Q}{A} = -k\frac{\Delta T}{s} \quad \left[\frac{W}{m^2}\right]$$

Q is the local surface heat flux and s is the wall thickness. In this case the temperature delta is the difference between the inner and outer wall temperatures:

$$\dot{Q}_{cond} = -k\frac{T_{wall,in} - T_{wall,out}}{s}$$

The wall conductivity k is assumed as constant for each material. In a real case the thermal conductivity greatly changes with temperature, therefore the value for expected high temperatures is used.

3.5.3 External radiation model

A simple grey body emissivity model is used:

$$\dot{Q}_{rad} = \varepsilon \sigma T_{wall,out}^4 \quad \left[\frac{W}{m^2}\right]$$

The emissivity ε is a free parameter depending on the considered material. σ is the Stefan-Boltzmann constant ($5,67037 \cdot 10^{-8}$ $[W/m^2K^4]$) and $T_{wall,out}$ is the external wall temperature. An outer temperature equal to zero is considered. Assuming outer temperature equal to 0 K is a big approximation. The outer temperature around earth averages around 283.32 K [20] reducing the heat that the nozzle can radiate. Moreover, multiple engine coupling effect has to be evaluated. In these cases, the equation becomes:

$$\dot{Q}_{rad} = \varepsilon \sigma (T_{wall,out}^4 - T_{ext}^4)$$

3.6 Film cooling model

When it comes to describe the interaction between moving fluids, creating an analytical model becomes a hard task. In the case of film cooling a coolant flow is injected parallel to the wall of a combustion chamber where a hot gas flow is present. A differential 1D model able to estimate wall temperature when film cooling is present could help and improve the design phase of a film cooled rocket nozzle. Unfortunately such a comprehensive model does not exist. Today, with the help of CFD, film cooling performance can be studies with more precision. However, film cooling has been used multiple times even when CFD was not a practical tool. Therefore, film cooling studies were carried out with experimental test campaigns. While experimental tests are way more instructive than computations, an estimation on how film cooling performs made with a 1D model is needed. A limited number of models for both liquid and gaseous film cooling have been developed. Grisson [14] model for liquid film cooling is a 1D differential model for liquid film cooling in combustion chambers. The model includes the estimation of the film cooling length (i.e. the length of the liquid phase-film cooled region) from the calculation of the coolant evaporation rate due to heating. Radiative and convective heating of the film are considered. The model neglects liquid droplets entrainment into the hot gas stream, therefore it can be applied to reduced coolant mass flow rate test cases. The model states that even after that the cooling stream completely evaporates, the coolant keeps flowing in proximity of the walls, providing an additional downstream vapor phase protection. Shine et al. [26] developed a 0D analytical model for liquid film cooled combustion chambers, including hot-gas radiation and liquid coolant droplets entrainment into the hot gas flow. The correlation by Sawant et al. [25] to compute mass transfer via entrainment is used. Liquid stream - hot gas convection and radiation are computed

assuming an instantaneous heating of the liquid to its saturation temperature. The evaporation process is calculated similarly to Grisson's model, by calculating a dry wall heat transfer coefficient and than correcting it for transpiration. Di Matteo et al. [8] developed a gaseous film cooling model. It is a quasi-2D differential-algebraic formulation to study the shear mixing that originates from a gaseous wall film jet. The mixing geometry is based on Simon [27]. The film cooling heat model adopted in this thesis is based on Di Matteo et al. [8] gaseous film cooling model since is the only one that tries to model a gas-gas interaction. Experimental evidences and previous works showed a linear growth rate in the mixing region after the coolant injection, therefore three zones are identified as in Figure 3.3 and the quantities exchanged between them are calculated trough geometrical relations. The three zones (core, mixing and coolant) are assumed to be at the same pressure for any given cross section of the combustion chamber, determined without film cooling.

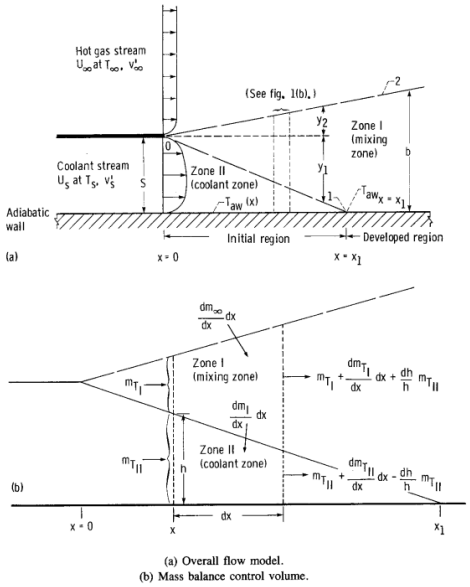

Figure 3.3: Flowfield geomerty by Simon's model[27]

The thermal behavior of the model is described in subsection 3.6.1. The most relevant parameters to obtain are the film cooling effectiveness η, the blowing ratio B and the velocity ratio R:

$$\eta = \frac{T_{aw} - T_g}{T_c - T_g} \qquad B = \frac{(\rho u)_g}{(\rho u)_c} \qquad R = \frac{u_g}{u_c}$$

Film cooling effectiveness is the ratio of the difference between the adiabatic wall temperature with film cooling and the gas temperature over the difference between the coolant temperature and the gas temperature. It determines how well and how long on the wall the injected mass flow film cools effectively. The blowing ratio,

together with the velocity ratio, determine the momentum ratio between the hot gas and the coolant which influences how the primary and secondary flows interact and mix.

3.6.1 Film cooling thermal model

The film region length x_1 is first calculated. This length is also called potential core length and represents the region where the gas properties are considered to be equal to the coolant properties. The convective heat flux is therefore computed by the film conditions, whilst the convective heat flux in the developed region is computed by the mixing conditions. An iterative procedure to compute x_1 is proposed in the original model [8]:

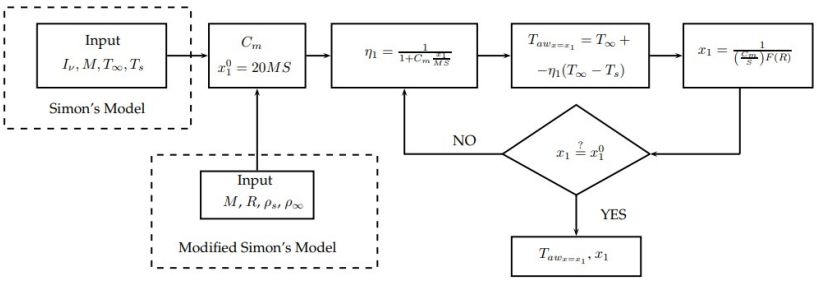

Figure 3.4: Iterative procedure for the potential core length estimation [8]

Where B is the blowing ratio $(\rho u)_g/(\rho u)_{film}$, h_{slot} is the slot height of the film injection, C_m is the mixing coefficient and it is equivalent to the mixing zone growth rate. T_{aw} is the adiabatic wall temperature and F(R) is:

$$F(R) = \frac{y_1}{y_2} = \frac{1}{\frac{\rho_{film}}{\overline{\rho}_{mix}(0.416+0.134R)} - 1}$$

$\overline{\rho}_{mix}$ is the average density of the mixing zone, calculated using the perfect gas equation of state at the temperature $T_{aw_{x=x_1}}$. R (velocity ratio) is defined as:

$$R = k_R \frac{u_g}{u_{film}}$$

where $k_R = Nb/2\pi R_c$ is a correction parameter to take into account a discrete number of injection slots (N is the number of slots), b is the slot width and r_c is the combustion chamber radius. The mixing zone growth rate is:

$$\frac{db}{dx} = C_m = \pm c \frac{R-1}{R+1}$$

c is a function of the density ratio ρ_g/ρ_{film}:

$$c = \frac{0.27}{2} \frac{\left[1 + \left(\frac{\rho_g}{\rho_{film}}\right)^{0.5}\right]}{\left(\frac{\rho_g}{\rho_{film}}\right)^{0.5}}$$

Knowing the potental core length x_1 the flowfield geometry can be calculated as in Figure 3.3:

$$y_{1,i} = \frac{h_{slot}}{x_1} x_i \qquad y_{2,i} = \frac{db}{dx} x_i$$

$$A_{g,i} = \pi(r_{c0} - y_{2,i})^2 \qquad A_{film,i} = \pi[r_c^2 - (r_{c0} + y_{1,i})^2]$$

$$A_{mix,i} = \pi[(r_{c0} + y_{1,i})^2 - (r_{c0} - y_{2,i})^2] = \pi r_c^2 - A_{g,i} - A_{film,i}$$

Di Matteo's [8] model is based on a "layered model" with the assumption that the mixing zone does not affect the film and mainstream flows but it is a result of their interaction. The developed flow field geometry is based on the one studies by Simon [27] and it takes into account for the mixing, film and core regions.

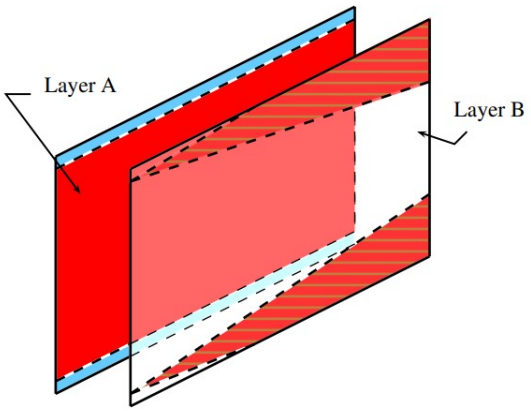

Figure 3.5: Layered model scheme [8]

The film and main stream flows do not influence each other until they enter in the mixing region. In the mixing zone fluid properties are evaluated by the entrained coolant mass and main stream energy inflows. With these assumptions, a layered model is used, where the mixing region is determined by the properties of two uncoupled fluids. The first layer (layer A) is therefore characterized by two parallel fluids flows. The interaction is accounted on a second layer B, where the mixing region is developed. On the B layer only the mixing zone exists and its properties are evaluated by the properties balance of the flows in the A layer. This concept is showed in Figure 3.5. Assuming mass, energy and momentum equations in the form:

$$\frac{\partial U}{\partial t} + \frac{\partial f(U)}{\partial x} = S(U)$$

it is possible to write the governing equations for the A layer (hot gas core and film cooling regions) and B layer (mixing region):

A layer

$$U = A\begin{bmatrix}(\rho)_{film}\\(\rho)_g\\(\rho)_g x^{nc}\\(\rho v)_g\\(\rho E)_{film}\\(\rho E)_g\end{bmatrix}; f(U) = A\begin{bmatrix}(\rho v)_{film}\\(\rho v)_g\\(\rho v)_g x^{nc}\\(\rho v^2+P)_g\\(\rho v h)_{film}\\(\rho v h)_g\end{bmatrix}; S(U) = \begin{bmatrix}0\\0\\0\\-\frac{1}{2}(\frac{d\xi}{dx})\rho v|v|A+\rho g A+P(\frac{dA}{dx})\\(\frac{d\dot{Q}_{film}}{dx})\\(\frac{d\dot{Q}_g}{dx})\end{bmatrix}$$

B layer

$$U = (\rho E A)_{mix}; \quad f(U) = (\rho v h A)_{mix}; \quad S(U) = \frac{d\dot{Q}_{mix}}{dx} + (\rho v h A)_{C2M} + (\rho v h A)_{F2M}$$

The subscripts $C2M$ and $F2M$ indicate a quantity that is exchanged from the core to the mixing region ($C2M$) or from the film to the mixing region ($F2M$). To evaluate the mass flow rates contribute to the mixing region, algebraic equations based on the flowfield geometry are used:

$$\dot{m}_{C2M} = (\rho u)_g A_{C2M}$$

$$\dot{m}_{F2M} = (\rho u)_{film} A_{F2M}$$

the area term represents the interface area between two consecutive regions, determined by the previously described geometry as shown in Figure 3.6:

$$A_{C2M,i} = A_{g,i-1} - A_{g,i}$$

$$A_{F2M,i} = A_{film,i-1} - A_{film,i}$$

To calculate the i-th node temperature the incoming temperature are averaged using their mass flow rates as weights:

$$T_{mix,i} = \begin{cases}\frac{T_{g,i}\dot{m}_{C2M,i}+T_{film,i}\dot{m}_{F2M,i}}{\dot{m}_{C2M,i}+\dot{m}_{F2M,i}} & i=1\\ \frac{T_{g,i}\dot{m}_{C2M,i}+T_{film,i}\dot{m}_{F2M,i}+T_{mix,i-1}\dot{m}_{mix,i-1}}{\dot{m}_{C2M,i}+\dot{m}_{F2M,i}+\dot{m}_{mix,i-1}} & otherwise\end{cases}$$

in the mixing region the mass flow rate is:

$$\dot{m}_{mix,i} = (\dot{m}_{g,i} + \dot{m}_{film,i})\frac{A_{mix,i}}{A_{g,i} + A_{film,i} + A_{mix,i}}$$

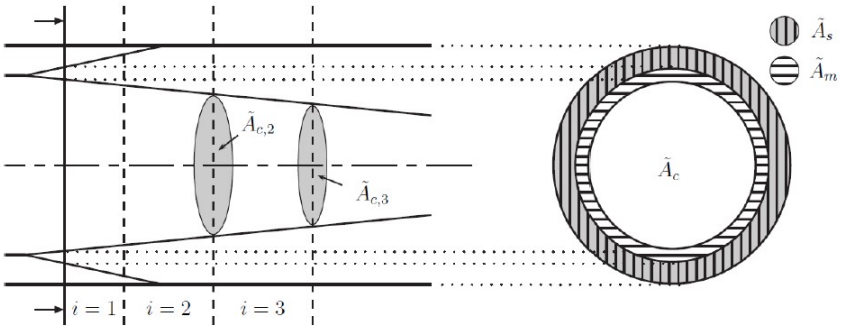

Figure 3.6: Mixing regions scheme [8]

Ultimately, the convective heat transfer coefficient is computed. The Pavli equation [7] provides again an estimation of the heat transfer coefficient based on the Stanton number:

$$St_{Pavli} = 0.023 Re^{-0.2} Pr^{-0.6} \left(\frac{T_{aw}}{T_{ref}}\right)^{0.6} \left(\frac{x}{x_{throat}}\right)^{-0.2}$$

The Stanton number differs in the film region ($x < x_1$) from the mixing region ($x > x_1$):

$$\begin{cases} St_{film} = 0.026 Re_{film}^{-0.2} Pr_{film}^{-0.6} \left(\frac{T_{aw}}{T_{ref}}\right)^{0.6} \left(\frac{x}{x_{th}}\right)^{-0.2} \\ St_{mix} = 0.026 Re_{mix}^{-0.2} Pr_{mix}^{-0.6} \left(\frac{T_{aw}}{T_{ref}}\right)^{0.6} \left(\frac{x}{x_{th}}\right)^{-0.2} \end{cases}$$

D_{th} and x_{th} are throat diameter and abscissa, r_{curv} is the radius of curvature, Re_{film} is the film slot height–based Reynolds number, Pr_{film} is the film Prandtl number, T_{aw} is the adiabatic wall temperature, and T_{ref} is a reference temperature. The convective heat load can be expressed as:

$$\dot{Q}_{conv,i} = (T_{aw,i} - T_{wall,i}) \times \begin{cases} St_{film,i} \rho_{film,i} u_{film,i} c_{p,film,i} & if \;\; x < x_1 \\ St_{mix,i} \rho_{mix,i} u_{mix,i} c_{p,mix,i} & if \;\; x \geqslant x_1 \end{cases} \qquad \left[\frac{W}{m^2}\right]$$

3.6.2 Film cooling injection geometry

A convergent-divergent inlet channel is used to accelerate the coolant from its stagnation conditions to supersonic speed. The driving design condition to obtain its geometry is the equivalence of static pressure at the coolant channel exit and local hot gas static pressure at the injection section. The geometric values come from the isentropic chocked flow equations:

- Coolant channel pressure ratio assuming a stagnation inlet pressure p_c° and and an exit static pressure equal to the local gas static pressure:

$$PR = \frac{p_g}{p_c^\circ}$$

- Coolant exit mach number M_c from the pressure ratio:

$$M_c = \sqrt{\left[(PR)^{-\frac{\gamma_c - 1}{\gamma_c}} - 1\right] \frac{2}{\gamma_c - 1}}$$

- Chocked flow throat area:

$$A_{t,c} = \frac{\dot{m}_c \sqrt{T_c^\circ}}{p_c^\circ} \sqrt{\frac{R_c}{\gamma_c}} \left[\frac{\gamma_c + 1}{2}\right] \frac{\gamma_c + 1}{2(\gamma_c - 1)}$$

- Exit coolant channel area ratio:

$$\frac{A_{e,c}}{A_{t,c}} = \left(\frac{\gamma_c + 1}{2}\right)^{-\frac{\gamma_c + 1}{2(\gamma_c - 1)}} \frac{\left(1 + \frac{\gamma_c - 1}{2} M^2\right)^{\frac{\gamma_c + 1}{2(\gamma_c - 1)}}}{M}$$

Once the coolant channel geometry is set, the leftover parameters are the lip thickness t and the resulting full backward facing step height H as shown in figure 3.7. The effect of changing the lip thickness t has been investigated in the following chapters.

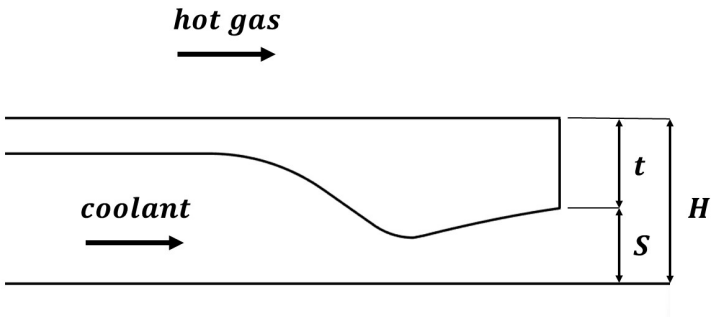

Figure 3.7: Coolant inlet channel geometry scheme

3.7 Isp losses

Two different approaches can be used to estimate the Isp losses due to film cooling:

- Additional coolant as wasted mass flow rate;
- The coolant mass flow rate contributes to the engine thrust without reacting.

Model 1
In the first case the coolant mass flow rate injected on the NE wall is considered as an additional mass flow rate in order to cool the engine without contributing to the thrust of the engine. With these assumptions, the engine thrust is not affected by the coolant mass flow rate, but the Isp. The Isp can be written as:

$$Isp = \frac{T}{\dot{m}g}$$

Where $\dot{m}$ is the propellant mass flow rate without film cooling. If a film cooling mass flow rate $\dot{m}_c$ is present, the new mass flow rate leads to a Isp reduction depending on the film cooling mass flow percentage p:

$$Isp' = \frac{T}{(\dot{m}+\dot{m}_c)g} = \frac{\dot{m}}{\dot{m}+\dot{m}_c}Isp = \frac{1}{1+p}Isp \qquad p = \frac{\dot{m}_c}{\dot{m}}$$

Model 2
The assumption of completely wasted coolant is quite conservative. In a real case, the coolant will accelerate and contribute to the engine thrust, potentially reacting with the core flow and increasing thrust even more. In this second case the coolant mass flow is assumed as a non-reacting expanding gas. The gas properties are computed by means of the isentropic gas expansion laws and its thrust is:

$$T_{film} = \dot{m}_c u_e + A_e(p_e - p_0) = \dot{m}_c \cdot g \cdot Isp_{film}$$

From this equation the film Isp_{film} can be computed and than corrected for nozzle efficiency η and exit angle α as well as the film thrust:

$$Isp_{film,corr} = \eta \cdot Isp_{film} \cdot cos(\alpha) \implies T_{film,corr} = \dot{m}_c \cdot g \cdot Isp_{film,corr}$$

At this point the final engine Isp is computed using the new values of thrust and mass flow rate:

$$Isp' = \frac{T + T_{film,corr}}{g \cdot (\dot{m}+\dot{m}_c)}$$

Chapter 4

CFD model

In this chapter all the assumption for the NE CFD model are presented. The chapter contains the details of the NE geometry and computational grid for both uncooled and film cooled NE cases. The tested combustion models are listed as the custom definition of chemical species properties. The thermal model and the equations needed to calculate NE parameters are described.

4.1 Geometry

The tested geometry from the Huracán engine includes the convergent-divergent channel of the MCC and the parabolic NE. This geometry has been provided by The Exploration Company for simulation. The barrel section of the combustion chamber has not been simulated, therefore the boundary conditions at the convergent inlet are assumed to be equal to the stagnation properties of the barrel section of the combustion chamber. Stagnation pressure and temperature are provided by the company as well as the initial hot gas composition in terms of mass fractions. This composition was obtained by an equilibrium combustion computation and used as initial condition for the expansion since the gas velocity in the barrel section of the combustion chamber is usually order of magnitude lower than the chemical reaction velocity. Thus, all reactions reach equilibrium and the composition is used as a boundary condition. The outlet boundary conditions are used only for flowfield initialization since the outlet is supersonic. Due to the axisymmetric geometry of a rocket engine nozzle, all the CFD computations will be performed on a 2D geometry with axisymmetric model. When the axisymmetric model is selected on the CFD software, the entire 2D geometry is assumed to have an angular thickness of 1 rad, therefore when it comes to integrate on a surface perpendicular to the model axis the integral on the radius only has to be multiplied by 2π. The specifications of the geometry for both uncooled and film cooled NE cases are presented in the following section.

4.1.1 Uncooled NE case

The simple geometry of the convergent-divergent nozzle is imported as a 2D spline on the CFD software. The spline is then closed with an inlet, an outlet and an axis coincident with the x-axis for the axisymmetric model. To simulate the wall thermal behavior, the NE wall has been thickened by a 2 mm extrusion and the resulting geometry is shown in Figure 4.1.

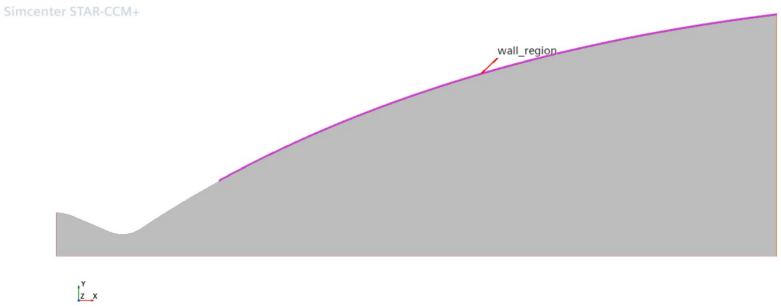

Figure 4.1: NE geometry, the solid wall is highlighted

4.1.2 Film cooled NE case

The film cooling injection geometry is imported on the original geometry. A secondary inlet is therefore created. On this inlet the coolant boundary conditions are applied. The main function of the coolant inlet channel is to provide the film cooling mass flow rate at the design conditions, therefore it features a convergent-divergent geometry in order to accelerate the gaseous coolant up to supersonic speed to the point where the static coolant pressure equals the local hot gas static pressure (at least in design conditions) as described in subsection 3.6.2. Figure 4.2 shows the details of the coolant channel geometry. Note that the half convergent-divergent channel is reversed with respect to the geometry presented in subsection 3.6.2. The inlet surface where stagnation pressure and temperature boundary conditions are applied corresponds to the gaseous coolant distribution manifold.

(a) NE geometry

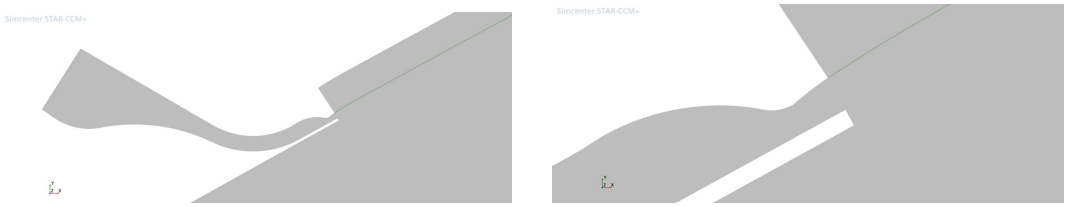

(b) Film cooling injection detail (c) Convergent-divergent detail

Figure 4.2: Film cooling geometry

4.2 Computational grid

The CFD computation requires a computational grid to be performed. A grid for the uncooled and film cooled NE cases are crated with the same idea. The main difference between the two cases is the scale of the geometry. In the first case a simple uniform grid is adopted for the entire domain whilst in the second case the coolant injection requires a local refinement to capture the main characteristics of the smaller convergent-divergent injection channel.

4.2.1 Uncooled NE case

For the uncooled NE case the computational grid features a radius based refinement. The local MCC and NE radius is divided in 100 polygonal elements. A prism layer is added on the wall of the fluid domain to capture the boundary layer evolution. On the solid wall a quadrilateral mesh with 20 elements per axial position has been implemented. The solid wall model only features conduction and since the only radiating surface is the external surface, no more refinement is required.

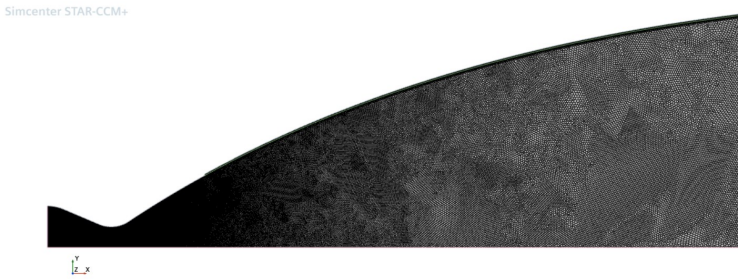

Figure 4.3: Surface mesh

4.2.2 Film cooled NE case

The film cooled NE case features two geometry on two different scales. The main MCC and NE geometry refinement is equal to the uncooled NE case with 100 elements on the radius for each axial position. The film cooling injection channel

features a custom local refinement around the injection zone as shown in Figure 4.4. The refinement is needed because of the compressibility phenomenon that take place at the injection point. On the other side no particular refinement is needed in the previous feeding channel from the distribution manifold.

(a) Global surface mesh

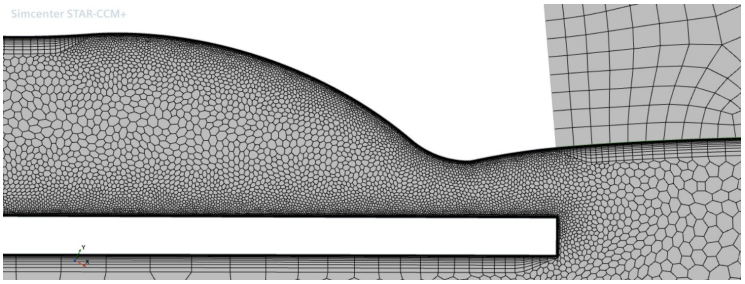

(b) Coolant convergent-divergent mesh detail

Figure 4.4: Film cooled NE case surface mesh

The following table compares the grid number of elements for both cases. The addition of the coolant geometry with a proper local refinement greatly increases the computational cost of the simulation.

Grid	Cells	Faces	Vertices
Uncooled NE	112247	319726	209181
Film cooled NE	383241	943976	586244

Table 4.1: Number of elements for each grid

4.3 Combustion models

When a hot gas expands through a rocket nozzle, it is hard to determine how the chemical reactions take place. Generally, two different physical points of view represent the extreme cases: frozen flow and shifting equilibrium. It is well known that,

in a real case, the flow characteristics sit in between these two cases, providing a useful range of temperature and pressures that one can expect from the real reacting flow. Combustion models aim to refine the prediction of the flow behaviour involving a specific definition of the chemical kinetic. These models heavily rely on experimental data for calibration, providing equations and constants to be used in CFD software. The downside of implementing a chemical kinetic model is the increasing computational cost, because every reaction involved in a model adds to the number of equation that the software has to solve for each iteration. The scientific community has provided multiple combustion models for different propellant combinations and environments, from simple and reduced order mechanism to complex and high-number-equations schemes. In this thesis, different models involving different number of species and equations have been investigated. The parameters in the following tables are referred to the Arrhenius equation described in subsection 2.4.2:

$$k_{f/b,j} = AT^{\beta}e^{-\frac{E_a}{RT}}$$

4.3.1 Frozen flow

In the frozen model, no reaction takes place between the chemical species, therefore the composition, in terms of mass fractions, is constant during the expansion in the nozzle. From a physical point of view it represents the case in which the flow velocity is orders of magnitude higher than the chemical reactions velocity.

4.3.2 2S-CM2 mechanism

The 2S-CM2[3] mechanism is a simple reduced order two step global reaction mechanism for methane combustion, implemented in multiple commercial CFD software. It involves 5 species and 3 reactions: the methane combustion and the dissociation of CO_2. The following table summarizes the reactions and the constant values for each:

Reactions	A	β	E_a	Reaction orders
$CH_4 + 1.5O_2 \rightarrow CO + 2H_2O$	2×10^{15}	0.000	35000	$[CH_4]^{0.9}[O_2]^{1.1}$
$CO + 0.5O_2 \rightarrow CO_2$	2×10^{9}	0.000	12000	$[CO][O_2]^{0.5}$
$CO_2 \rightarrow CO + 0.5O_2$	8.1104×10^{10}	0.000	77194	$[CO_2]$

Table 4.2: 2S-CM2[3] mechanism (units in cm, s, cal, mol)

4.3.3 Jones Linstedt mechanism

The Jones-Linstedt [16] mechanism is a simple hydrocarbons kinetic combustion model based on 4 reactions:

$$\begin{cases} C_nH_{2n+2} + \frac{n}{2}O_2 \rightarrow nCO + (n+1)H_2 \\ C_nH_{2n+2} + nH_2O \rightarrow nCO + (2n+1)H_2 \\ H_2 + \frac{1}{2}O_2 \longleftrightarrow H_2O \\ CO + H_2O \longleftrightarrow CO_2 + H_2 \end{cases}$$

In the case of methane combustion $n = 1$. This model has been widely used and modified but in this work its original form is used. The original coefficients for the Arrhenius equation are listed in the following table:

Reactions	A	β	E_a	Reaction orders
$CH_4 + 0.5O_2 \rightarrow CO + 2H_2$	7.82×10^{13}	0.000	30000	$[CH_4]^{0.5}[O_2]^{1.25}$
$CH_4 + H_2O \rightarrow CO + 3H_2$	3.0×10^{12}	0.000	30000	$[CH_4][H_2O]$
$H_2 + 0.5O_2 \longleftrightarrow H_2O$	1.209×10^{18}	-1.000	40000	$[H_2]^{0.25}[O_2]^{1.5}$
$CO + H_2O \longleftrightarrow CO_2 + H_2$	2.75×10^{12}	0.000	20000	$[CO][H_2O]$

Table 4.3: Jones Linstedt[16] mechanism (units in cm, s, cal, mol)

4.3.4 Zhukov mechanism

The most complex mechanism implemented is the one developed by Zhukov[30] for the oxidation of alkanes and involves 23 species and 51 reactions:

Reactions	A	β	E_a
$O_2 + CH_2O \longleftrightarrow HO_2 + HCO$	1.000×10^{14}	0.000	40000.00
$H + O_2 + M \longleftrightarrow HO_2 + M$	2.800×10^{18}	-0.860	0.00
$H + 2O_2 \longleftrightarrow HO_2 + O_2$	3.000×10^{20}	-1.720	0.00
$H + CH_2O(+M) \longleftrightarrow CH_3O(+M)$	5.400×10^{11}	0.454	2600.00
$2OH(+M) \longleftrightarrow H_2O_2(+M)$	7.400×10^{13}	-0.370	0.00
$OH + HO_2 \longleftrightarrow O_2 + H_2O$	2.900×10^{13}	0.000	-500.00
$OH + H_2O_2 \longleftrightarrow HO_2 + H_2O$	1.750×10^{12}	0.000	320.00
$OH + H_2O_2 \longleftrightarrow HO_2 + H_2O$	5.800×10^{14}	0.000	9560.00
$OH + CH_4 \longleftrightarrow CH_3 + H_2O$	1.000×10^{08}	1.600	3120.00
$2HO_2 \longleftrightarrow O_2 + H_2O_2$	1.300×10^{11}	0.000	-1630.00
$2HO_2 \longleftrightarrow O_2 + H_2O_2$	4.200×10^{14}	0.000	12000.00
$HO_2 + CH_3 \longleftrightarrow O_2 + CH_4$	1.000×10^{12}	0.000	0.00

$HO_2 + CH_3 \longleftrightarrow OH + CH_3O$	2.000×10^{13}	0.000	0.00
$HO_2 + CO \longleftrightarrow OH + CO_2$	1.500×10^{14}	0.000	23600.00
$HO_2 + CH_2O \longleftrightarrow HCO + H_2O_2$	1.000×10^{12}	0.000	8000.00
$CH_3 + O_2 \longleftrightarrow O + CH_3O$	2.675×10^{13}	0.000	28800.00
$CH_3 + O_2 \longleftrightarrow OH + CH_2O$	3.600×10^{10}	0.000	8940.00
$CH_3 + H_2O_2 \longleftrightarrow HO_2 + CH_4$	2.450×10^{04}	2.470	5180.00
$CH_3 + CH_2O \longleftrightarrow HCO + CH_4$	3.320×10^{03}	2.810	5860.00
$CH_3O + HO_2 \longleftrightarrow CH_2O + H_2O_2$	1.200×10^{13}	0.000	0.00
$CH_3O_2 + CH_3 \longleftrightarrow CH_3O + CH_3O$	3.000×10^{13}	0.000	-1200.00
$CH_3O + O_2 \longleftrightarrow HO_2 + CH_2O$	4.280×10^{-13}	7.600	-3530.00
$CH_3 + O_2 \longleftrightarrow CH_3O_2$	1.700×10^{60}	-15.100	18785.00
$CH_3O + CH_3 \longleftrightarrow CH_2O + CH_4$	2.410×10^{13}	0.000	0.00
$O + CH_4 \longleftrightarrow OH + CH_3$	1.020×10^{09}	1.500	8600.00
$H + O_2 \longleftrightarrow O + OH$	8.300×10^{13}	0.000	14413.00
$H + O_2 + H_2O \longleftrightarrow HO_2 + H_2O$	9.380×10^{18}	-0.760	0.00
$O + H_2 \longleftrightarrow H + OH$	5.000×10^{04}	2.670	6290.00
$O + CH_3 \longleftrightarrow H + CH_2O$	8.430×10^{13}	0.000	0.00
$O + CO + M \longleftrightarrow CO_2 + M$	6.020×10^{14}	0.000	3000.00
$H + OH + M \longleftrightarrow H_2O + M$	2.200×10^{22}	-2.000	0.00
$H + CH_3(+M) \longleftrightarrow CH_4(+M)$	1.270×10^{16}	-0.630	383.00
$H + HCO(+M) \longleftrightarrow CH_2O(+M)$	1.090×10^{12}	0.480	-260.00
$H + C_2H_4(+M) \longleftrightarrow C_2H_5(+M)$	1.080×10^{12}	0.454	1820.00
$H + C_2H_4 \longleftrightarrow C_2H_3 + H_2$	1.325×10^{06}	2.530	12240.00
$H + C_2H_6 \longleftrightarrow C_2H_5 + H_2$	1.150×10^{08}	1.900	7530.00
$OH + H_2 \longleftrightarrow H + H_2O$	2.160×10^{08}	1.510	3430.00
$OH + CH_2 \longleftrightarrow H + CH_2O$	2.000×10^{13}	0.000	0.00
$OH + C_2H_6 \longleftrightarrow C_2H_5 + H_2O$	3.540×10^{06}	2.120	870.00
$HCO + O_2 \longleftrightarrow HO_2 + CO$	7.600×10^{12}	0.000	400.00
$HCO + M \longleftrightarrow H + CO + M$	1.870×10^{17}	-1.000	17000.00
$CH_3 + OH \longleftrightarrow CH_2O + H_2$	8.000×10^{12}	0.000	0.00
$CH_2 + CH_3 \longleftrightarrow H + C_2H_4$	4.000×10^{13}	0.000	0.00
$O_2 + CO \longleftrightarrow O + CO_2$	2.500×10^{12}	0.000	47800.00
$OH + CO \longleftrightarrow H + CO_2$	4.760×10^{07}	1.228	70.00
$OH + CH_2O \longleftrightarrow HCO + H_2O$	3.430×10^{09}	1.180	-447.00
$H + CH_2O \longleftrightarrow HCO + H_2$	2.300×10^{10}	1.050	3275.00
$H + CH_4 \longleftrightarrow CH_3 + H_2$	6.600×10^{08}	1.620	10840.00
$2CH_3(+M) \longleftrightarrow C_2H_6(+M)$	2.120×10^{16}	-0.970	620.00
$H + O_2 + N_2 \longleftrightarrow HO_2 + N_2$	2.600×10^{19}	-1.240	0.00
$H + O_2 + Ar \longleftrightarrow HO_2 + Ar$	7.000×10^{17}	-0.800	0.00

Table 4.4: Zhukov[30] mechanism (units in cm, s, cal, mol)

4.3.5 Shifting equilibrium

With the equilibrium model, the software relaxes the species composition in each cell to the local equilibrium composition. It is assumed, therefore, that the flow velocity is order of magnitude smaller than the chemical reactions velocity and all the reactions reach equilibrium.

4.4 Transport properties

Custom definition of dynamic viscosity and thermal conductivity are implemented in the simulation software. A correlation based on temperature T was proposed by Gordon, McBride and Reno[13]:

$$A \ln T + \frac{B}{T} + \frac{C}{T^2} + D = \begin{cases} \eta \\ \lambda \end{cases}$$

Where η is the dynamic viscosity and λ is the thermal conductivity. The coefficients A, B, C and D are tabulated for different temperature ranges (300-1000 K and 1000-5000 K) for each chemical species as in the following example:

```
CH4                              V2C2  GORDON; NASA TM86885, OCT 1984
 V  300.000 1000.000 0.57388074E 00-0.98544160E 02 0.20012204E 04 0.17536015E 01
 V 1000.000 5000.000 0.65074534E 00 0.23936771E 02-0.22020183E 05 0.11244058E 01
 C  300.000 1000.000 0.11770360E 01-0.17422121E 03 0.22865563E 05-0.55146852E 00
 C 1000.000 5000.000 0.49214767E 00-0.91598343E 03 0.87265127E 05 0.48489412E 01
```

Figure 4.5: Transport properties coefficients for methane

4.5 External radiation

A simple grey-body emissivity model is implemented. It is assumed that the body has a known emissivity ε as a free parameter. The general equation for the radiation heat flux for a grey-body is:

$$q = \varepsilon\sigma(T_1^4 - T_2^4) \qquad \left[\frac{W}{m^2}\right]$$

where q is the heat flux, T_1 and T_2 are the temperature of the hot and cold bodies, σ is the Stefan-Boltzmann constant. In this case the hot body is the nozzle extension and the cold temperature refers to the external ambient temperature. The latter is assumed to be equal to $0K$ as a first approximation. In the real case of the Huracán engine, it will be crucial to evaluate the external heat flux considering the coupling with the other spacecraft engines. The CFD model, as well as the 1D model, considers the external heat flux as a cooling effect however the nozzle extension will face the

nozzle extensions of the other engines, reducing the cooling effect and potentially threatening the engine survival. Future analysis will determine the coupled mutual heating effect of each engine based on their spacing and arrangement. The previous simple radiation equation has been implemented as a field function in the CFD software and applied to the external NE wall as a heat flux boundary condition, where T is the temperature of the wall surface cell.

4.6 Fluid/solid coupling

In order to evaluate the NE performance, a thin solid wall is implemented in the simulation. A structured grid is used in the solid region because of the very simple geometry of the NE in a 2D simulation. The fluid and solid domains thus share an interface that allows the calculation of convective heat transfer of the side wall of the hot gas and conduction within the solid. A customised material definition is used. Tables from the manufacturer's material datasheet are imported for the definitions of specific heat and thermal conductivity as a function of temperature. The software assumes a stationary heat transfer state for the calculation.

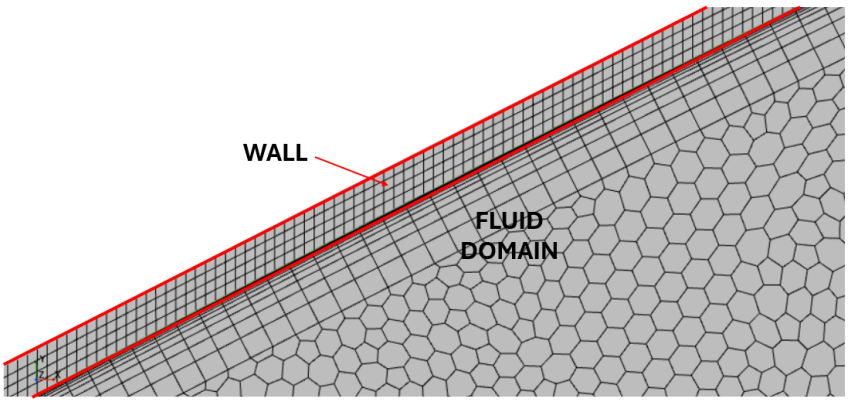

Figure 4.6: Wall-fluid domain interface

4.7 MCC wall

In order to get a correct flow field for the nozzle extension, a complete convergent-divergent nozzle geometry has been used. The MCC is regeneratively cooled, therefore the CFD model described would not be suitable for a heat flux calculation. Since the MCC is not the focus of this thesis, the regenerative cooling channels are not implemented in the model. However it is not possible to ignore the thermal behavior of the MCC. Since the temperature in the MCC is considerably higher than in the NE (which is why it needs the regenerative cooling), the use of an adiabatic wall

condition on it would lead to a strong axial temperature gradient on the NE. In a real case, without any film cooling, it is expected to see a sudden raise in temperature at the beginning of the NE due to the end of the regenerative cooling circuit.

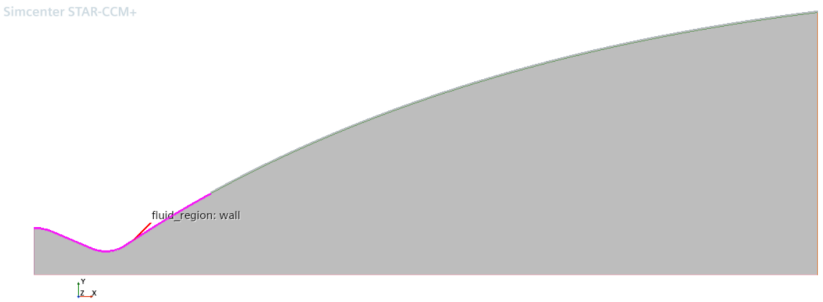

Figure 4.7: The MCC wall is highlighted

With an adiabatic wall as a boundary condition on the MCC wall, a temperature decrease from the adiabatic wall temperature of the MCC to the thermal equilibrium external radiation temperature of the NE is noted instead. To get around this problem the hot-gas side wall temperature of the MCC is imposed as a wall boundary condition. The temperature envelope has been provided by The Exploration Company's internal MCC wall temperature estimation. The figure 4.7 shows the MCC wall where the provided temperature envelope is applied as a boundary condition.

4.8 CFD film cooling Isp losses

In order to compare the Isp losses due to film cooling between the analytical model and the CFD computation, the engine performance parameters must be calculated. The Isp is defined as follows:

$$Isp = \frac{T}{\dot{m}g}$$

Thrust T and propellant mass flow rate $\dot{m}$ at the outlet have to be computed from the 2D simulation. Taking the outlet nozzle surface as reference and its axis as the origin, the desired parameters can be calculated with the following integrals:

$$\begin{cases} \dot{m} = \int_{A_{exit}} \rho u dA = \int_{A_{exit}} \rho(x,y)u(x,y)dxdy \\ T = \int_{A_{exit}} (\rho u^2 + p)dA = \int_{A_{exit}} [\rho(x,y)u(x,y)^2 + p(x,y)]dxdy \end{cases}$$

The equation of thrust should include also the environment outer pressure. In this case the outer pressure is set to zero since the engine operates in near vacuum

conditions. In a polar reference system the integrals for thrust and mass flow rate are:

$$\begin{cases} \dot{m} = \int_{A_{exit}} \rho(r)u(r)rdrd\theta = \int_{2\pi} d\theta \int_r \rho(r)u(r)rdr \\ T = \int_{A_{exit}} [\rho(r)u^2(r) + p(r)]rdrd\theta = \int_{2\pi} d\theta \int_r [\rho(r)u^2(r) + p(r)]rdr \end{cases}$$

The CFD simulation provides the distributions of density ρ, normal velocity u and pressure p for the engine outlet for each cell. The integrals are approximated with the finite sum:

$$\begin{cases} \dot{m} \approx 2\pi \sum_i \rho_i u_i r_i \Delta r_i \\ T \approx 2\pi \sum_i (\rho_i u_i^2 + p_i) r_i \Delta r_i \end{cases}$$

Chapter 5

Results

In this chapter the results of the CFD computations and the analytical model are presented. In particular, each CFD model step is investigated to highlight the influence of each hypothesis. Different boundary conditions are used to determine the film cooling performances and a comprehensive comparison with the developed analytical model is presented.

5.1 Grid convergence analysis (uncooled NE)

A grid convergence analysis is required to estimate the simulation capability to approximate the solution. Three different grids (coarse, medium and fine) are implemented to perform the grid convergence analysis. The convergence order p is measured using three reference parameters for each level of refinement:

$$p = \frac{\frac{g_3 - g_2}{g_2 - g_1}}{ln(r)}$$

	maximum axis mach number	minimum axis density	throat wall pressure
p	2.76	3.04	1.75

The values g_3, g_2 and g_1 represent the values of the reference parameter for each grid. The subscripts (1), (2), (3) are respectively the coarse, medium and fine grids. r is the refinement ratio used to refine the grid and is equal to 2. The reference parameters used are the maximum axis mach number, the minimum axis density and the throat wall pressure.

5.1.1 Richardson extrapolation

A Richardson extrapolation with measured order p is performed to estimate the exact solution for the reference parameters. To keep the refinement ratio the same

Grid	Cells	Faces	Vertices	max axis mach number	min axis density	throat wall pressure
Coarse	11113	28299	17698	8.84656	0.00102974	1.338917×10^6
Medium	33546	90826	58246	8.63106	0.00111857	1.338621×10^6
Fine	112247	319726	209181	8.59932	0.00112939	1.337623×10^6

Table 5.1: Reference parameters for each grid

between the coarse - medium and medium -fine grids, the number of elements per radius has been doubled going from the coarse to medium and fine grid. The extrapolation can be performed with the following equation:

$$g_0 = g_1 + \frac{g_1 - g_2}{r^p - 1}$$

The results for each parameter are shown in the following table:

	max axis mach number	min axis density	throat wall pressure
Coarse	8.84656	0.00102974	1.338917×10^6
Medium	8.63106	0.00111857	1.338621×10^6
Fine	8.59932	0.00112939	1.337623×10^6
Extrapolated	8.5938377	0.0011309	1.339042796×10^6

Table 5.2: Reference parameters and extrapolated values

5.1.2 Grid convergence index

To report the grid covergence quality, the Grid convergence index (GCI) is computed. It is calculated for each refinement steps therefore 2 GCI are computed for each reference parameter in this case. The equation for GCI is:

$$GCI = \frac{F_s|e|}{r^p - 1}$$

where F_s is an optional safety factor and e is the relative error between the two grids:

$$e = \frac{g_1 - g_2}{g_1}$$

Once the GCI is computed, it is possible to evaluate the asymptotic range of convergence. If the solution is not in the asymptotic range it means that the computation

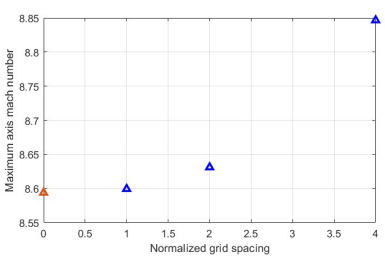

(a) Maximum axis mach number

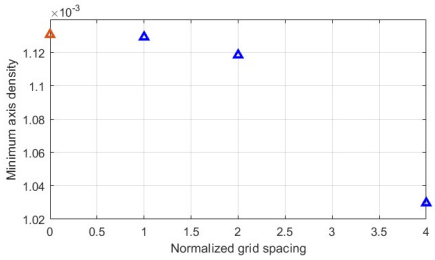

(b) Maximum axis density

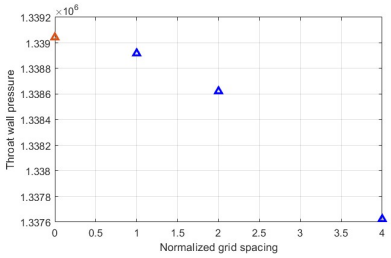

(c) Throat wall pressure

Figure 5.1: Richardson extrapolation for reference parameters

	max axis mach number	min axis density	throat wall pressure
$GCI_{2,3}$	1.2938%	3.3044%	0.0944%
$GCI_{1,2}$	0.1913%	0.3986%	0.0280%

Table 5.3: Grid convergence index for each refinement step

is not asymptotically approaching a converged solution and thus the solution is not grid independent. To evaluate the asymptotic range of convergence, the following equation is used:

$$A = \frac{GCI_{2,3}}{r^p \times GCI_{1,2}} \approxeq 1$$

If the solution is in the asymptotic range of convergence then A should be approximately equal to 1. The results are shown in the following table. The fine grid is the one adopted for the computations on the uncooled NE case.

	max axis mach number	min axis density	throat wall pressure
A	0.9963226	1.0096731	1.0002213

Table 5.4: Asymptotic range of convergence evaluation

5.2 Grid convergence analysis (film cooled NE)

The computational grid for the film cooled NE case described in subsection 4.2.2 features two different geometries on two different scales. This makes impractical to evaluate the grid convergence properties using the same strategy used for the uncooled NE case. It is indeed harder to refine the grid with a constant refinement factor between coarse, medium and fine grids. In order to have a better understanding of the film cooled NE case grid convergence, an analysis based exclusively on the outputs has been performed. The reference parameter used to evaluate the grid convergence is the wall temperature, since it is the one mainly influenced by the film cooling and one of the most important outputs of this work. The grid has been refined doubling the base size of the elements around the coolant injection and the wall. The rest of the grid keeps the characteristics of the uncooled NE version. This has been done to check the validity of the region around the film cooling injection which is the one that determines the film cooling behavior. The resulting number of elements for each grid is shown in the following table:

Grid	Cells	Faces	Vertices
Coarse	233764	570683	361886
Medium	268067	650097	407183
Fine	383270	944063	586302

Table 5.5: Grids number of elements

Figure 5.2a compares the NE wall temperature for the three grids. Refining the grid doesn't change the solution of more than 4% from the coarse to the medium and for a maximum of around 1% going from the medium to the fine (Figure 5.2b). Further refinement of the grid could improve the solution but not provide any more useful information about the wall temperatures.

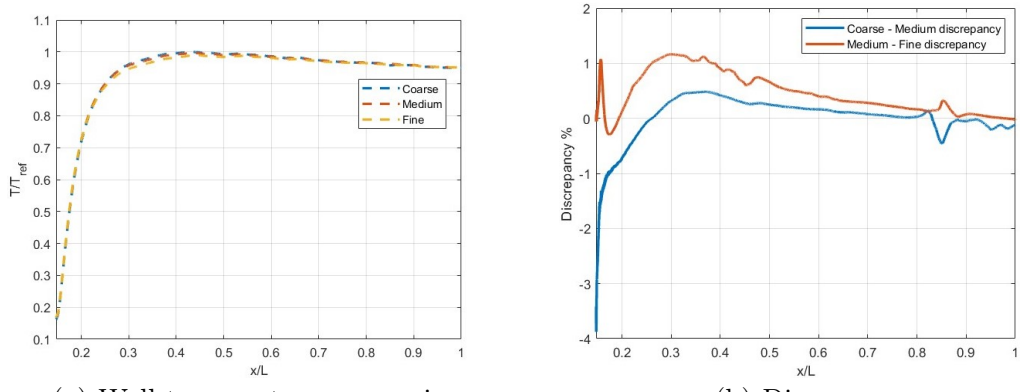

(a) Wall temperature comparison (b) Discrepancy

Figure 5.2: Wall temperature differences between grids

5.3 Uncooled NE

To better understand the influence of each CFD model variation, the influence of each simulation improvement step has been investigated following the same logic described in chapter 4.

5.3.1 Flowfield geometry

As expected, the nozzle accelerates the hot gas up to supersonic speed while its temperature and pressure decrease due to the strong expansion. Figure 5.3 shows the mach number, temperature and pressure contours in the nozzle for a chemical equilibrium computation.

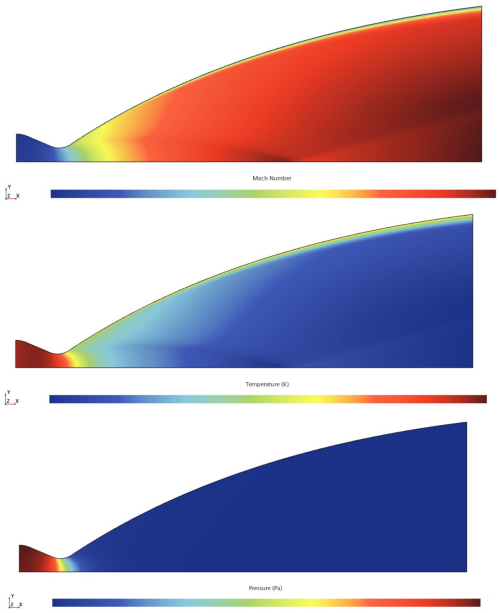

Figure 5.3: Mach number, temperature and pressure contours

The temperature contour clearly shows the increase of temperature near the wall. The gas flowing near the wall are slowed by the interaction with the boundary layer where viscosity exchanges kinetic energy for heat, increasing local temperature and, therefore, the wall temperature approaches the gas recovery temperature. In this computation the wall is adiabatic so the wall temperature is equal to the adiabatic wall temperature. Moreover, a shock wave is formed and is particularly visible in the mach and temperature contours. This shock wave is due to the strategy adopted to design the NE. The geometry is a Thrust Optimized Parabolic (TOP) arc which means that the divergent part of the MCC is connected with a parabolic arc to complete the divergent geometry. The TOP geometry differs from other geometries such as the Truncated Ideal Contour (TIC) because of the not shock-free flowfield. The TIC geometry is obtained from the carachteristic lines in order to produce a shock-free flowfield. In a non viscous case the TIC geometry would lead to an isentropic convergent-divergent nozzle. In TOP geometries a shock wave originates from the flex point of the contour, where the second derivative changes its sign. The advantage of a TOP geometry over a TIC geometry is the higher value of exit pressure that gives to the TOP nozzle a higher margin against flow separation [9]. Despite the name, the TOP is not by any means the highest possible thrust geometry. Depending on the design, a TIC nozzle could provide more thrust than a TOP nozzle, however the TOP geometry provides the highest possible thrust for a parabolic contour. The shock wave has a curved profile, due to the changes in the

speed of sound with the decreasing temperature. At least for the equilibrium case, this shock wave reflects on the axis.

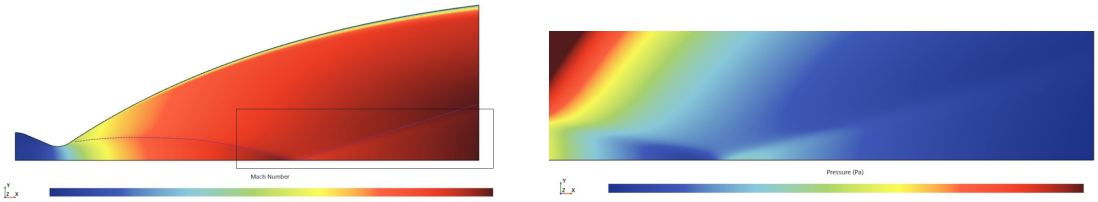

(a) Mach number contour (b) Balanced pressure contour detail

Figure 5.4: Shock wave overview

The shock wave is highlighted in figure 5.4a. The shock wave compression effect is clearly visible in a balanced pressure contour in Figure 5.4b around the reflection zone.

5.3.2 Combustion models comparison

Part of the work of this thesis consists in comparing different combustion models to simulate the NE flowfield. It is important to compare combustion models since it is well known that real rocket engine performance sits in between two extreme cases. Frozen composition and shifting equilibrium represent these two extreme cases. In a frozen case, the species mass fraction remain the same during the entire expansion in the nozzle. In a real rocket engine combustion takes place however the flow behaviour, especially in the last part of the divergent, usually performs closer to a frozen case. This is due to the fact that the gas speed is greatly increased by the expansion to the point where the chemical reactions do not have time to take place. On the other hand, in a shifting equilibrium case all chemical reactions reach the equilibrium in each part of the nozzle. This is true in the barrel section of the MCC and the first part of the convergent, where the speed is low compared to the chemical reaction speed. Therefore neither the shifting equilibrium nor the frozen composition model are able to capture the real hot gas expansion behavior. Combustion model try to approximate better the flowfield behavior by modeling how the chemical species react with each

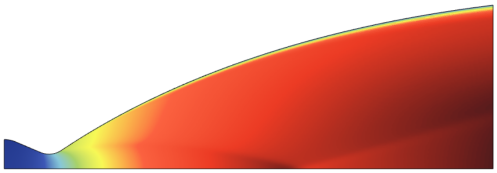

Figure 5.5: Equilibrium

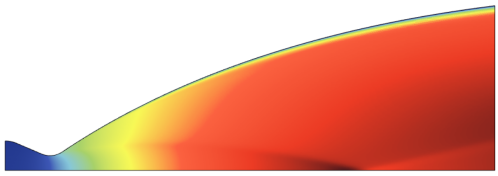

Figure 5.6: Zhukov mechanism

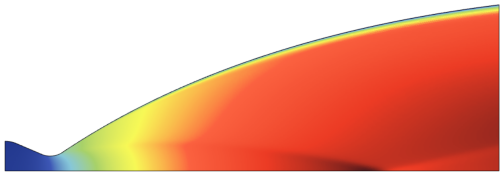

Figure 5.7: 2S-CM2 mechanism

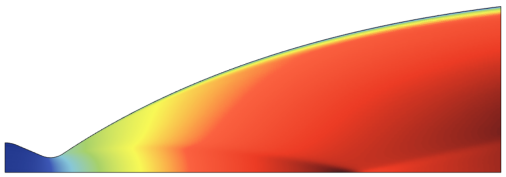

Figure 5.8: Jones-Linstedt mechanism

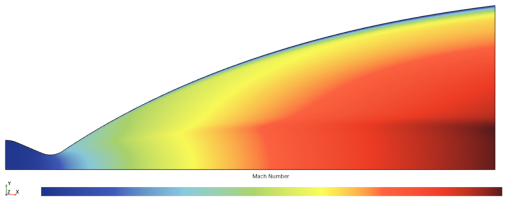

Figure 5.9: Frozen

other. Each combustion models involves a number of chemical species and reactions. A lot of effort has been put on by the scientific community to create detailed kinetic chemical models for each combustion case (methane-oxygen combustion in this case). Typically, more complex combustion models (where more complex means more species and reactions involved) lead to better approximations of the real case. On the other side, including more reactions and species requires a higher computing time since each species adds an equation to solve as described in subsection 2.4.2.
The three combustion models investigated in this thesis feature different number of species and equations as shown in the following table:

Combustion model	Number of species	Number of reactions
Zhukov	23	51
2S-CM2	5	3
Jones-Linstedt	6	4

Table 5.6: Combustion models structure

The first observation that can be made by just analyzing the flowfield from Figure 5.5 to Figure 5.9 is the shape of the shock wave. The position of the point where the shock reflects moves further down the nozzle axis moving from the equilibrium (where it reflects on the rearmost position) to combustion models and frozen model. The frozen model is the only one where the shock wave flows out of the nozzle without reflecting on the axis inside the engine. The frozen model, moreover, features the highest exit mach number (while the equilibrium, the lowest). This is due to the lower overall temperature in a frozen model computation rather than an equilibrium one. If the composition is frozen, no chemical reactions take place and no energy is released from combustion. The lower temperatures lead to lower values of speed of sound and, therefore, higher mach numbers. In the same way, the curvature change of the shock wave is due to the change in hot gas properties with temperature. The position of the shock reflection for the combustion models sits in between the frozen and chemical equilibrium cases, as expected. The effect of the shock reflection can be seen also on the axis temperature and pressure as shown in Figure 5.10. The shock wave reflection creates a local spike in temperature and pressure since after the shock

wave static temperature and pressure increase. In the frozen case this is not true since the shock wave flows out of the nozzle. The 1D model, of course, is not able to predict shock waves or their interaction with the flowfield. However, The 1D model provides a good estimation of equilibrium and frozen axial temperature and pressure. The combustion models, as expected, sit in between the equilibrium and frozen cases for both temperature and pressure. The only exception is the axis temperature in the MCC for the JL [16] mechanism which computes a lower combustion temperature in the convergent. Temperature and pressure in Figure 5.10 are normalised for their maximum values T_{ref} and p_{ref}, corresponding to the MCC combustion temperature and pressure. The x abscissa is normalised for the divergent axial length, therefore a zero axial position corresponds to the nozzle throat and a negative axial position corresponds to the convergent part of the nozzle.

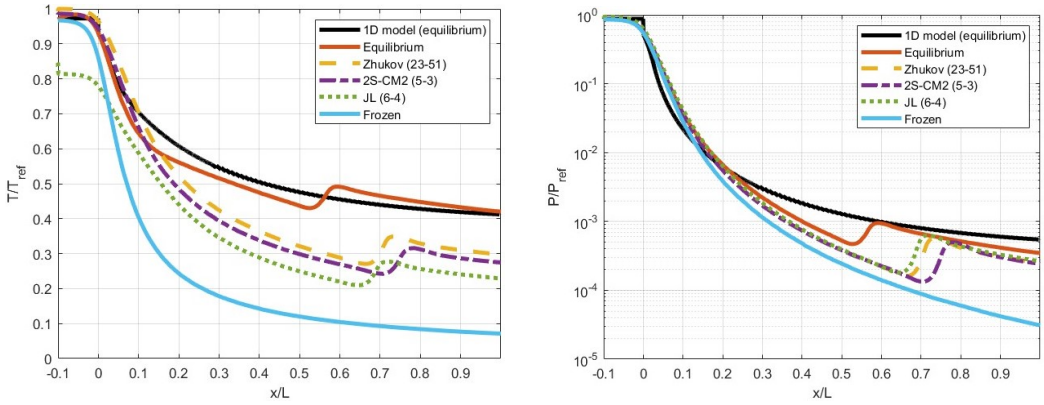

(a) Axis temperature

(b) Axis pressure

Figure 5.10

Figure 5.11 compares the mass fraction of the main hot gas components, normalised for their initial value.

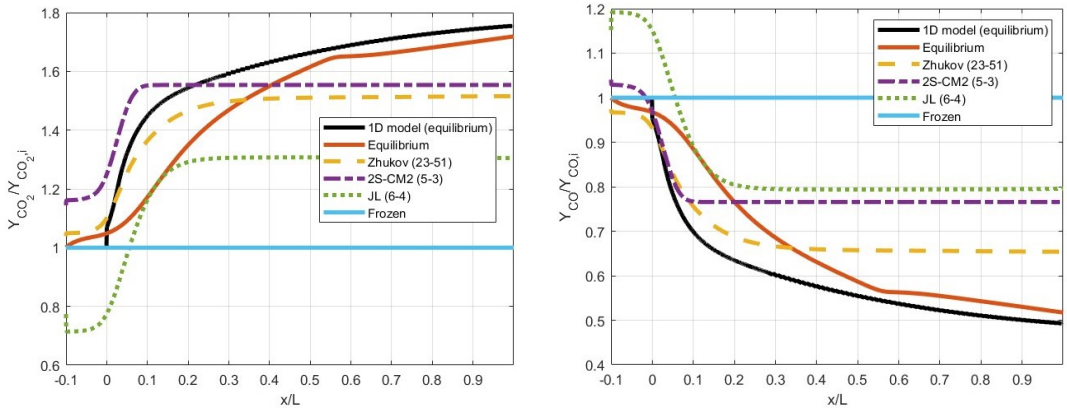

(a) Axis CO_2 mass fraction

(b) Axis CO mass fraction

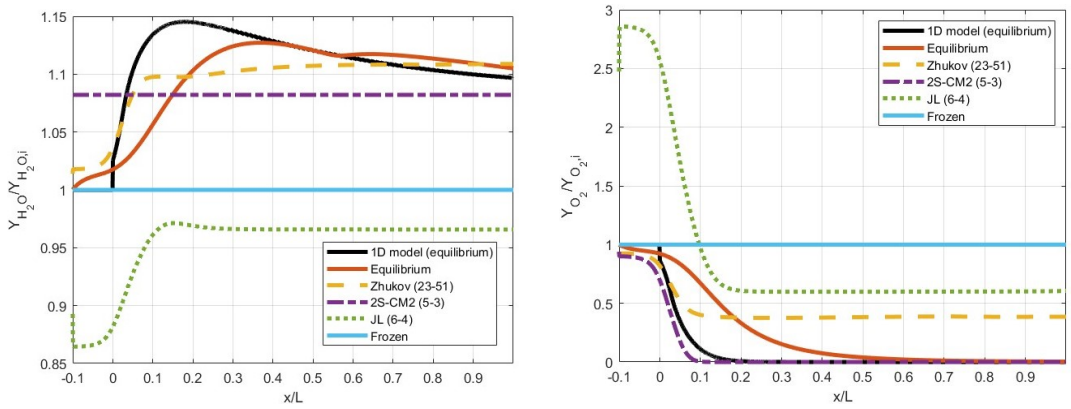

(c) Axis H_2O mass fraction (d) Axis O_2 mass fraction

Figure 5.11: Main gas component mass fractions

The simulations use the same initial composition except for the 2S-CM2 and JL combustion models where the initial composition have been normalised on the species of each model to keep the sum of mass fractions to 1. This is why the initial value of mass fraction appears to be off compared to the others in Figure 5.11 for these two models. Globally, all the mass fraction show the same behavior. The mass fraction of H_2O for the 2S-CM2 model remains constant because the model does not involve any reaction in which H_2O is generated except for the methane combustion. However, the initial methane mass fraction is equal to zero since the initial composition comes from an equilibrium combustion chamber calculation. The JL model, as for the temperature, shows a different behavior especially in the convergent part of the MCC. On the other side it keeps the same trend of the other models for each species. The equilibrium model is the only one affected by the shock reflection. It is clearly visible a change in the trend of the mass fractions in the equilibrium case that corresponds to the same axial position of the shock reflection visible in the mach contour. Therefore when equilibrium is assumed, the gradient of pressure and temperature is able to trigger more chemical reactions, which is not the case for the non equilibrium combustion models. The mass fraction of O_2 for the JL model is the one that differs the most from the other models. However, since the plot are normalised for the initial composition it is not visible that globally, O_2 mass fractions are orders of magnitude lower than the other components, therefore the real variation of mass fractions is limited for all the models.

5.3.3 Transport properties

Custom definition of dynamic viscosity and thermal conductivity with temperature have been imported as described in section 4.4. The CFD software obtains the gas mixture average dynamic viscosity and thermal conductivity by averaging the properties with a mass-weighted average for both. Dynamic viscosity and thermal

conductivity are particularly relevant when it comes to determine the boundary layer behavior. Dynamic viscosity changes the way the high core kinetic energy is transformed in heat while thermal conductivity determines how this heat is exchanged. Therefore, since the viscous stress depends on the velocity gradient, the core gas properties are not affected on a large scale by a variation of transport properties with temperature, since there are no big changes in the velocity gradients. On the other side, the boundary layer behaviour changes considerably due to strong velocity gradients. Figure 5.12 compares the effect of introducing custom transport properties with temperature to constant transport properties in the case of the 2S-CM2 combustion model.

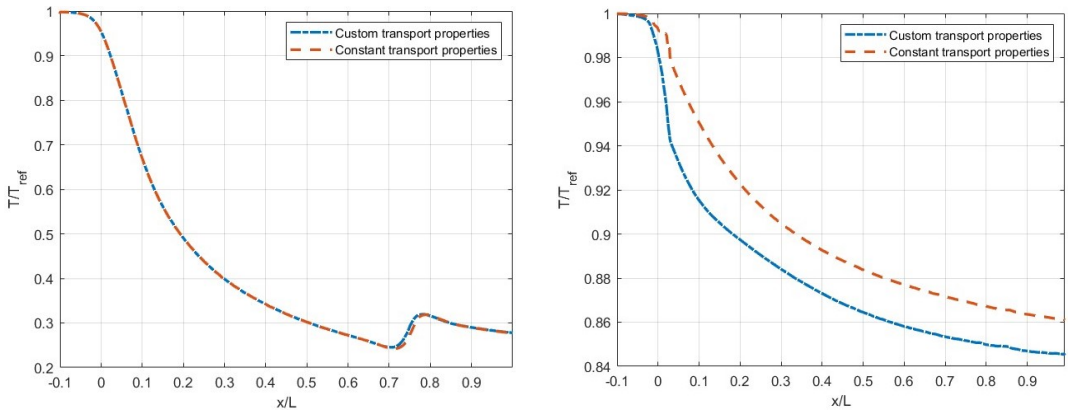

(a) Axis temperature (b) Adiabatic wall temperature

Figure 5.12: Effect of custom transport properties

As expected, the axis temperature shows no changes after introducing transport properties, except for a small region around the shock reflection, where the temperature gradient leads to a local change in transport properties. The difference is instead noticeable on adiabatic wall temperature. In a gas, dynamic viscosity and thermal conductivity decrease as temperature decreases. Therefore, when the temperature decreases because of the expansion, less energy is converted from kinetic to heat and the temperature decreases even more. At the same time the conductivity decreases, leading to less heat being transferred to the wall, contributing to the reduction of temperature compared to the constant properties case.

5.3.4 External radiation and MCC data

The external radiation model described in section 4.5 has been implemented on the outer surface of the nozzle. The outer surface radiates the heat reducing the NE wall temperature. Figure 5.13a compares the wall temperature for the equilibrium case with and without the external radiation. When radiation is added on the NE external wall, the temperature decreases at the beginning of the NE. This temperature

approaches the temperature computed with the 1D model. However, the first part of the nozzle extension with these hypothesis shows a high temperature. this is due to the fact that the temperature decreases from the higher value of temperature in the MCC that is equivalent to the MCC adiabatic wall temperature since the wall is considered as adiabatic. This results, also, in an axial temperature gradient due to the fact that the temperature on the MCC is higher than it should be. Since this thesis focuses on the NE, the regenerative cooling system present in the MCC has not been simulated. To provide a better understanding of the NE temperature envelope the inner wall temperature of the MCC has been provided by the company internal wall temperature estimation and used as a temperature boundary condition as described in section 4.7.

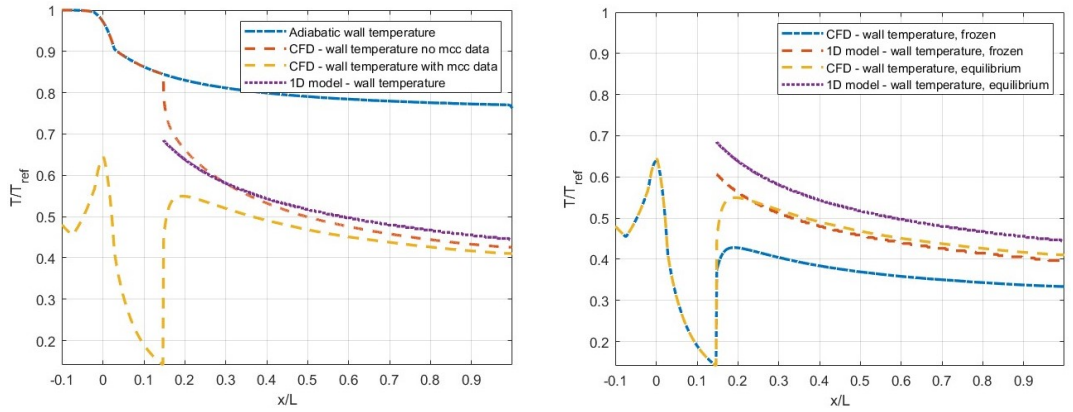

(a) Wall temperature with radiation (b) Equilibrium/frozen wall temperature

Figure 5.13: Wall temperature envelope

Figure 5.13a shows the corrected temperature profile on the wall. At $x/L = 0$ the throat peak temperature is visible. The NE axial coordinate is $x/L = 0.14$. At that point the temperature suddenly increases since no more regenerative cooling is present. The addition of the MCC data also decreased the NE wall temperatures far from the junction. This is due to the aforementioned axial gradient that was present because of the adiabatic wall boundary condition on the MCC wall. The 1D model overestimates the wall temperature both in the equilibrium and in the frozen cases of 10 to 20 % as shown in Figure 5.13b. However, the approximation is better for the equilibrium than the frozen model. As expected, the frozen wall temperature is lower than the equilibrium wall temperature.

At this point the uncooled NE performances have been assessed. The data show that even in the best case scenario, a metallic NE can not survive the mission, therefore a cooling strategy needs to be implemented. The following section describes the implementation of film cooling on this geometry.

5.4 Film cooled NE

The coolant is injected at the NE-MCC interface, thanks to a convergent-divergent channel that accelerates the coolant to supersonic speed as described in subsection 4.1.2. Because of the supersonic speed, both the hot gas and the coolant are subject to compressibility, therefore it is important to check how expansions and shock waves interact. In this section the film cooling behavior is investigated, focusing on the interaction between the hot gas and the coolant, the effect of chemical reactions and the influence of feeding pressure on the flowfield.

5.4.1 Flowfield geometry

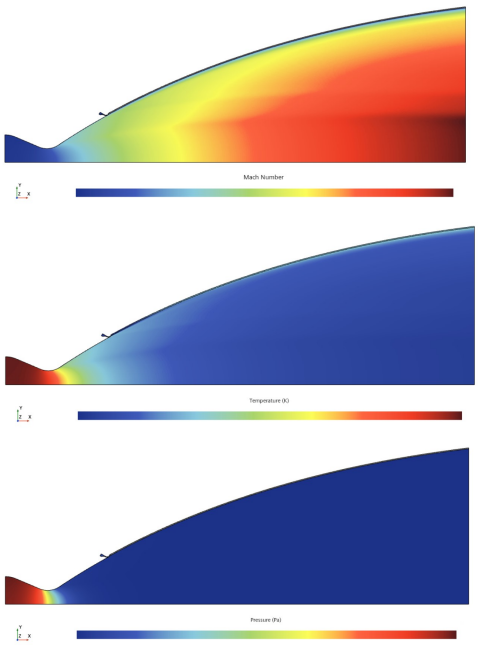

Figure 5.14: Mach number, temperature and pressure contours

Figure 5.14 shows the contour of mach number, temperature and pressure on the scale of the NE in a frozen composition simulation. The injection of a secondary flow of gaseous coolant partially affects the main stream flowfield. This is noticeable in the mach number contour, where a second shock originates from the film cooling injection point and flows out of the nozzle as the main shock described in the uncooled NE case. This is also visible in the temperature contour but not in the pressure contour since the scale ranges from the highest to the lowest pressures. Figure 5.15 provides a zoom on the injection point with a balanced pressure contour. It is clearly visible that multiple compressible phenomenon take place and interact with each other. Two shocks originate from the injection region, while expansion fans form from the upper and lower lip.

Song, C. and Shen, C.[28] investigated the flowfield behavior of a supersonic gas injected tangentially in a supersonic gaseous main stream under different feeding pressures with an experimental setup. Their research described the flowfield behavior around the injection point, focusing on the main visible phenomenon. The results showed a very complex compressible geometry, characterized by shock reflections, expansion-shock and shock-boundary layer interactions and separation bubbles. This is also influenced by the coolant feeding pressure since it changes the expansion ratio and the divergent characteristics. The inlet geometry is fixed and designed for a specific inlet stagnation pressure to provide a matched pressure condition at the

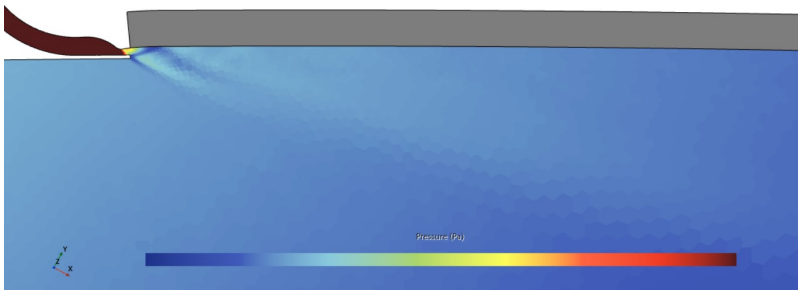

Figure 5.15: Calibrated pressure on film cooling injection

coolant channel exit. However, if the inlet stagnation pressure is changed, the channel becomes underexpanded if the pressure is increased or overexpanded if the pressure is descreased, since the local hot gas static pressure is the same. Figure 5.16 describes the main phenomenon that take place at the injection point as described by Song et Shen[28].

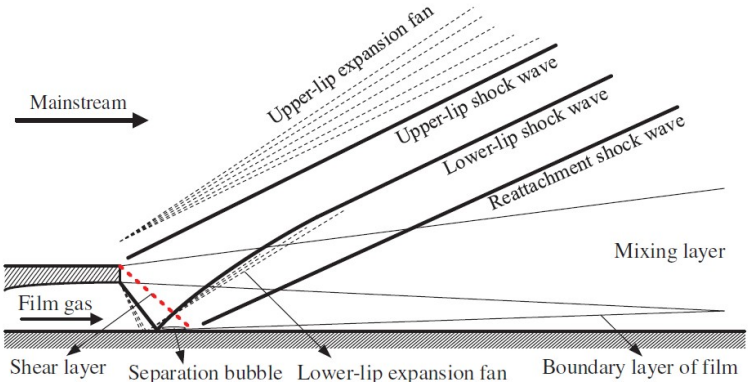

Figure 5.16: Schematic flowfield structures near the slot [28]

The lip edge forces the main flow to form an expansion fan from the upper edge, referred in Figure 5.16 as "upper-lip expansion fan". After the expansion the flow encounters the coolant secondary flow, therefore it has to compress forming a shock wave ("upper-lip shock wave"). When the deviated flow reaches the wall it forms a reattachment shock wave because of the deflection induced by the wall. At the same time, the secondary flow that leaves the coolant channels encounters the main flow, forming an expansion fan and a shock wave, depending if the channel is overexpanded or underexpanded. The lower lip shock forms from the lower edge of the lip. This shock reflects on the wall an forms the "lower-lip shock wave". This reflection may create a separation bubble on the wall, again depending on the channel conditions. This description aims to characterize the most noticeable phenomenon that take place at the coolant injection point however this doesn't mean that each of these are

present at the same time in the way they are pictured in Figure 5.16. In fact, the same work of Song et Shen [28] showed how the shock waves that develop towards the main flow, tend to merge in a single shock wave, especially in underexpanded cases as described in subsection 5.4.3. Figure 5.17 shows the balanced pressure contour where the visible expansions and compressions are highlighted.

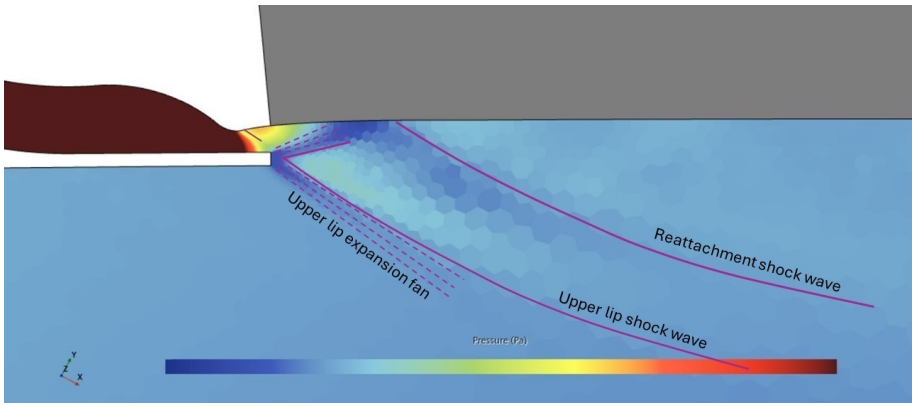

Figure 5.17: Balanced pressure contour

In this case (underexpanded) the upper-lip expansion and shock wave are clearly visible. The flow deflects after the lip and encounters the coolant flow, expanding and than recompressing. The coolant flow, also, expands after the lip and than recompresses when it encounters the deflected main flow. Further down, the reattachment shock wave. In this case the reattachment and upper-lip shock waves do not completely merge as in the cases described in 5.4.3. The pressure contour also shows a shock wave that originates from the channel divergent section right after its throat.

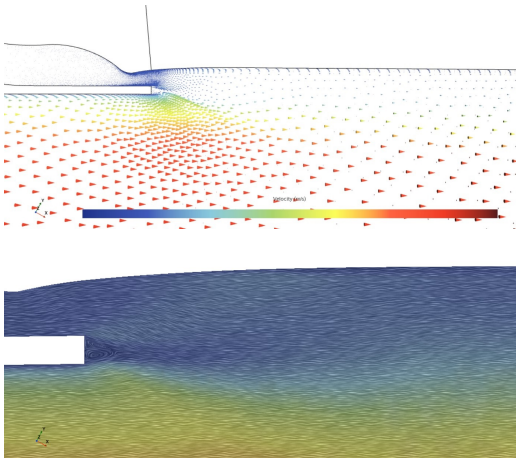

Figure 5.18: Pressure contour and vector field around the injection point

This is the same behavior of the main nozzle, as the shape of the coolant inlet channel was obtained with the same strategy, therefore a shock wave originates from the flex point of the parabolic arc conjunction with the divergent. The vector field of velocity clearly shows the slip line between the primary and secondary flows. As expected, the slip line deflects towards the main flow since this is and underexpanded case and the exit static pressure of the coolant is higher than the local gas static pressure. It is also noted that no separation bubble is formed on the wall in this case but it obviously forms around the lip thickness since it represents a supersonic deflection for both the primary and secondary flows. This is clearly visible in the

pathlines contour in figure 5.18. The mixing layer formation can be seen from the coolant mole fraction distribution as shown in Figure 5.19.

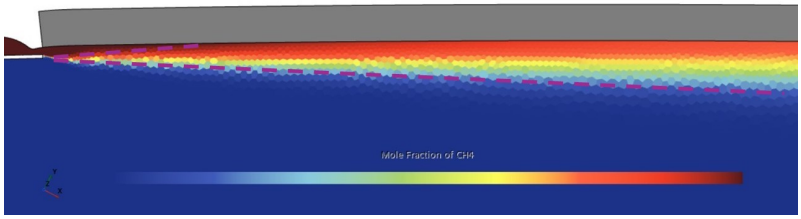

Figure 5.19: Mixing layer formation

5.4.2 Combustion models comparison

The purpose of injecting a cold gaseous stream of methane on the NE wall surface is to lower the local wall temperature. Unlike a MCC film cooling injection, a NE film cooling injection does not rely on local mixture ratio shifting to lower the resulting wall temperature. In fact, the main mechanism is diffusion, where the gaseous stream, since at lower temperature, cools the wall because of its temperature and not because of the lower chemical combustion temperature. However, the injection of methane may result in more combustion taking place along the wall, reducing the effect. Because of this, the influence of different combustion models has been investigated.

(a) Equilibrium CH_4 mole fraction

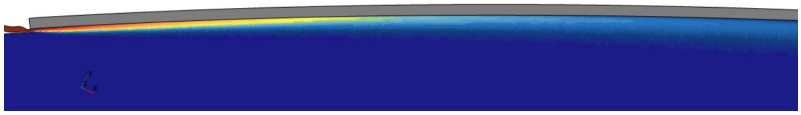

(b) Non equilibrium CH_4 mole fraction

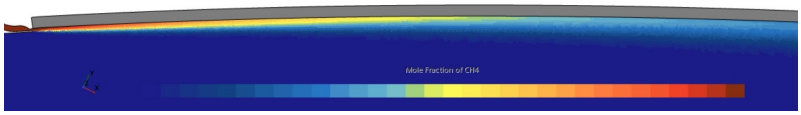

(c) Frozen CH_4 mole fraction

Figure 5.20: CH_4 mole fraction in equilibrium, non equilibrium and frozen cases

Figure 5.20 qualitatively shows the mole fraction distribution of methane around the injection region for different combustion models. As expected, Figure 5.20a shows a faster reduction of methane since equilibrium is considered. On the other hand, Figure 5.20c, with a frozen model, clearly shows that the methane mass fraction

decreases slower than the previous case. The frozen case represents the diffusion phenomenon: the methane undergoes mixing with the other species therefore its mole fraction reduces. This is also true in the equilibrium case, but due to chemical reactions methane reduces faster. The non equilibrium combustion model ($2S - CM2$[3]) in Figure 5.20b, as expected, sits in between the two cases. The distribution of the coolant on the wall thus determines the cooling properties. The effect of different combustion models on wall temperatures are shown in Figure 5.21.

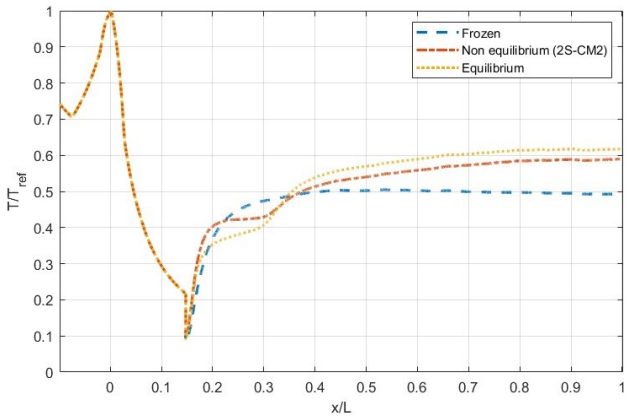

Figure 5.21: Film cooling wall temperatures

The reference pressure is the throat maximum wall temperature, while the reference length L is the NE exit section coordinate assuming the throat as the origin. As expected, the frozen model features the lowest maximum temperature, while the equilibrium model, the highest, with the non equilibrium in the middle but closer to the equilibrium. The behavior of temperature, however, is different between the three cases. In the frozen case the temperature keeps rising with a smooth trend, while in both equilibrium and non equilibrium cases, the temperature rising stops between $x/L = 0.2$ and $x/L = 0.3$ and then starts to rise again.

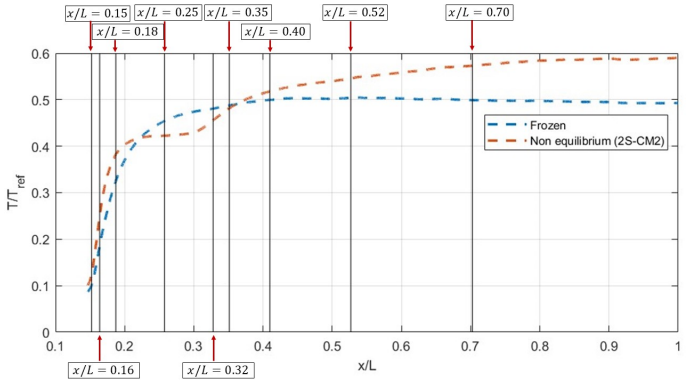

Figure 5.22: Axial position of next plots

To better understand the reasons behind this behavior, the mole fractions of the components have been plotted along the radius at different positions, depicted in Figure 5.22. The purpose of the next plots is to capture the mole fraction evolution in the points where the non equilibrium (and equilibrium) temperature profiles differ from the frozen one. Figure 5.23 collects these plots for the non equilibrium case.

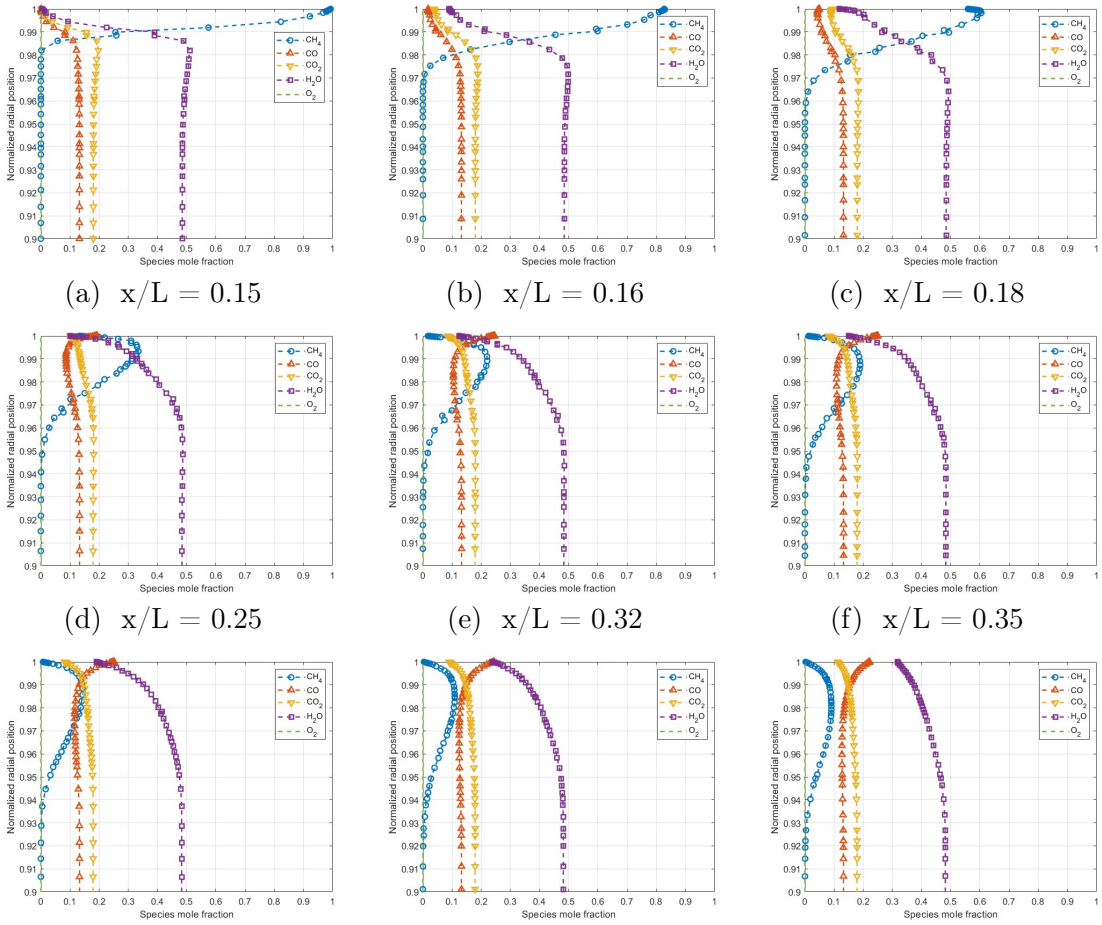

(a) x/L = 0.15 (b) x/L = 0.16 (c) x/L = 0.18

(d) x/L = 0.25 (e) x/L = 0.32 (f) x/L = 0.35

(g) x/L = 0.40 (h) x/L = 0.52 (i) x/L = 0.70

Figure 5.23: Mole fractions at different axial positions (2S-CM2[3])

The y axis corresponds to the local radius, normalised for its maximum value, therefore 0 identifies the axis of the engine while 1 identifies the wall. In close proximity of the injection point, the mole fraction of methane on the wall is 1, as expected, since it is the only species injected with film cooling (Figure 5.23a). The mole fraction of methane decreases on the wall surface until $x/l = 0.32$ (Figure 5.23e) where it reaches zero. The maximum value of methane mole fraction always decreases going from the injection point (Figure 5.23a) to forward positions on the x-axis. The oxygen mole fraction is orders of magnitude lower than the other species and appears on the plots as a vertical line on the zero value. However, this does not justify

the different temperature trend seen in Figure 5.21. In this case, both diffusion and chemical reactions take place and it is hard to tell which contributes affects more the mole fraction distributions in each position. In order to differentiate diffusion and chemistry, the same plots have been made in the frozen case and they are collected in Figure 5.24.

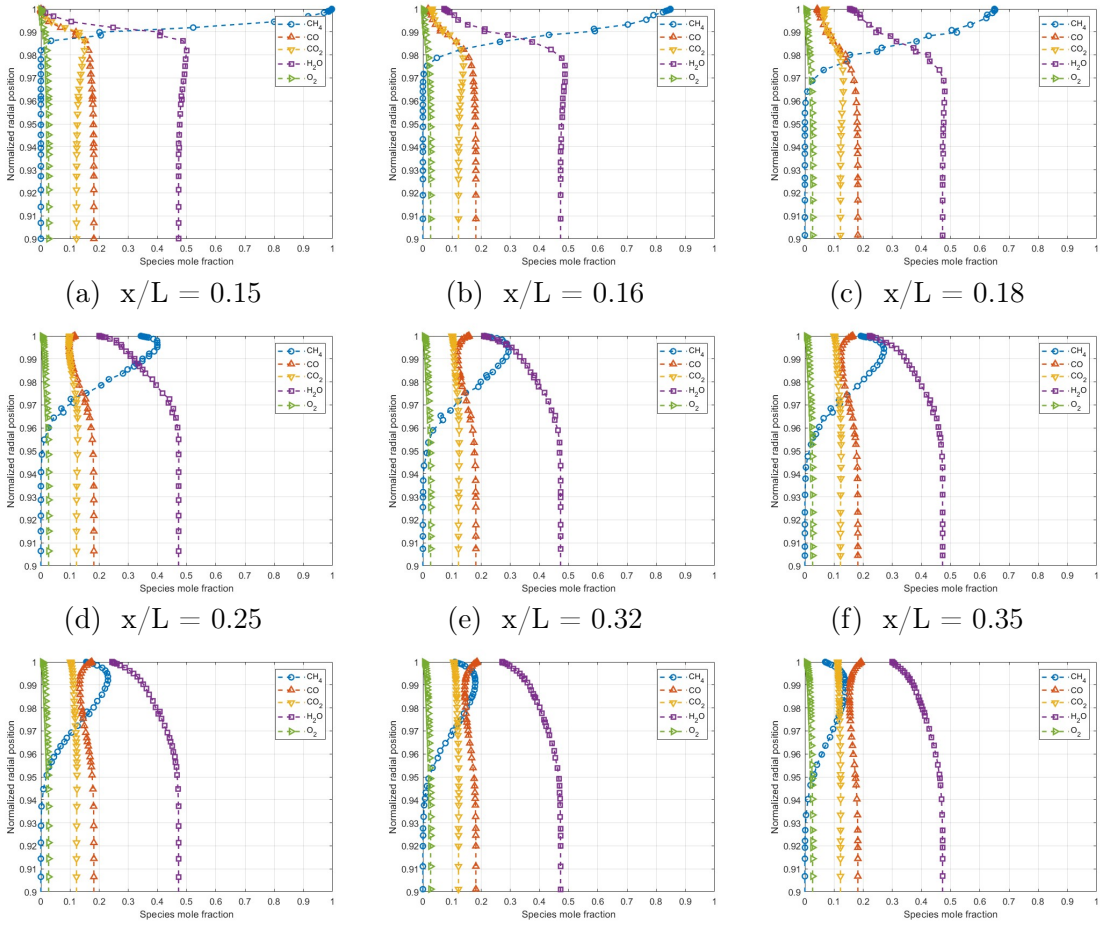

(a) x/L = 0.15 (b) x/L = 0.16 (c) x/L = 0.18

(d) x/L = 0.25 (e) x/L = 0.32 (f) x/L = 0.35

(g) x/L = 0.40 (h) x/L = 0.52 (i) x/L = 0.70

Figure 5.24: Mole fractions at different axial positions (frozen)

In a frozen case only species diffusion is responsible for mole fraction changes close to the wall. The difference between the plots in the non equilibrium and frozen cases represents the effect of chemical reactions which is limited. Most of the mole fractions change is due to diffusion. However, the frozen cases clearly shows that the mole fraction never goes to zero on the wall unlike the non equilibrium case. Therefore the faster consumption of methane in the non equilibrium case is due to its combustion with the oxygen that comes from carbon dioxide dissociation. Table 5.7 shows the chemical reactions involved in the 2S-CM2[3] non equilibrium combustion model, as described in subsection 4.3.2. These reactions are the methane

combustion with oxygen, the carbon dioxide dissociation and the carbon monoxide-oxygen recombination in carbon dioxide.

Reactions	A	β	E_a	Reaction orders
$CH_4 + 1.5O_2 \rightarrow CO + 2H_2O$	2×10^{15}	0.000	35000	$[CH_4]^{0.9}[O_2]^{1.1}$
$CO + 0.5O_2 \rightarrow CO_2$	2×10^{9}	0.000	12000	$[CO][O_2]^{0.5}$
$CO_2 \rightarrow CO + 0.5O_2$	8.1104×10^{10}	0.000	77194	$[CO_2]$

Table 5.7: 2S-CM2[3] mechanism (units in cm, s, cal, mol)

After the injection, on the wall, the cold temperature of the methane keeps the wall temperature low, but the mixing with the hot gases inevitably leads to a temperature increase on the wall. As the temperature rises, the methane reacts with the oxygen that comes from the dissociation of carbon dioxide. The result of this combustion is visible comparing Figure 5.23c and Figure 5.24c. The methane mole fraction decreases more in the non equilibrium model than the frozen case. At the same time, on the wall, the carbon dioxide mole fraction decreases while the carbon monoxide increases. This is a combined effect between the carbon dioxide dissociation and methane combustion which both produce carbon monoxide. The dissociation is endothermic, therefore it tends to lower the temperature, while the combustion is exothermic, so it increases the temperature. At $x/L = 0.32$ no more methane is left on the wall in the non equilibrium case, therefore the oxygen can now recombine with carbon monoxide to form carbon dioxide. This reaction is exothermic, therefore it tends to increase the temperature. This, however, is not enough to justify the sudden increase of wall temperature at $x/L = 0.32$ since a slight increase of carbon dioxide can be noted from Figure 5.23e to Figure 5.23i but it remains limited. The increase of temperature is due to the lack of the cold methane that was cooling down the wall before. In the non equilibrium case the methane is consumed by combustion and reaches a zero mole concentration on the wall that is never reached in the frozen case (i.e. diffusion), leading to a reduction in the cooling effect. When there's no more methane to cool the wall, the temperature rises, and it raises more in the non equilibrium case than in the frozen, because of the combination of a higher hot core gas temperature and a previous than expected methane mole fraction decrease on the wall. In the equilibrium case this effect is amplified. The methane is consumed even before than the non equilibrium case and the temperature starts to raise before and more.

Figure 5.25 shows the temperature profiles at the same axial positions as before over the radius. In Figures 5.25a and 5.25b, the interaction with the main shock wave that generates from the NE flex point is visible and after the shock wave the temperature increases. This is not clearly identifiable, since the velocity direction

should be considered, however it is clear that the trend of each temperature curve after the shock changes with an increase in temperature, as expected through a shock wave. Figure 5.25c and 5.25d focus on the temperature profile close to the wall.

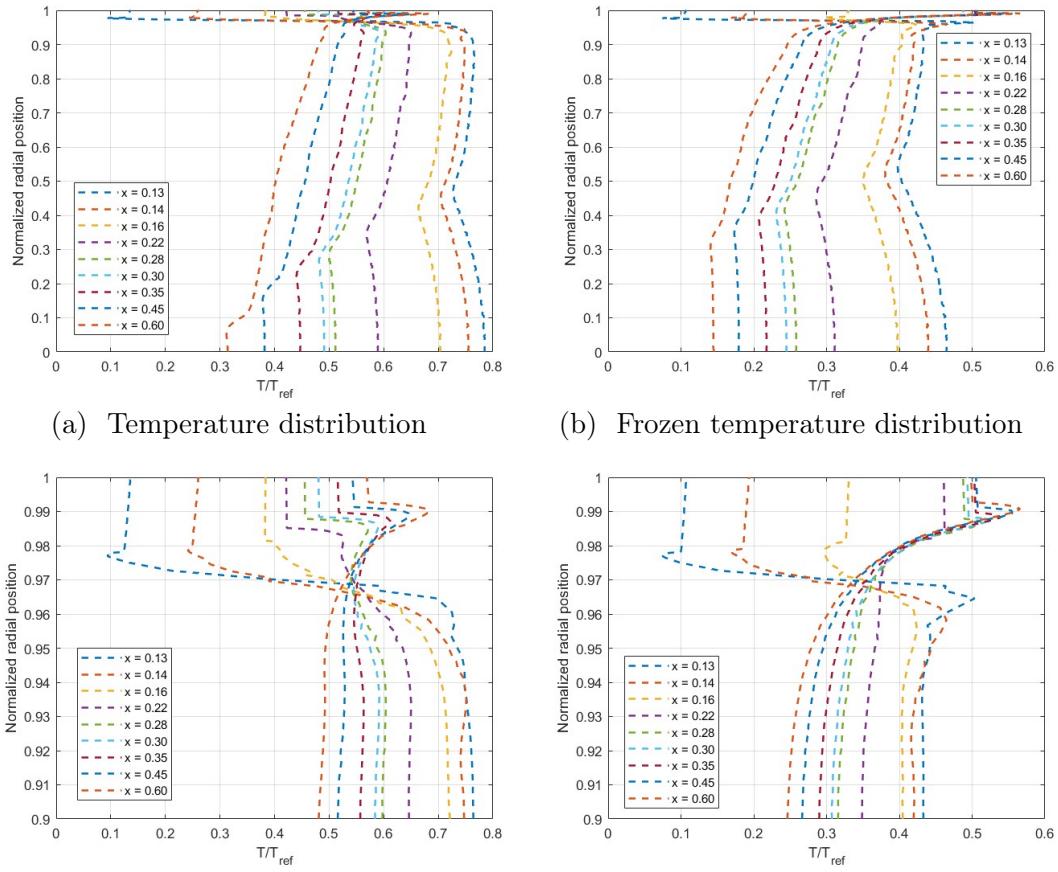

(a) Temperature distribution

(b) Frozen temperature distribution

(c) Distribution (zoom)

(d) Frozen distribution (zoom)

Figure 5.25: Temperature distribution

Becomes difficult to describe the temperature behavior close to the wall. When a hot gas stream flows over an adiabatic wall, the boundary layer strong velocity gradients slow down the supersonic flow exchanging kinetic energy for heat. This increases the wall temperature up to the adiabatic wall temperature. In this case the wall is not adiabatic and the hot gas is cooled by the injection of a cold gas. Moreover, the interaction with the lip generated shock waves changes the temperature profile even more. However, it is clear that moving further away from the injection point, the wall temperature increases due to the decreasing film cooling effect both in frozen and non equilibrium cases. The analysis on different combustion models provides a realistic range of wall temperature for the NE with film cooling for fixed coolant feeding conditions. However, the wall temperature changes with different boundary

conditions have to be evaluated in order to determine if the coolant conditions that can be obtained by the engine's cycle match the NE thermal requirements. In the next section, the effect of multiple coolant feeding pressures has been evaluated.

5.4.3 Feeding pressure variation

The inlet conditions of the gaseous coolant may change during the engine operations. In off-design conditions the engine has to be still able to complete the mission, however in off-design conditions the properties of the feeding coolant can change. In this section the effect of changing the inlet pressure of the gaseous coolant is investigated in a frozen case.

The coolant is injected on the NE wall from a distribution manifold where, for simplicity, a stagnation condition is assumed. In stagnation conditions, the total and static pressure are equal, at least for an isentropic transformation. Table 5.8 summarises the inlet conditions of the coolant with the value p/p_{ref} for each of the 6 test cases. p is the coolant stagnation pressure in the distribution manifold, while p_{ref} is the coolant stagnation pressure for which the exit pressure of the coolant channel matches the local static pressure of the hot gas. A value of p/p_{ref} equal to 1 thus identifies the case where the static pressure of the coolant at the exit is expected to be the same of the static hot gas pressure for the specific geometry used. The geometry is kept the same for all computations, therefore only one value of p leads to a matched pressure at the exit of the isentropic convergent-divergent channel. Values smaller or greater than one indicate, respectively, that the channel is overexpanded or underexpanded.

Cases	1	2	3	4	5	6
p/p_{ref}	0.364	0.545	0.727	1	1.818	2.727
p_i/p_{ref}	0.118	0.145	0.191	0.255	0.497	0.767
p_i/p_g	0.526	0.645	0.847	1.124	2.197	3.389
B	0.507	0.733	0.963	1.372	2.413	3.631
DR	2.863	2.997	5.253	7.493	13.202	19.865
R	0.177	0.183	0.183	0.183	0.183	0.183
M_c	2.011	2.002	2.002	2.003	2.002	2.002

Table 5.8: Simulation cases parameters

All the other parameters in Table 5.8 are computed from the CFD outputs. p_i (injection) is the exit static pressure of the channel, while p_g is the local hot gas static pressure. p_i/p_g thus identifies the under/overexpanded nature of the channel as well.

B is the blowing ratio ($B = \rho_c u_c / \rho_g u_g$, the subscript c identifies the coolant, while g identifies the hot gas). The blowing ratio expresses the ratio of momentum between the coolant and the hot gas. DR and R are, respectively, the density and velocity ratios ($DR = \rho_c / \rho_g$, $R = u_c / u_g$). The last parameter is the convective mach number M_c. It is a measure of the stability of the mixing layer and how turbulence affects the streams interface [5] ($M_c = (u_g - u_c)/(a_g + a_c)$, a_g and a_c are the hot gas and coolant speed of sound). These parameters, combined, help to describe how the primary and secondary streams interact and mix and thus how the film cooling behaves for different feeding pressures. The coolant inlet stagnation temperature is kept the same for each case. Table 5.8 shows that both R and M_c do not change significantly with different pressures. This is due to the fact that the inlet stagnation pressure does not change the injection channel expansion properties in terms of velocity. Therefore, the coolant exit velocity is the same for each case, as the hot gas velocity. Moreover, the static temperature at the exit point of the coolant is the same, since the stagnation temperature doesn't change. Also, the static temperature of the hot gas is not affected by a change in coolant stagnation pressure before the injection point. This means that the speed of sound (which depends on temperature) doesn't change either. Since the velocities and temperature do not change for coolant and hot gases, both R and M_c keep the same value for all the test cases. In test Case 1 there is a slightly more noticeable variation of R and M_c that is due to strong flow separation and will be described later. The variation of inlet stagnation pressure, however, changes to momentum balance between the hot gas stream and the coolant flow. This is described by the blowing ratio B. An increase of coolant stagnation pressure increases the density ratio DR which is the parameter that leads to a significant variation in blowing ratio. The hot gas density doesn't change, but the coolant density changes a lot at the injection point. Since the coolant is a gas, at the same temperature, an increase in pressure determines an increase in density, thus increasing DR. A higher stagnation pressure means that after the expansion (which is defined by the channel geometry) the coolant flow has more energy, i.e. more momentum. If the stagnation pressure is higher than the stagnation pressure for which the isentropic converging-diverging channel is designed, the flow is underexpanded. In fact, the ratio p_i/p_g for the Cases 5 and 6 are greater than 1. In Case 4, this ratio is expected to be close to one, since it is the case where the inlet coolant stagnation pressure is the one used to design the channel. However the ratio p_i/p_g in Case 4 is greater than one. This is due to the recompression in the diverging part caused by the shock wave that originates on the diverging parabolic flex point, as described before. The ratio p_i/p_{ref} shows how the exit static pressure of the coolant thus increases from Case 1 to Case 6.

The variation of feeding coolant stagnation pressure changes the flowfield after the injection point. Figure from 5.26 to 5.31 show the pressure contour of the region around the injection (all contours are balanced on the same pressure values). The

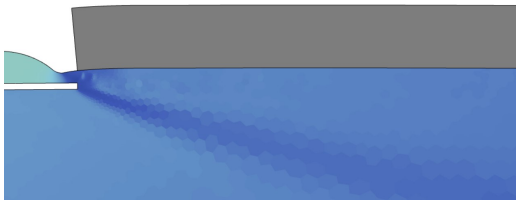

Figure 5.26: Case 1: $p/p_{ref} = 0.364$

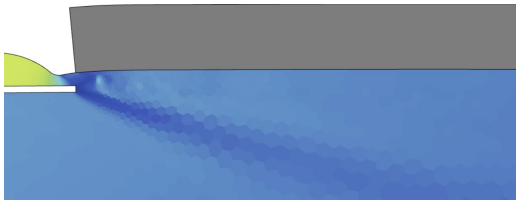

Figure 5.27: Case 2: $p/p_{ref} = 0.545$

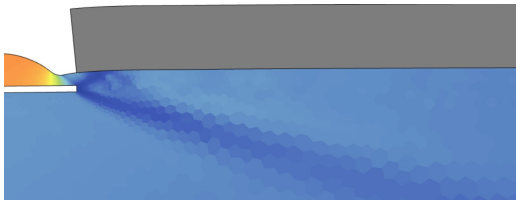

Figure 5.28: Case 3: $p/p_{ref} = 0.727$

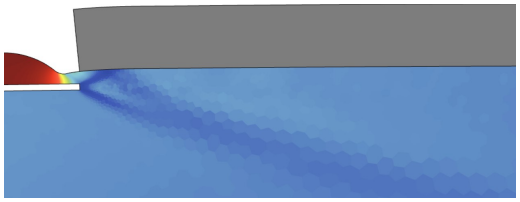

Figure 5.29: Case 4: $p/p_{ref} = 1$

Figure 5.30: Case 5: $p/p_{ref} = 1.818$

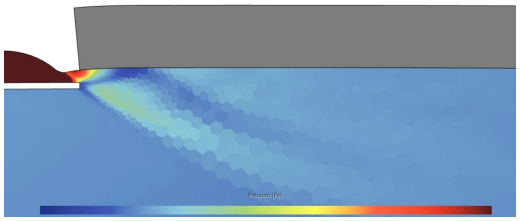

Figure 5.31: Case 6: $p/p_{ref} = 2.727$

general flowfield behaviour has been described in subsection 5.4.1. When a change in feeding pressure is considered, however, it becomes more difficult to explain the flowfield geometry, because the expansions and shock waves start to interact. Cases 1 to 4 show that the upper, lower lip and reattachment shock waves merge in a single shock wave, while in cases 5 and 6 the upper lip and reattachment shock waves never merge. At the same time, cases 4 and 6 are clearly underexpanded, therefore no lower lip shock wave is formed due to the overexpansion of the flow. However, the coolant flow continues its expansion out of the divergent and has to recompress when it meets the deflected main flow. This allows the formation of the lower lip shock wave for the underexpanded cases too. This shock wave however, merges with the reattachment shock wave when it reflects on the wall. Cases 1 to 4 are overexpanded, therefore the lower lip shock waves generates because of the pressure gradient between the hot gas deflected stream and the over-expanded flow. This shock waves, with the upper lip and reattachment shock waves, merge into a single shock wave and no differentiation is noticeable. In Case 1 it is even harder to determine how the compressible phenomenon interact since the channel is heavily overex-panded and the flow struggles to stick to the wall. As mentioned before it is the ratio of pressure and density that drives the coolant/hot gas interaction and not the velocity magnitude difference.

The kinetic flowfield behavior is deter-mined by the coolant channel isentropic

expansion. However, the direction of the velocity vectors gives an indication of how the coolant flow interacts with the hot gases. Figure 5.32 to 5.37 show the vector field of velocity around the injection region. In close proximity of the injection point, the velocity field is similar for all the cases. This is expected, as 5.8 shows that the velocity ratio R does not change much between cases. However, immediately after the injection section, the vector field of velocity changes a lot. Cases 5 and 6 (underexpanded) clearly show the deflection of the coolant stream towards the hot gas stream, due to the higher pressure ratio. Decreasing the inlet stagnation pressure (from Case 4 to 1), the momentum ratio shifts in favor of the hot gas stream and the coolant flow becomes overexpanded. Case 1 is an extreme case, since the flow separates from the NE wall and it is very close to separation also on the lower lip wall side. Figure 5.32 to 5.37 also show the evolution of the slip line between the hot gas stream and the coolant flow. This is again due to the increase of the blowing ratio with feeding pressure. The coolant flow carries more momentum and this cause the deformation of the coolant/hot gas slip line towards the hot gas stream. These flowfield also help to analyse how the shock waves interact with the boundary layer. The velocity vector fields show that close to the wall, the boundary layer is not uniform and it interacts both with the coolant and hot gas streams.

Figure 5.38 to 5.43 help to visualize

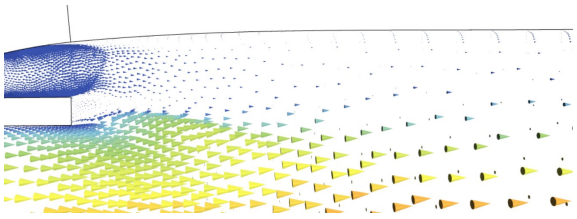

Figure 5.32: Case 1: $p/p_{ref} = 0.364$

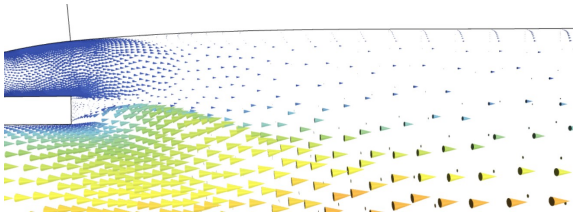

Figure 5.33: Case 2: $p/p_{ref} = 0.545$

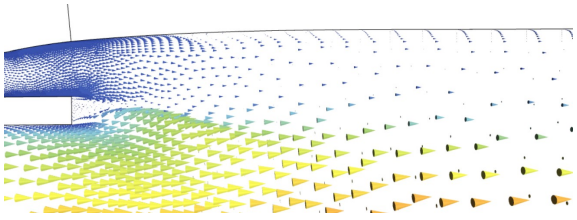

Figure 5.34: Case 3: $p/p_{ref} = 0.727$

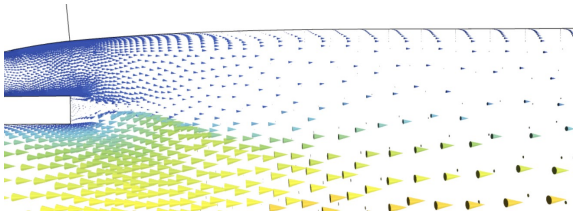

Figure 5.35: Case 4: $p/p_{ref} = 1$

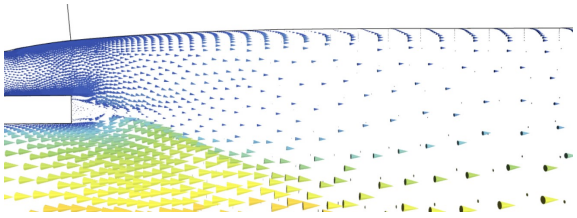

Figure 5.36: Case 5: $p/p_{ref} = 1.818$

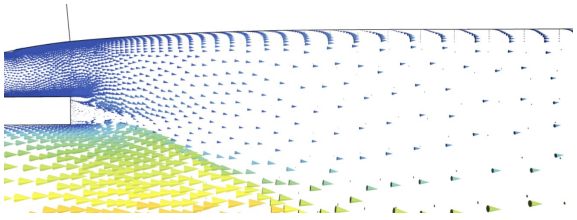

Figure 5.37: Case 6: $p/p_{ref} = 2.727$

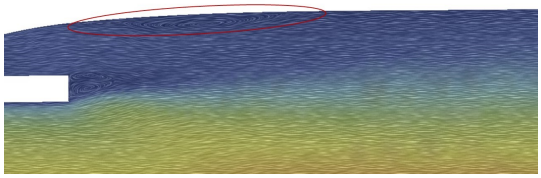

Figure 5.38: Case 1: $p/p_{ref} = 0.364$

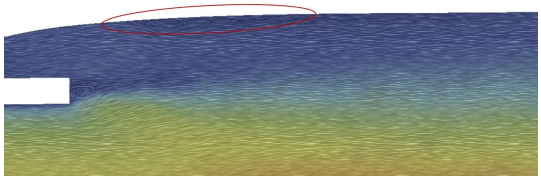

Figure 5.39: Case 2: $p/p_{ref} = 0.545$

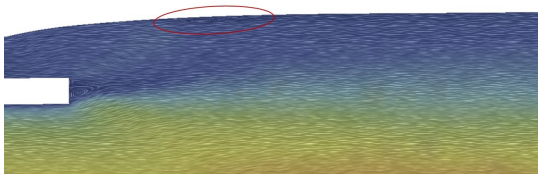

Figure 5.40: Case 3: $p/p_{ref} = 0.727$

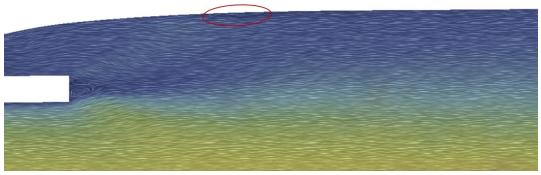

Figure 5.41: Case 4: $p/p_{ref} = 1$

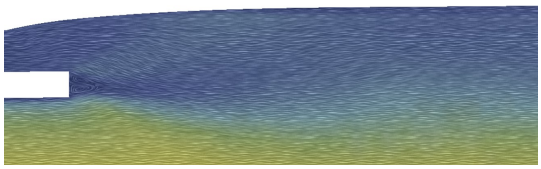

Figure 5.42: Case 5: $p/p_{ref} = 1.818$

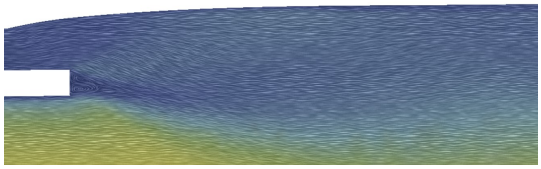

Figure 5.43: Case 6: $p/p_{ref} = 2.727$

the particles pathlines around the injection region. Two recirculation regions are clearly recognisable. The first, is the region adjacent to the lip. Both hot gas and coolant streams expand after the lip, since it is, effectively, a supersonic deflection. After the lip the recirculation zone keeps the same scale for each Case, however it is deformed by the momentum imbalance in over/underexpanded cases. When the blowing ratio is greater than one, the recirculation bubble after the lip deforms towards the hot gas flow and when the blowing ratio is less than one, the hot gas stream deforms the recirculation bubble towards the coolant flow. The second region is visible from Case 1 to 4 close to the NE wall. This region grows going from underexpanded to overexpanded cases, and it is primarily caused by the lower lip/reattachment shock wave and expansion fan interaction with the wall boundary layer. When the feeding pressure increases, the secondary flow momentum is able to stabilize the detachment eliminating the recirculation completely (this is visible in Case 5 and 6). In Case 1, the most overexpanded, the recirulation bubble extends up to the divergent channel as shown in both Figure 5.32 and 5.38. Separation bubbles may result in a higher than expected wall temperature and, therefore, in a reduction in film cooling effectiveness. The NE wall temperatures are shown in Figure 5.44 for each test case. A decrease in blowing ratio (i.e. feeding stagnation pressure in this case) leads to higher wall temperatures, while an increase in the coolant

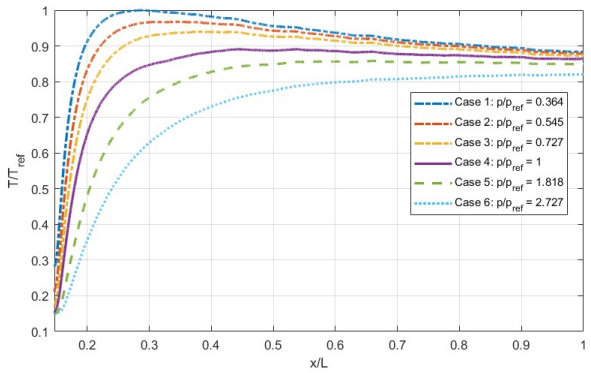

Figure 5.44: Wall temperatures for different feeding pressures

momentum leads to a lower maximum temperature on the wall. The adiabatic film cooling effectiveness is defined as:

$$\eta* = \frac{T_{aw} - T_g}{T_c - T_g}$$

η expresses the ratio between the temperature reduction obtained on the adiabatic wall with the film cooling over the maximum possible temperature reduction. In this case, the wall is not adiabatic, since external radiation is considered, therefore the film cooling effectiveness is:

$$\eta = \frac{T_{wall} - T_g}{T_c - T_g}$$

Film cooling effectiveness has been plotted for different coolant feeding pressure in Figure 5.45.

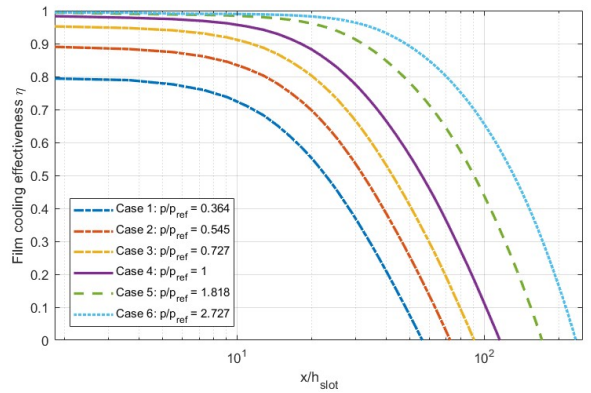

Figure 5.45: Film cooling effectiveness for different feeding pressures

The x-axis expresses the distance from the injection point, normalised for the slot

height h_{slot}. For overexpanded cases, as for the temperature, the film cooling effectiveness decreases faster than the underexpanded cases. Moreover, the value of η at the injection point for the overexpanded cases is lower than one. This is due to the recirculation bubble that keeps the flow detached and decreases its effectiveness in cooling down the wall. Underexpanded (high blowing ratios) keep the cooling effectiveness high further down the wall compared to overexpanded cases. The 1D model previously developed, assumes a matched exit pressure for the coolant, therefore only the 4th case can be compared with it.

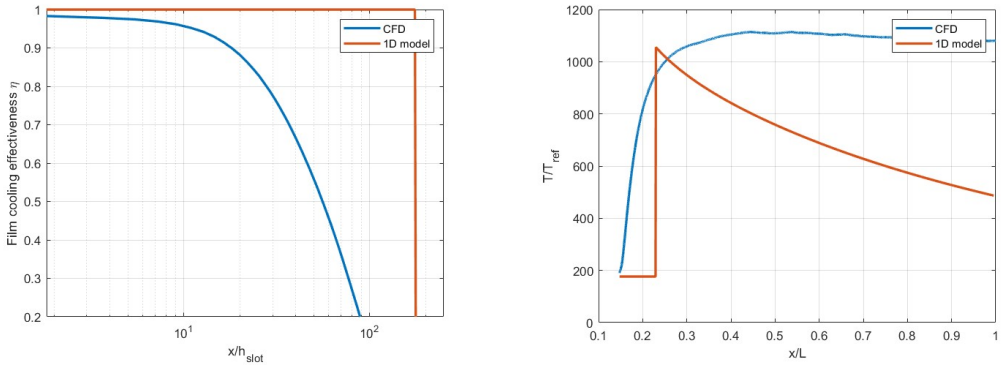

(a) Film cooling effectiveness (b) Wall temperature

Figure 5.46: Comparison with 1D model

Figure 5.46 compares the film cooling effectiveness and wall temperature computed with the developed 1D model and CFD. The 1D model is not able to reconstruct the temperature envelope computed by CFD and this can be due to many reasons. The model assumes that until the film cooling length x_1, the region is composed by only coolant at its injection temperature, therefore the first part of the nozzle wall is not heated by the hot gases. After the coolant region the mix temperature guides the heat transfer. The 1D model however predicts a decreasing in temperature rather than an increase, overestimating the cooling effect. This can be due to how the mixing temperature is computed. The film cooling model implemented hasn't been tested on supersonic injection problems and was tested for MCC subsonic coolant injection only. On the other side, the model seems to be able to capture both the maximum peak temperature after the coolant zone and the potential length of this.

5.4.4 Isp losses

Two different analytical model to determine the film cooling mass flow rate have been described in section 3.7. The first model assumes a wasted additional mass flow rate of film cooling (where wasted means it does not contribute to the thrust), while the second model computes the film cooling mass flow rate contribution to thrust assuming the coolant does not react with the core flow. The results in terms

of percentage losses per coolant mass flow rate percentage are presented in Figure 5.47

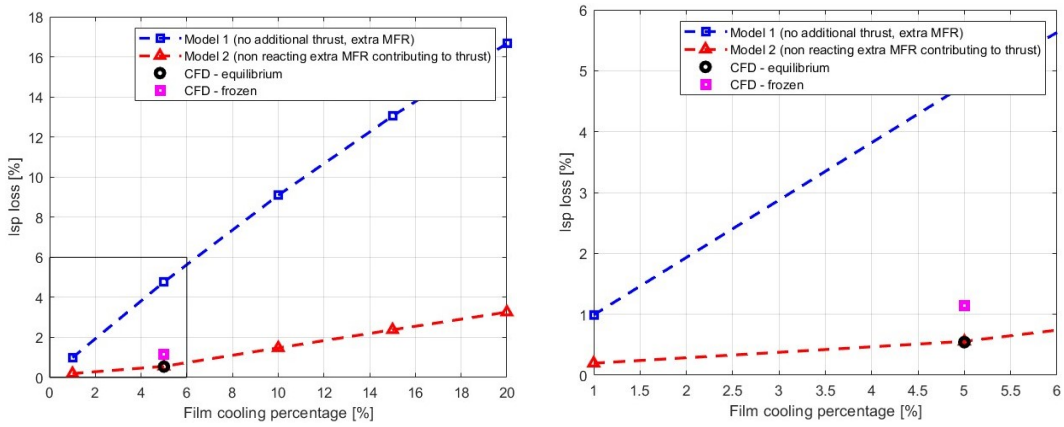

Figure 5.47: Isp losses due to film cooling

The film cooling percentage p is referred to just the fuel (methane in this case) mass flow rate and not the total propellant mass flow rate. If $\dot{m}_c$, $\dot{m}_f$, $\dot{m}_o$ and $\dot{m}$ are, respectively, the coolant (GCH4), fuel (LCH4), oxidizer (LOX) and total propellant mass flow rates, the following equations can be written for the NE:

$$p = \frac{\dot{m}_c}{\dot{m}_f} \qquad MR = \frac{\dot{m}_o}{\dot{m}_f} \qquad \dot{m} = \dot{m}_o + \dot{m}_f + \dot{m}_c$$

Where MR is the MCC mixture ratio. The Figure 5.47 shows, as expected, a higher reduction of Isp for the first model and a lower reduction for the second model. Multiple [4][23][24] experimental investigations about the relation between the percentage of film cooling and Isp percentage losses have shown a direct relation between them. It is also suggested that for a conservative rule of thumb to estimate the Isp losses, a one-one correlation between the two percentages defined as before can be adopted, therefore the percentage of Isp lost can be approximated with the percentage of coolant mass flow rate. This behavior is confirmed by the first conservative model in Figure 5.47.

The Isp losses have been also computed from the CFD simulations as described in section 4.8. Only one case of coolant mass flow rate has been investigated and the results are shown in Figure 5.47. The percentage of Isp lost differs in CFD computations between the frozen and equilibrium cases. This is not the case of the 1D model. The two curves representing the two Isp losses models do not differ between the equilibrium and frozen case, since the variation is expressed in percentage and both refer to the nominal reference frozen or equilibrium Isp computed by RocketCEA.

However the CFD simulations show a difference between the frozen and equilibrium cases. This is due to the fact that the CFD computation with equilibrium combustion model computes chemical reactions between the coolant and the core flow that lead to higher thrust and therefore a more limited reduction in Isp losses. On the other hand, the second model clearly approximates better the Isp losses compared to the first model.

Chapter 6

Conclusions

The engine NE thermal behavior has been investigated. The results show that a metallic NE can not survive in the engine's high temperature environment relying on external radiation only to dissipate heat. The engine NE needs an active cooling technique to reduce wall temperatures to values in range for the desired material and film cooling performances have been evaluated. The data shows that it is possible to effectively cool the NE with a relatively small amount of gaseous coolant injected at the interface between the NE and the MCC. Figure 6.1 and 6.2 show the temperature reduction on the wall when film cooling is implemented.

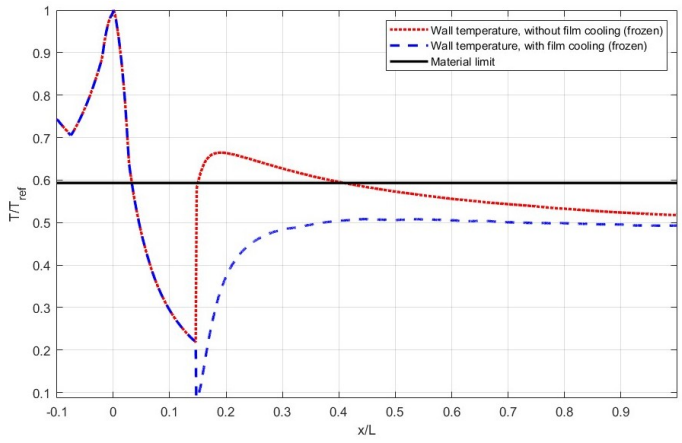

Figure 6.1: Wall temperatures (Frozen)

In a frozen case (Figure 6.1), the wall temperature without film cooling is already close to the maximum allowable material temperature. Therefore, film cooling effectively reduces the peak temperature enough for it to survive. In this case, a reduction in coolant mass flow rate may reduce the Isp loss even more, improving the engine performances. On the other side, in an equilibrium case (Figure 6.2), the film cooling mass flow rate is able to lower the peak temperature under the maximum material temperature, however the temperature rises further down the nozzle, exceeding the

limit. In a combustion model (2S-CM2) the temperature reduction is enough to barely stay within the allowable range.

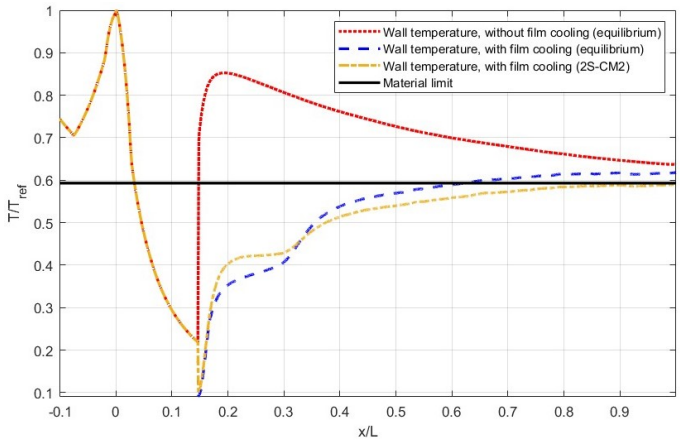

Figure 6.2: Wall temperatures (Equilibrium and 2S-CM2)

In a real case, the temperature envelope sits in between the frozen case and the equilibrium case. However, typically, the temperature profile is closer to equilibrium when the flow velocity is lower and closer to frozen when the speed is higher. The peak temperature in the equilibrium case is reached at the end of the nozzle extension, where the flow velocity is the highest. Therefore, the temperature profile should be better approximated by the frozen case, reducing the real wall exit temperature. This means that actually, the main concern for the nozzle survival is the peak temperature at the NE inlet. To improve the cooling effect, however, the coolant inlet parameters may be changed, increasing the coolant mass flow rate, its pressure or temperature. This comes with a cost in terms of engine performance loss or availability of different coolant conditions, in the terms described in this thesis. The results also showed how a simple 1D model can not easily describe the thermal behavior of mixing supersonic fluid in a rocket environment. This is due to the lack of detailed models for compressible mixing flows and the limited number of experimental data available in literature. This is also one of the reasons why, historically, supersonic gaseous film cooling research was carried out experimentally. Modern CFD techniques can help during the design phase but are limited by the implemented models that may change significantly the outputs, therefore experimental campaigns will deliver more significant results to anyone interested in developing a supersonic film cooled NE.

6.1 Design implementation

This thesis provides vital information for the design of a rocket NE. However, a number of simplifications have been made in order to provide multiple comparisons.

When it comes to the design of the component, some of these assumptions have to be evaluated. The performed CFD computations assumed an axisymmetric geometry and despite this being true for the convergent-divergent geometry of the engine, it is not true for the coolant injection geometry. In the CFD computations the injection is assumed on a continuous circumferential slot with a constant height. In a real case it is not feasible to realise a geometry like that, therefore the injection will be performed via a discrete number of holes as shown in Figure 6.3.

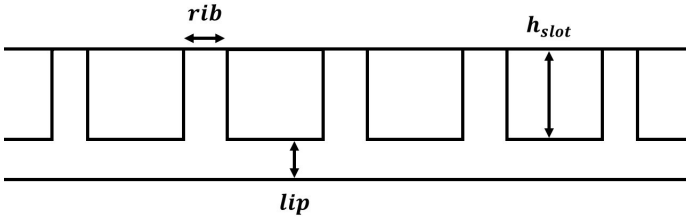

Figure 6.3: Discrete injection holes

These holes will be separated by a rib with a certain thickness, and they will be kept separated from the hot gas by a lip. In the CFD computations the actual slot height h_{slot} has been artificially reduced in order to keep the same mass flow rate of a discrete number of holes with the desired dimensions. In a real case, these geometries will interact with the main flow with shock waves and expansion fans and this behavior can only be described by 3D CFD computations.

Moreover, the manufacturing of the NE has to be considered. 3D printing of such a large component is already a complex procedure, therefore the precision printing of small orifices that are close to the 3D printing limits is even more complicated. The coolant is injected via a convergent-divergent channel, therefore the throat section features a even smaller hole area compared to the exit section. If this area is below the 3D printing minimum values, other parameters of the injection geometry have to be changed. If the throat area is at the limit and the mass flow rate has to be reduced, the only way is to reduce the channel thickness (i.e. increase the rib thickness). However, this can reduce the cooling performances on the wall, creating a pattern of linear spots where the coolant can not properly refrigerate the wall. Moreover, additive manufacturing requires specific conditions in order to print a component and presence of supports to allow the printing process have to be considered. If the NE will be printed from the exit section towards the inlet section, 45 degrees supports have to be designed to print the ribs of the channels, since they would effectively represent overhanging surface from the printer point of view. These supports wil be immersed in the hot gas stream and their survival has to be evaluated with CFD-thermal analysis.

The interface with the MCC is another critical point when designing a nozzle extension. Assuming the same material is used for the MCC (Inconel 718) and the NE, significant temperature differences result in different material expansion, therefore one component may be deformed by the heating of the other and vice versa. The results of this work show that at the injection point the wall temperature of the NE drops down due to cold methane flowing on it. The coolant injection point, however, is physically close to the regenerative cooling channel injection point, where the MCC wall temperature is cold as well. This is more complicated in the case of different materials. Different thermal expansion ratios may cause stresses on the interface bolting, potentially threatening the engine survival and this is even more dangerous if the NE material is not metallic. Carbon composites usually feature a lower thermal expansion coefficient and, moreover, they are brittle, and an excessive stress on the interface may induce fractures on the composite and, again, threaten the mission accomplishment.

When the geometry will be fixed, it will be tested. However, it is impossible to test this kind of NE on a test stand since the NE is a component designed to operate in the near vacuum environment of space. On the test stand where the engine is mounted on, the environment features a pressure equal to the ambient pressure (around 101325 Pa). The expansion performed by the NE lowers the exit static pressure of the hot gas orders of magnitude under the ambient pressure and this pressure gradient destabilises the supersonic flow leading to its detachment from the wall. This phenomenon is called separation and has to be always avoided in rocket engines. Separation is highly unstable and non-stationary, leading to unstable structural loads on the NE. Moreover, it could lead to dynamic instability if the frequencies of detachment and reattachment match the NE own frequencies. The only way to increase the NE outlet pressure is to reduce its expansion ratio and, therefore, its length, manufacturing a short version of the NE usually referred as "skirt". The purpose of this short skirt is to house all the sensor (thermocouples) needed to compare experimental data and simulation data at least for the first part of the NE, thus determining if the entire NE will survive the mission.

6.2 Future work

In order to provide a final design of the component, more research has to be carried out. When creating the CFD model, a custom definition of viscosity and thermal conductivity have been used, however, the results showed that also mass diffusion plays a big role in how the coolant interacts with the hot gases after the injection. Therefore it is necessary to implement a more refined description of mass diffusion, i.e. how each chemical species diffuses in each other. This will help separating the diffusion from the chemical reactions that take place close to the wall as described in subsection 5.4.2. 3D simulation are required in order to determine both the flowfield

and the temperature profile around the injection holes ribs and supports. These simulation will require a higher computational power than the simulation performed on this thesis but will provide essential data for the subsequent NE design. Lastly, separation has to been evaluated. Prediction of supersonic separation has proved to be a hard challenge from a computational point of view, since multiple studies tried to use CFD to accurately predict the point where the flow separates from the NE wall. This is greatly influenced by turbulence model which guide how viscosity and back pressure act to destabilise the boundary layer and induce separation. This phenomenon is much complex and its description is beyond the scope of this thesis. However, it can be said that due to its unstable, non-stationary and turbulent nature, common RANS approaches are not suitable to precisely capture supersonic flow separation. A great effort has been put by the scientific community to develope more refined and accurate models to predict flow separation involving both LES (Large Eddy Simulation) and DNS (Direct Numerical Simulation) approaches.

Bibliography

[1] National Aeronautics and Space Administration. "Liquid rocket engine nozzles". In: 1976.

[2] B. Aupoix et al. "Experimental and Numerical Study of Supersonic Film Cooling". In: *AIAA Journal* 36.6 (1998), pp. 915–923. DOI: 10.2514/2.495. eprint: https://doi.org/10.2514/2.495. URL: https://doi.org/10.2514/2.495.

[3] J. Bibrzycki and T. Poinsot. "Reduced chemical kinetic mechanisms for methane combustion in O 2 / N 2 and O 2 / CO 2 atmosphere". In: 2010.

[4] R. T. Cook. *Advanced cooling techniques for high-pressure hydrocarbon-fueled engines*. Tech. rep. National Aeronautics and Space Administration, Oct. 1979.

[5] Abanti Datta and K. Sinhamahapatra. "Investigation of the Influence of Convective Mach Number on Compressible Plane Jet Exhausting into Parallel Streams". In: *Journal of The Institution of Engineers (India): Series C* 99 (Aug. 2016). DOI: 10.1007/s40032-016-0336-8.

[6] Francesco Di Matteo, M. Rosa, and Marcello Onofri. "Semi-Empirical Heat Transfer Correlations in Combustion Chambers for Transient System Modelling". In: May 2010.

[7] Francesco Di Matteo, M. Rosa, and Marcello Onofri. "Semi-Empirical Heat Transfer Correlations in Combustion Chambers for Transient System Modelling". In: May 2010.

[8] Francesco Di Matteo et al. "Modelling and Simulation of Film Cooling in Liquid Rocket Engine Propulsion Systems". In: July 2012. ISBN: 978-1-60086-935-8. DOI: 10.2514/6.2012-3908.

[9] Manuel Frey, Konrad Makowka, and Thomas Aichner. "The TICTOP nozzle — a new nozzle contouring concept". In: May 2016.

[10] S. Gordon and B.J. McBride. *Computer Program for Calculation of Complex Chemical Equilibrium Compositions and Applications - I. Analysis*. Tech. rep. National Aeronautics and Space Administration, 1994.

[11] S. Gordon and B.J. McBride. *Computer Program for Calculation of Complex Chemical Equilibrium Compositions and Applications - II. Users Manual and Program Description*. Tech. rep. National Aeronautics and Space Administration, 1996.

[12] S. Gordon and B.J. McBride. *Computer Program for Calculation of Complex Chemical Equilibrium Compositions, Rocket Performance, Incident and Reflected Shocks, and Chapman-Jouguet Detonations*. Tech. rep. National Aeronautics and Space Administration, 1976.

[13] S. Gordon, B.J. McBride, and Martin A. Reno. *Coefficients for calculating thermodynamic and transport properties of individual species*. Tech. rep. National Aeronautics and Space Administration, Oct. 1993.

[14] William M. Grisson. "Liquid Film Cooling in Rocket Engines". In: 1991.

[15] Peterson Carl R. Hill Philip G. *Mechanics and Thermodynamics of Propulsion*. 2nd ed. Addison-Wesley publishing company, inc.

[16] W.P. Jones and R.P. Lindstedt. "Global reaction schemes for hydrocarbon combustion". In: *Combustion and Flame* 73.3 (1988), pp. 233–249. ISSN: 0010-2180. DOI: https://doi.org/10.1016/0010-2180(88)90021-1. URL: https://www.sciencedirect.com/science/article/pii/0010218088900211.

[17] K. A. Juhany, M. L. Hunt, and J. M. Sivo. "Influence of injectant Mach number and temperature on supersonic film cooling". In: *Journal of Thermophysics and Heat Transfer* 8.1 (1994), pp. 59–67. DOI: 10.2514/3.501. eprint: https://doi.org/10.2514/3.501. URL: https://doi.org/10.2514/3.501.

[18] Takeshi Kanda et al. "Experimental studies of supersonic film cooling with shock wave interaction". In: *AIAA Journal* 34.2 (1996), pp. 265–271. DOI: 10.2514/3.13060. eprint: https://doi.org/10.2514/3.13060. URL: https://doi.org/10.2514/3.13060.

[19] A.I. Leontiev, V.G. Lushchik, and M.S. et al. Makarova. "Temperature Recovery Factor in a Compressible Turbulent Boundary Layer". In: (2023), pp. 409–431. DOI: https://doi.org/10.1134/S0018151X22030117.

[20] Angela. Libal. *The Temperatures of Outer Space Around the Earth*. 2024. URL: https://sciencing.com/temperatures-outer-space-around-earth-20254.html.

[21] Wei Peng and Peixue Jiang. "Influence of Shock Waves on Supersonic Film Cooling". In: *Journal of Spacecraft and Rockets - J SPACECRAFT ROCKET* 46 (Jan. 2009), pp. 67–73. DOI: 10.2514/1.38458.

[22] Arnold Richard, Suslov Dmitry, and Haidn Oskar. "Convective and Film Cooled Nozzle Extension for a High Pressure Rocket Subscale Combustion Chamber". In: (2012). DOI: https://doi.org/10.2514/6.2010-1150.

[23] D. C. Rousar. *Plug cluster module demonstration.* Tech. rep. National Aeronautics and Space Administration, July 1978.

[24] D. C. Rousar and R. L. Ewen. *Combustion effects on film cooling.* Tech. rep. National Aeronautics and Space Administration, Feb. 1977.

[25] Pravin Sawant, Mamoru Ishii, and Michitsugu Mori. "Droplet entrainment correlation in vertical upward co-current annular two-phase flow". In: *Nuclear Engineering and Design* 238.6 (2008), pp. 1342–1352. ISSN: 0029-5493. DOI: https://doi.org/10.1016/j.nucengdes.2007.10.005. URL: https://www.sciencedirect.com/science/article/pii/S0029549307005304.

[26] Sun Shine, S. Sunil Kumar, and B. Suresh. "A new generalised model for liquid film cooling in rocket combustion chambers". In: *International Journal of Heat and Mass Transfer* 55 (Sept. 2012), pp. 5065–5075. DOI: 10.1016/j.ijheatmasstransfer.2012.05.006.

[27] Frederick F. Simon. *Jet model for slot film cooling with effect of free-stream and coolant turbulence.* Tech. rep. National Aeronautics and Space Administration, Oct. 1986.

[28] Changqing Song and Chibing Shen. "Effects of Feeding Pressures on the Flowfield Structures of Supersonic Film Cooling". In: *Journal of Thermophysics and Heat Transfer* 32.3 (2018), pp. 648–658. DOI: 10.2514/1.T5322. eprint: https://doi.org/10.2514/1.T5322. URL: https://doi.org/10.2514/1.T5322.

[29] Changqing Song and Chibing Shen. "Effects of Lip Thickness on the Flowfield Structures of Supersonic Film Cooling". In: *Journal of Thermophysics and Heat Transfer* 33 (Dec. 2018), pp. 1–7. DOI: 10.2514/1.T5479.

[30] Victor Zhukov and Alan Kong. "A Compact Reaction Mechanism of Methane Oxidation at High Pressures". In: *Progress in Reaction Kinetics and Mechanism* 43 (Mar. 2018), pp. 62–78. DOI: 10.3184/146867818X15066862094914.